kollar.laszlo.e_99_23

Savaria Institute of Technology
Faculty of Informatics
ELTE Eötvös Loránd University, Budapest

Vibration of Conductors under Extreme Weather Conditions

László E. Kollár

Dissertation for the degree of
Doctor of the Hungarian Academy of Sciences

Szombathely, 2023

Acknowledgments

Major part of the research presented in this thesis was carried out in the NSERC/Hydro-Québec/UQAC Industrial Chair on Atmospheric Icing of Power Network Equipment (CIGELE) and the Canada Research Chair on Atmospheric Icing Engineering of Power Networks (INGIVRE) at the University of Québec at Chicoutimi, Canada. I would like to thank Prof. Masoud Farzaneh, the chairholder, for assuring my progress in this research field during the years I pursued my research in his group, for my further colleagues and friends in the research chair, and for the CIGELE partners. My gratitude is also due to my former colleagues from the University of Huddersfield, in the United Kingdom. I am grateful to my colleagues in the Savaria Institute of Technology at the ELTE Eötvös Loránd University, Budapest, which is the location of further important achievements reported in the thesis. The research was supported by the János Bolyai Research Scholarship of the Hungarian Academy of Sciences, the project "EFOP-3.6.1-16-2016-00018 – Improving the role of research + development + innovation in the higher education through institutional developments assisting intelligent specialization in Sopron and Szombathely", and the project TKP2021-NVA-29 with the support provided by the Ministry of Culture and Innovation of Hungary from the National Research, Development and Innovation Fund, financed under the TKP2021-NVA funding scheme. My knowledge and expertise in this research field was established during the period I spent at the Department of Applied Mechanics, Budapest University of Technology and Economics. I would like to express my gratitude to Prof. Gábor Stépán who guided through the beginning of my research career and whose wise advises I can still count on.

Finally, I would like to thank the patience and the continuous support of my wife, Raquel, and daughter, Laura, who were always present during the long way to reach my goals.

Contents

1 Introduction **1**
1.1 Motivation and background 1
1.2 Main research objectives 2

2 Characteristics of droplet clouds causing ice accretion on structures **5**
2.1 Binary droplet collision 5
2.1.1 Coalescence after minor deformation 7
2.1.2 Further regimes of collision outcome 10
2.1.3 Composite collision outcome model 12
2.2 Further processes influencing droplet cloud characteristics 13
2.2.1 Evaporation and cooling 13
2.2.2 Gravitational settling 14
2.2.3 Turbulent dispersion 14
2.3 Modelling the variation of droplet cloud characteristics 15
2.3.1 Air velocity field 16
2.3.2 Droplet motion 17
2.3.3 Procedure of computation 18
2.4 Experimental modelling in an icing wind tunnel 19
2.4.1 Icing wind tunnel 19
2.4.2 Air velocity and droplet velocity measurements 20
2.4.3 Droplet size distribution and liquid water content measurements 21
2.5 Vertical and streamwise variations of droplet cloud characteristics 21
2.5.1 Droplet trajectory and droplet velocity 22
2.5.2 Vertical and streamwise variations of droplet size 23
2.5.3 Vertical and streamwise variations of liquid water content 26
2.6 New results 27

3 Conductor vibration following ice shedding **29**
3.1 Phenomena inducing conductor vibration 29
3.1.1 Wind-induced conductor motion 29

3.1.2 Phenomenon and consequences of conductor vibration following ice shedding . . . 31
3.1.3 Modelling conductor vibration following ice shedding . . . 32
3.2 Numerical modelling of vibration of bundled conductors following ice shedding . . . 33
3.2.1 Bundled conductors with spacers . . . 33
3.2.2 Finite element model of a single span of bundled conductors with spacers . . . 33
3.2.3 Results and discussion . . . 36
3.3 Numerical and experimental modelling of sudden ice shedding . . . 40
3.3.1 Experimental set-up . . . 40
3.3.2 Numerical model . . . 42
3.3.3 Validation of the numerical model . . . 43
3.3.4 Application for a full-scale span with a twin bundle . . . 49
3.4 Modelling ice shedding propagation on transmission lines with or without interphase spacers . . . 51
3.4.1 Numerical model . . . 51
3.4.2 Simulation of ice shedding propagation on a full-scale line . . . 52
3.4.3 Sudden and propagating shedding on conductors linked with interphase spacers . . . 57
3.5 New results . . . 59

4 Vibration suppression of transmission line conductors 61
4.1 Control of conductor vibration with time delay . . . 63
4.1.1 Mathematical model . . . 63
4.1.2 Validation of the static and dynamic behaviour of the model . . . 67
4.1.3 Stability of the controlled system . . . 69
4.1.4 Dynamics of the controlled system with time delay . . . 72
4.2 Ice-shedding-induced vibration of conductors with active vibration control . . . 75
4.2.1 Model of conductor vibration . . . 75
4.2.2 Parameter set-up . . . 78
4.2.3 Model validation . . . 79
4.2.4 Vibration of conductor with damper following ice shedding . . . 81
4.3 Dynamics of digitally controlled forced vibration of conductors with backlash 85
4.3.1 Mathematical model of controlled conductor vibration . . . 86
4.3.2 Parameter set-up and model validation . . . 88
4.3.3 Dynamics of controlled conductor motion with time delay and backlash 88
4.4 New results . . . 93

5 Summary 95

Chapter 1

Introduction

1.1 Motivation and background

Structures in energy engineering are often exposed to dynamic loads due to natural phenomena or to human intervention. These phenomena include strong wind, or load shedding, e.g. the shedding of ice accumulated on the structure under icing conditions, or shock load applied on the structure, which may be caused by an impact. These dynamic effects may essentially reduce the range of operation and lifetime of the structure. Such problems justify the effort to study the sources of dynamic loads and the process of the resulting vibration, and to develop solutions in order to reduce the undesired consequences. A common way of energy transmission and distribution across large distances is the utilisation of overhead transmission lines. These structures involve long suspended conductors, and the phenomena listed above may lead to high-frequency or high-amplitude vibration of the conductor. The consequence of high-frequency vibrations, e.g. the aeolian vibration caused by wind, is fatigue; whereas the high-amplitude vibrations, including galloping due to wind or the vibration following ice shedding, are associated with excessive dynamic forces, and they may damage some elements of the transmission line in a relatively short time. An important difference between galloping and ice-shedding-induced vibration is the following. High-amplitude vibration is maintained during galloping due to wind effect that acts as a periodic excitation on an asymmetrical conductor. On the other hand, vibration following ice shedding is characterized by high amplitude initially, and then the oscillation decays as a consequence of structural damping of the conductor and aerodynamic damping. Thus, ice shedding may induce high-amplitude vibration, but ice plays an important role in galloping as well, since the principal reason that makes the conductor asymmetric is ice accretion.

Ice accreted on structures installed or moving in the atmosphere may cause serious problems during the functioning and in the safety of the structure. Apart from overhead transmission lines, many other structures may be exposed to atmospheric icing; wind turbine blades, aircraft wings, or pantographs in electric trains or trams are the most common examples to mention. These issues justify the effort made to understand the conditions leading to icing and describe the accretion process.

Apart from transmission line conductors, suspended cables occur in further engineering applications including cable-stayed bridges or mooring of marine structures. Those cables are also exposed to natural phenomena that may cause heavy static load on the cable or that may lead to cable vibration. Such vibration may be associated with excessive dynamic forces resulting in severe damage to some elements of the structure that supports the cable. Understanding the reasons leading to such vibration and the process how such vibration develops require an in-depth study of the phenomenon including theoretical, numerical and experimental modelling. Simulation of cable vibration provides information about the amplitude and frequency of vibration, the developing stresses in the cable, and the forces acting on the cable and at the suspension during the vibration. Linear and nonlinear theories to describe the dynamics of suspended cables were developed decades ago [47, 48]. They describe the static equilibrium of a suspended cable, the response to a point load and to a uniformly distributed load, as well as the free vibration and the dynamic response of a suspended cable. The theory is well developed for a single cable, but transmission lines often consist of several spans of suspended conductors whose end-points are connected to suspension strings or insulators that can move during conductor vibration. Such structures and the motion of such structures were extensively studied by numerical and experimental modelling [43, 49, 67, 89, 106, 129, 132].

Several methods have been developed to attenuate cable or conductor vibration caused by natural phenomena and to reduce the harmful consequences. Vibration dampers that act as passive control are often installed on transmission lines to attenuate high-frequency, low-amplitude conductor vibration [124]. The interphase spacers applied in transmission lines contribute to the attenuation of high-amplitude conductor vibration and to keeping a safe distance between the phases during vibration [121]. Active control of cable vibration has been implemented on cable-stayed bridges [2]. Active control methods include the transverse or the axial motion of cable support. The displacement or the velocity of a chosen point of the cable is observed, and the control system determines a response that results in the displacement of the support, i.e. one of the end-points of the cable, so that the vibration amplitude of the observed point of the cable reduces. Time delay is always present in digital control due to taking samples of the observed parameter, and this delay influences the control efficiency and the parameters describing cable vibration. Increasing time delay tends to destabilize the controlled system, and above a critical value it leads to loss of stability [116]. When control is applied via mechanical driving, backlash occurs at the driving and causes small-amplitude oscillations around the equilibrium. The combination of time delay and backlash leads to irregular oscillations, which may be called "marginally chaotic" [60, 77, 78, 79].

1.2 Main research objectives

The research concerning the vibration of transmission lines under icing conditions and the related line protection methods focuses on three main areas. First, the process how ice develops on such structures as a conductor must be understood. The type, mass

and shape of ice depend on the ambient conditions; therefore, it is essential to study the characteristics of the cloud that eventually causes the ice accretion on the conductor. Then, effort should be made to describe conductor vibration due to natural phenomena including wind and ice shedding. The dynamic loads that act during the vibration and the resulting deformation and stresses in the line elements provide information about possible damages as consequences of these dynamic loads. Finally, methods are developed that contribute to attenuating the vibration, and thereby to reducing its harmful effects.

The research presented in this dissertation focuses on the areas described in the previous paragraph. In order to predict ice accretion on conductors, the characteristics of the clouds that are responsible for icing should be studied together with the processes influencing these characteristics. The approach proposed considers droplet collision, evaporation, gravity and turbulent dispersion. The theoretical background for the transition between two domains of collision outcome is developed and involved in the modelling approach. Apart from the theoretical model, experimental approach is also applied to simulate icing processes in a cold wind tunnel. These models describe the characteristics of droplet clouds and their variation in the flow, with particular attention to the droplet size distribution and liquid water content [66, 70]. This topic is the subject of Chapter 2.

Another main objective of this research is to study vibration of overhead transmission line conductors following ice shedding. Different ice shedding processes (sudden, propagating) are simulated numerically and experimentally. Finite element models have been developed in order to predict conductor rebound height, and the transient dynamic forces at the suspension during the resulting vibration. The numerical models are evaluated by comparing results to those of laboratory experiments obtained using a small-scale line model, and some results were also compared to observations on a full-scale test line [122]. The results obtained may be used to assess whether the vibrating conductors approach each other so that an electric arc may develop, as well as they provide information if the dynamic forces damage the suspension or other line elements [67, 71, 76]. Details are provided in Chapter 3.

The research also aims to examine the control of conductor vibration. A model simulating cable vibration with active control is developed in several steps. Since a number of parameters influence cable vibration and the efficiency of control, parametric study investigates the effects of sampling delay that occurs in digital control and excitation frequency. The active control methodology aims to attenuate small-amplitude, high-frequency vibration of suspended cables that are exposed to wind effect. The consideration of the nonlinear elastic material behaviour of the conductor makes the methodology applicable to the control of such high-amplitude vibration as that following ice shedding from the conductor. When backlash occurs at the driving, then the control force is not transmitted when the direction of rotation at the driving changes. The effects of the presence of time delay and backlash together in the control system may result in an irregular motion that justifies the detailed study of the dynamics of such systems [61, 62, 63]. These developments are discussed in Chapter 4.

The main achievements of this research are formulated in the theses at the end of

Chapters 2-4. The developments and results reveal that the goals are successfully achieved, and they are summarized in Chapter 5.

Chapter 2

Characteristics of droplet clouds causing ice accretion on structures

The droplet clouds that are responsible for ice accretion on structures in the atmosphere are characterized by several parameters including air temperature, air velocity, air humidity, liquid water content (LWC) and droplet size distribution (DSD). These are the most important factors affecting atmospheric icing processes; therefore, it is essential to determine them when modelling atmospheric icing. Natural aerosol clouds under icing conditions are modelled by injecting water spray into cold airstream, thereby creating a two-phase air/dispersed water flow. Such clouds undergo significant changes before reaching the icing object. Several factors influence these modifications including droplet collision and coalescence, evaporation and cooling, gravitational settling, and turbulent dispersion of the dispersed phase. This section focuses on binary droplet collisions, and the theory behind the transition between two domains of the collision outcome is developed. Then, theoretical and experimental models are presented for droplet motion and for the evolution of DSD in aerosol clouds considering the factors mentioned. The theoretical model is validated by wind-tunnel experiments, and the computed and measured results are discussed.

2.1 Binary droplet collision

The phenomenon of binary droplet collision is controlled by several physical parameters. The most important ones are the droplet velocities, droplet diameters, dimensional impact parameter, surface tension of the liquid, and the densities and viscosity coefficients of the liquid and surrounding gas. Further components may also be significant, such as the pressure, molecular weight, and molecular structure of the gas. From these physical parameters several dimensionless quantities can be formed, namely, the Weber number, Reynolds number, impact parameter, droplet size ratio, ratio of densities, and ratio of viscosity coefficients. For a specific liquid-gas system, the outcome of collision is usually described by the following three non-dimensional parameters: Weber number, impact parameter, and droplet size ratio. The Weber number is the ratio of the inertial force to

the surface force:

$$We = \frac{\rho_d U_r^2 d_S}{\sigma} \tag{2.1}$$

where ρ_d is the droplet density, U_r is the relative velocity of the interacting droplets, d_S is the diameter of the smaller droplet, and σ is the surface tension. The impact parameter is defined as the distance b from the center of one droplet to the relative velocity vector passing through the center of the other droplet, i.e. the dimensional impact parameter, divided by the sum of the radii of the colliding droplets:

$$B = \frac{2b}{d_L + d_S} \tag{2.2}$$

where d_L is the diameter of the larger droplet. The droplet size ratio is given by

$$\delta = \frac{d_S}{d_L} \tag{2.3}$$

although the reciprocal, $\gamma = 1/\delta$ is also used.

Comprehensive experimental studies on the possible outcomes of binary droplet collisions and the transition between their regimes were provided in [98, 104]. The evolution of the pressure and velocity fields during central binary collisions together with droplet deformation in the different regimes were studied numerically in [94]. The droplets may experience bounce or coalescence. Coalescence may be stable or temporary, followed by separation which may result in either disruption or fragmentation. In disruption, the number of post-collision droplets is the same as that prior to collision. In fragmentation, numerous satellite droplets are formed [98]. Qian and Law [104] distinguishes two regimes of separation according to the trajectories of colliding droplets and the subsequent separation process: separation for near head-on collisions or reflexive separation, and separation for off-center collisions or stretching separation. They also distinguish two regimes of stable coalescence that may be conjunct: coalescence after minor deformation and coalescence after substantial deformation. Thus, the binary droplet collision may result in five regimes of outcome described briefly as follows. If the drops approach each other slowly enough, or more precisely, the Weber number is low enough, then the gas trapped between the droplets has time to escape, so that coalescence occurs after minor deformation (regime I). If the Weber number is higher, then the surfaces of the droplets do not make contact due to the trapped gas layer, so the droplets become deformed and bounce apart (regime II). Further increasing the Weber number, when the kinetic energy of collision is sufficient to expel the intervening layer of gas, the droplets will coalesce after substantial deformation. The coalesced droplet deforms into a disk and oscillates until being stabilized in spherical form due to surface tension (regime III). For the highest Weber numbers, the kinetic energy of collision overcomes the surface energy, and the temporarily coalesced droplet is separated into two or more droplets during oscillation. The temporary coalescence is followed by reflexive separation for low impact parameters (regime IV), while the collision process ends up in stretching separation for high impact parameters (regime V).

The relative velocity of the colliding droplets, and consequently the Weber number, are

small in most cases of collision in the droplet clouds of the atmospheric icing processes that are under investigation and in their experimental models. Therefore, coalescence followed by separation (regimes IV and V) is practically non-existent; and even if it occurs, disruption may be assumed, when satellite droplets are not formed. On the other hand, bounce and stable coalescence either after minor deformation or after substantial deformation appear frequently. Hence, the transitions between regimes I and II as well as between regimes II and III have particular importance. Criteria for transition curves between the regimes of outcome have been proposed based on the physics of the collision phenomenon (see Section 2.1.2), except for the boundary between regimes I and II, which was developed in [70] and will be discussed in detail in Section 2.1.1.

2.1.1 Coalescence after minor deformation

The boundary proposed by [72] between the regimes of bounce and coalescence after minor deformation was a line joining two given points on the B-We plane. One of these points separates the regime of bounce from that of coalescence after substantial deformation for head-on collisions, while the other point is the one where the Weber number is zero and the impact parameter is unity. This condition provides a close approximation of the experimental observations of [104], but lacks physical explanation. The model developed in [70] applies an alternative boundary whose physical basis is explained in this section.

The boundary between coalescence after minor deformation and bounce is determined by two conditions. First, the thickness of the gas film trapped between the droplets has to be reduced to a critical thickness for breaking up the gas film and resulting in the coalescence of droplets. Second, during the sliding interaction of droplets (i.e. when $B \neq 0$), coalescence takes place only if the droplets do not pass near each other due to the sliding motion before the film thickness reduces to its critical value. When the collision model verifies these conditions, the governing equations of motion of the film-thinning process are not solved for each collision case, although approaches are available in the literature [52, 92], because the calculation would be computationally costly. Instead, the minimum film thickness that the gas layer may reach is estimated using characteristic values of the involved quantities, whereas the time required for the gas layer to be reduced to the critical thickness at rupture is estimated using time-scale analysis. Then, the two-phase flow model verifies only the two conditions in each collision case.

To express the first condition mathematically, the minimum thickness that the gas layer can reach as well as the critical thickness at rupture have to be determined. The minor deformation of each droplet takes place where the other droplet approaches and pushes the spherical surface by forming a disc of radii r_S and r_L on the smaller and larger droplets, respectively (see Figure 2.1). These radii are obtained from the balance of capillary and drag forces acting on the droplet. The drag force may be modelled as the viscous drag on a sphere [115] so that the force balance and then the radius of the smaller droplet take the form

$$r_S^2 \pi \frac{4\sigma}{d_S} = 3\pi d_S \mu_a U_r \tag{2.4}$$

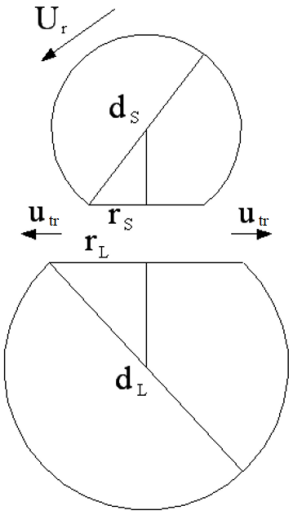

Figure 2.1: Two approaching droplets with relative velocity of U_r and the gas layer trapped between them

$$r_S = d_S \sqrt{\frac{3\mu_a U_r}{4\sigma}} \tag{2.5}$$

where μ_a is dynamic viscosity of the gas which is air in this model. Here, the velocity U_r is the approach velocity of the droplets, which is the component of relative velocity in the direction of the line connecting the centers of the two droplets. The pressure difference between the two sides of the droplet, which is balanced by surface tension, is smaller for the larger droplet, $4\sigma/d_L$, but the drag force is the same because it is determined by the area of the smaller droplet. Thus, the force balance for the larger droplet is written in the form

$$r_L = \sqrt{d_S d_L} \sqrt{\frac{3\mu_a U_r}{4\sigma}} \tag{2.6}$$

The transverse velocity of the gas, u_{tr}, is derived from a continuity condition, considering that a disc of surface $r_S^2\pi$ approaches the other disc with velocity U_r, and the gas escapes with velocity u_{tr} via a surface $2r_S\pi h$, where h is the gap thickness:

$$u_{tr} = \frac{r_S U_r}{2h} \tag{2.7}$$

The radius r_S is used here, because the volume intercepted between the two droplets depends on the size of smaller droplet. The dynamic pressure inside the gap, $\rho_a u_{tr}^2/2$, causes the deformation of droplet surface and is balanced by surface tension, $4\sigma/d_S$, where ρ_a is the air density [104]. This balance provides the maximum escaping velocity of the gas, u_{tr}, and the minimum thickness that the gas layer can reach is obtained after the substitution of Equation (2.7):

$$h = \sqrt{\frac{\rho_a d_S}{2\sigma}} \frac{r_S U_r}{4} \tag{2.8}$$

Equation (2.8) was derived using the interaction of the film with the smaller droplet.

The same thickness could be obtained, however, after considering the interaction with the larger droplet and also using Equations (2.5) and (2.6). The film thickness at rupture, h_r, is estimated by the following formula [13, 115]:

$$h_r = 0.802 \left(\frac{H_f r_S^2}{\sigma} \right)^{1/4} \tag{2.9}$$

where H_f is the Hamaker constant [92]. Again, r_S is used, because the intercepted volume depends on the size of the smaller droplet. MacKay and Mason [83] observed experimentally that the film thickness at rupture was less than 50 nm for droplet diameters up to 2500 μm. According to [13], Equation (2.9) is valid with a Hamaker constant, $H_f = 10^{-21}$ J, if the film thickness, h_r, is less than 12 nm. The above calculation for a liquid-gas system, which is the subject of this study, yields that this condition holds for droplets with diameter up to about 200 μm. Most of the droplets produced by the nozzles described in Section 2.4.1 are smaller than this limit, and although the diameter of largest droplets may exceed 200 μm in some cases, their number is so low that Equation (2.9) was accepted for all the cases considered. Then, the first condition of coalescence after minor deformation may be written in a simple form as:

$$h < h_r \tag{2.10}$$

which may be expressed after some algebraic manipulations using Equations (2.5), (2.8) and (2.9), the droplet Reynolds number $Re_d = \rho_a U_r d_S / \mu_a$, and that the approach velocity is $U_r\sqrt{1-B^2}$ for sliding interactions of droplets, as follows:

$$We Re_d^3 \left(1 - B^2\right)^{5/2} < 564.85 \frac{H_f \sigma \rho_a \rho_d}{\mu_a^4} \tag{2.11}$$

The right-hand side includes constants and fluid properties only; thus, it is constant for a fixed liquid-gas system.

Equation (2.11) is only a sufficient condition for coalescence after minor deformation if $B = 0$. If the impact parameter increases, this condition is satisfied for greater Weber numbers, which contradicts the experimental results of [104]. However, the sliding velocity, i.e. the component of relative velocity perpendicular to the approach velocity, increases with the impact parameter; hence, the droplets may slide near each other before the thickness of the gas film between them could be reduced to its critical value. In this case coalescence does not take place, and this is what the second condition should consider. Since the sliding velocity is $U_r B$, the time the two droplets need to slide near each other is expressed in the form

$$t_s = \frac{d_S + d_L}{U_r B} = \frac{d_S \left(\delta + 1\right)}{\delta U_r B} \tag{2.12}$$

The time for reducing the thickness h to h_r is obtained as follows. The relative velocity of the approaching droplets is reduced due to the force of fluid dynamic resistance, which

may be described by the following equation [92]:

$$m_d \frac{\mathrm{d}U_r}{\mathrm{d}t} = -\frac{6\pi\mu_a U_r}{h}\left(\frac{d_S d_L}{2\left(d_s + d_L\right)}\right)^2 \tag{2.13}$$

where $m_d = \rho_d d_S^3 \pi/6$ is the droplet mass. Equation (2.13) may also be written as

$$\frac{\mathrm{d}U_r}{\mathrm{d}t} = -\frac{1}{\tau_f} U_r \tag{2.14}$$

where τ_f denotes the characteristic time of the process and is defined by

$$\tau_f = \frac{\rho_d d_S \left(\delta + 1\right)^2 h}{9\mu_a} \tag{2.15}$$

An estimate of [115] will be applied for the initial film thickness when the droplets are close enough to each other for causing surface deformation. They chose the initial film thickness as 1/10th of the droplet radius. Thus, the characteristic time may be written as follows:

$$\tau_f = \frac{\rho_d d_S^2 \left(\delta + 1\right)^2}{180\mu_a} \tag{2.16}$$

Since the critical thickness, h_r, is at least two orders of magnitude less than the initial thickness, it may be assumed that the film thickness should be reduced by 1/10th of the droplet radius for coalescence, and the time scale of this process is given by Equation (2.16). The second condition for coalescence after minor deformation is that this time scale should be less than the time scale of sliding expressed by Equation (2.12):

$$\tau_f < t_s \tag{2.17}$$

or, after some algebraic manipulations

$$Re_d B\delta\left(\delta + 1\right) < 180\frac{\rho_a}{\rho_d} \tag{2.18}$$

Again, the right-hand side is constant for a fixed liquid-gas system. Thus, if conditions (2.11) and (2.18) are satisfied, then the collision outcome is coalescence after minor deformation. It should be noted that former collision models used three parameters (We, B and δ); while Equations (2.11) and (2.18) include the droplet Reynolds number as well, together with some fluid parameters that are constant for a fixed liquid-gas system.

2.1.2 Further regimes of collision outcome

The transition between bounce and coalescence after minor deformation is determined as explained in Section 2.1.1. The other boundaries are based on formerly proposed conditions.

The criterion for transition between bounce and coalescence after substantial deformation (regimes II and III) was proposed by [27]. They assume that if the initial kinetic

energy of deformation does not exceed the energy required to produce a limit deformation, then droplets will not coalesce, but bounce. Their condition for coalescence after substantial deformation was formulated as follows:

$$We > \frac{\delta\left(1+\delta^2\right)\left(4\varphi' - 12\right)}{\chi\left(1-B^2\right)} \tag{2.19}$$

where

$$\chi = \begin{cases} 1-\left(2-\kappa^2\right)\left(1+\kappa\right)/4 & \text{if} \quad \kappa > 1.0 \\ \kappa^2\left(3-\kappa\right)/4 & \text{if} \quad \kappa \leq 1.0 \end{cases}$$

with $\kappa = (1-B)(1+\delta)$ and φ' denoting shape factor which measures the deformation of the droplets from their initial spherical shape and whose proposed value is 3.351.

The reflexive separation criterion (transition between regimes III and IV) was provided by [6]. They consider that once the coalesced droplets have stretched far enough for a thin ligament to form, the surface energy will promote the separation rather than prevent it. Therefore, the reflexive kinetic energy need not be as high as the nominal surface energy for separation to occur. They postulate that if the reflexive kinetic energy exceeds 75% of the nominal surface energy, then separation occurs. They derived the following expression for this condition:

$$We > 3\left[7\left(1+\delta^3\right)^{2/3} - 4\left(1+\delta^2\right)\right]\frac{\delta\left(1+\delta^3\right)^2}{\delta^6\eta_1 + \eta_2} \tag{2.20}$$

where $\eta_1 = 2\left(1-\xi\right)^2\left(1-\xi^2\right)^{1/2} - 1$, $\eta_2 = 2\left(\delta-\xi\right)^2\left(\delta^2-\xi^2\right)^{1/2} - \delta^3$ and $\xi = B\left(1+\delta\right)/2$.

Reference [11] proposed the stretching separation criterion (transition between regimes III and V). The collision outcome is stretching separation if the rotational energy of the coalesced droplet exceeds the surface energy required to re-form the original two droplets from the coalesced pair, which is expressed as follows:

$$We > \frac{4.8}{B^2}\frac{\left[1+\gamma^2-\left(1+\gamma^3\right)^{2/3}\right]\left(1+\gamma^3\right)^{11/3}}{\gamma^6\left(1+\gamma\right)^2} \tag{2.21}$$

Reference [6] derived an alternative criterion; however, they evaluated that condition (2.21) also provides a satisfactory prediction. The velocity of the larger post-collision droplet was determined by [33], as follows:

$$V_L^{new} = \frac{V_L d_L^3 + V_S d_S^3 + d_S^3\left(V_L - V_S\right)Z}{d_L^3 + d_S^3} \tag{2.22}$$

where V_L and V_S are the velocities of the larger and smaller pre-collision droplets, respectively, and $Z = \left(B - B_{cr}\right)/\left(1 - B_{cr}\right)$ in which B_{cr} is the critical impact parameter above which the collision results in stretching separation. This parameter is calculated from the

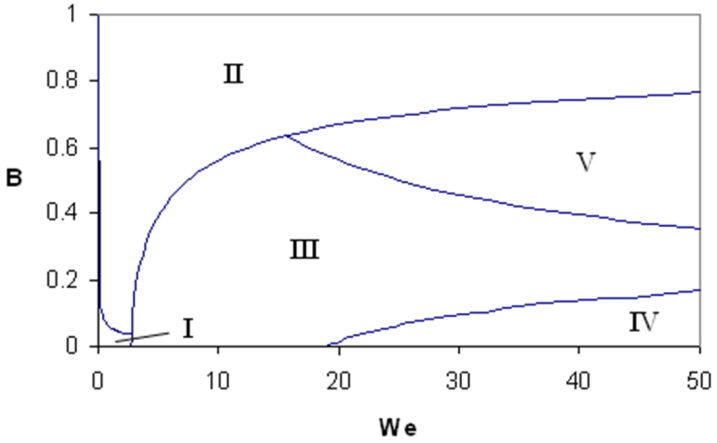

Figure 2.2: Collision outcome map on the $B - We$ plane for $\delta = 1$ and $d_S = 10\mu$m; I: coalescence after minor deformation; II: bounce; III: coalescence after substantial deformation; IV: reflexive separation; V: stretching separation

following formula:

$$B_{cr} = \min\left(1.0, \sqrt{\frac{4.8}{We}\frac{\left[1+\gamma^2-\left(1+\gamma^3\right)^{2/3}\right]\left(1+\gamma^3\right)^{11/3}}{\gamma^6\left(1+\gamma\right)^2}}\right) \tag{2.23}$$

The velocity of the smaller post-collision droplet is calculated similarly, with the quantities designating the larger and the smaller droplets interchanged in Equation (2.22).

2.1.3 Composite collision outcome model

Bounce affects droplet trajectory, but it does not modify the droplet size. Coalescence followed by disruption does not have any significant influence on droplet size. Other regions of collision outcomes, however, may influence droplet size. Fragmentation occurs when the relative velocity of colliding droplets is high, so the phenomenon almost never occurs in low-velocity flows that are under examination here. Coalescence after either minor or substantial deformation appear at low velocities; therefore, it is expected that their effects are significant as regards this study indicating that droplet collision causes an increase in droplet size.

The composite collision outcome model takes into account the five regimes defined earlier in this section. A typical outcome map in the $B - We$ plane is shown in Figure 2.2 for the water-air system. When two droplets collide, the outcome model is applied to determine the collision outcome and properties of the post-collision droplet(s), as follows. The Weber number, droplet Reynolds number, impact parameter, and droplet size ratio are calculated during simulation of the droplet motion. Firstly, it is ascertained whether coalescence after minor deformation occurs using conditions (2.11) and (2.18). If these conditions are not satisfied, then criterion (2.19) is used to determine whether or not bounce has occurred. If bounce has not occurred, then criteria (2.20) and (2.21) are applied to determine if the collision outcome is coalescence after substantial deformation,

reflexive separation, or stretching separation. After obtaining the collision outcome, the sizes, velocities, and temperatures of the post-collision droplets need to be determined. In case of coalescence, the size, velocity, and temperature are calculated in such a way as to conserve mass, momentum and to satisfy heat balance. When droplets bounce, their sizes and temperatures do not change and their velocities are modified according to the conservation of momentum. If separation occurs, it is assumed that satellite droplets are not formed, as discussed in the beginning of Section 2.1, and that the sizes and temperatures of post-collision droplets are equal to those of the pre-collision droplets. The velocities of post-collision droplets in the case of stretching separation are calculated according to the relation given by (2.22), while in the case of reflexive separation they are approximated by the velocities of the pre-collision droplets.

2.2 Further processes influencing droplet cloud characteristics

Several factors are responsible for the modification of the droplet cloud during its flow. The thermodynamic interactions between the dispersed and carrying phases result in evaporation and cooling. The mutual interactions within the dispersed phase are known as binary droplet collisions. The effects of external forces lead to gravitational settling of droplets and vertical variation of the DSD when the air speed is low. The extent to which these processes affect the characteristics of the aerosol cloud depends on the level of turbulence in the air flow. The turbulence also plays a key-role in the formation of aerosol clouds in wind-tunnel experiments. High levels of turbulence cause unrealistic thermodynamic processes in the tunnel and unnatural ice accretion. A certain level of turbulence, however, is essential to assure mixing and homogeneity in the cloud. Section 2.1 described binary droplet collisions in details. Further processes mentioned will be summarized in what follows.

2.2.1 Evaporation and cooling

The method that the model applies to calculate the decrease of droplet mass and temperature due to evaporation and cooling is based on the developments of [10] and [103]. This section recalls the formulae, but the reader is advised to see the above references for details. The rate of droplet mass, Δm_d, which is evaporated during the time interval, Δt, is obtained as follows:

$$\frac{\Delta m_d}{\Delta t} = -\frac{\pi d D_f \left(e_w\left(T_d\right) - RH_a e_w\left(T_a\right)\right)}{R_w T_f \left(1 - \frac{e_f}{p_{st}}\right)} Sh \tag{2.24}$$

where $e_w\left(T_d\right)$ and $e_w\left(T_a\right)$ are the pressures of saturated water vapor at droplet temperature, T_d, and at air temperature, T_a, respectively, RH_a the relative humidity of air, Sh the Sherwood number, R_w the gas constant for water vapor, p_{st} the static pressure of air,

and the subscript f refers to film formation on the evaporation surface involving droplet temperature and air temperature. The corresponding quantities $T_f = (T_d + T_a)/2$, $e_f = (e_w(T_d) + e_w(T_a))/2$ and $D_f = D_w(T_f)$ are, respectively, the mean values over the transfer path of the temperature, the pressure of saturated water vapor, and the diffusivity of water vapor, D_w. The Sherwood number is defined by the Reynolds number based on air velocity, i.e. $Re_a = d|\mathbf{u}|\rho_a/\mu_a$ where $\mathbf{u}$ stands for air velocity, and the Schmidt number, Sc, as follows:

$$Sh = 2\left(0.78 + 0.308 Re_a^{0.5} Sc^{0.33}\right) \tag{2.25}$$

The change in droplet temperature, ΔT_d, during the time interval, Δt, is obtained from the heat balance:

$$c_w m_d \frac{\Delta T_d}{\Delta t} = \alpha d^2 \pi (T_a - T_d) + L_{ev} \frac{\Delta m_d}{\Delta t} \tag{2.26}$$

where c_w is the specific heat of water, L_{ev} the latent heat of vaporization of water, and the heat transfer coefficient, α, is determined by the following expression:

$$\alpha = \frac{Nu \lambda_a}{d} \tag{2.27}$$

where λ_a is the thermal conductivity of air at the temperature of the droplet surface, and the Nusselt number, Nu, is defined by [127]:

$$Nu = 2 + \left(0.4 Re_a^{0.5} + 0.06 Re_a^{0.67}\right) Pr^{0.4} \left(\frac{\mu_a(T_a)}{\mu_a(T_d)}\right)^{0.25} \tag{2.28}$$

with Pr denoting Prandtl number. The T_d is the droplet temperature at the beginning of the time step, and $\Delta m_d/\Delta t$ is obtained from Equation (2.24).

2.2.2 Gravitational settling

Gravity is usually not considered in aircraft icing models due to the high air velocity and the corresponding dominance of drag forces; it significantly affects, however, droplet trajectory in atmospheric icing processes with gentle winds (below 20 m/s) and in their simulation in low-speed wind tunnels. The influence of gravity on droplet motion becomes particularly important for large droplets. A term considering gravity is included in the droplet equation which will be presented in Section 2.3.2.

2.2.3 Turbulent dispersion

The effect of turbulence on droplet motion is considered by a stochastic approach introduced by [22]. The instantaneous gas velocity, $\mathbf{u}$, is determined by adding a fluctuating component, $\mathbf{u}'$, to the gas mean velocity, $\bar{\mathbf{u}}$, in the droplet equation (see Section 2.3.2). The fluctuating component, $\mathbf{u}'$, is chosen from a Gaussian probability distribution with a standard deviation of $(2k/3)^{0.5}$, where k denotes turbulent kinetic energy. The value of the fluctuating component is changed at the beginning of each droplet–turbulent eddy

interaction. The time interval of this interaction is determined by the minimum of the eddy lifetime, t_e, and the transit time, t_r, over which the droplet traverses the eddy [37]. The eddy lifetime is provided by the form:

$$t_e = \frac{l_e}{|\mathbf{u}'|} \tag{2.29}$$

In this equation, l_e is the characteristic size of the turbulent eddy given by the following formula:

$$l_e = \frac{C_\mu^{0.75} k^{1.5}}{\epsilon} \tag{2.30}$$

where $C_\mu = 0.09$, and ϵ is the turbulent dissipation. The estimation for transit time takes the form:

$$t_r = -\tau_r \ln\left(1 - \frac{l_e}{\tau_r |\mathbf{u} - \mathbf{v}|}\right) \tag{2.31}$$

where $\tau_r = 4\rho_d d / (3\rho_a C_D |\mathbf{u} - \mathbf{v}|)$, C_D is the drag coefficient, and $\mathbf{v}$ is the droplet velocity. When $l_e / (\tau_r |\mathbf{u} - \mathbf{v}|) > 1$, Equation (2.31) does not have a solution, therefore it is assumed that the time of droplet–eddy interaction is equal to the eddy lifetime, t_e.

2.3 Modelling the variation of droplet cloud characteristics

Droplet clouds under icing conditions may be modelled by two-phase air/dispersed water flows. A widely used method to analyze fluid-particle flows is the Eulerian-Lagrangian approach, which treats the fluid phase as a continuum and considers the dispersed particles as a discrete phase [17, 18, 23]. These authors considered the heat and mass exchange between the phases, which results in droplet evaporation and cooling. The droplet equation of motion includes the gravity term, which is important for low velocities. Crowe et al. [18] developed a computational model which solved gas flow equations and droplet equations, and also considered the decrease of droplet mass and temperature due to evaporation and cooling; they ignored, however, the effects of turbulence on droplet dispersion and collisions between droplets. Dukowicz [22] proposed a stochastic approach to consider turbulence dispersion of droplets, which was elaborated for thick sprays by [99], and modified in [37, 84]. O'Rourke and Bracco [99] also considered droplet collisions and coalescence in their model by a stochastic approach, which was subsequently applied in [33]. Droplet trajectories for different velocities of the ambient air was examined in [32]. Post and Abraham [102] constructed a composite collision outcome model that included the different outcomes of binary droplet collisions except the lowest kinetic-energy collisions since they studied Diesel spray with high velocities. The developments of [59] took into account the formation of satellite droplets, which are the results of high kinetic-energy collisions between droplets [98]. Further improvements for high kinetic-energy collisions were proposed in [58, 90]. The relative velocity of colliding droplets is usually low in atmospheric icing processes and in their models in low-speed wind tunnels

where droplets are injected in the direction of the airflow; therefore, the collision model was improved in the range of the lowest kinetic-energy collisions and disregarded the formation of satellite droplets in [72]. This two-phase flow model considered droplet collision and gravitational settling, whereas evaporation and cooling were added later [73]. This study also discussed the range of thermodynamic parameters where the processes considered are dominant with regard to the evolution of the DSD. The turbulent dispersion of droplets was included in the model of [66], and time scales of the three processes involved together with that of turbulent dispersion were determined in [80]. A two-dimensional model of two-phase air/dispersed water flows was constructed in [72], and then further improved in [66, 70, 73, 80]. These models simulate the flow in the vertical section of a low-speed cold wind tunnel, which is applicable to reproduce a wide range of atmospheric icing processes.

The air velocity field together with turbulent parameters are determined first in the two-phase flow model. These data serve as input for the model that solves the droplet equation, tracks droplet trajectories, and calculates such droplet parameters as size, velocity and temperature, which are modified by the processes described in Sections 2.1 and 2.2. Thus, this model considers the influence of the carrier phase on particle motion, but it assumes that the dispersed phase does not change the continuous fluid phase. Some models, however, take into account two-way coupling between the phases (e.g. [18, 23, 119]). Numerous criteria have been proposed to establish whether the two-way exchange of mass, momentum and thermal energy between the phases is negligible or significant. Some of them were examined when developing the model in order to confirm that the one-way coupled model is an acceptable simplification in the cases investigated. Gore and Crowe [36] obtained that if the ratio of particle diameter to turbulent length scale, d/l_e, was less than 0.1, then particles did not increase turbulent intensity. Hetsroni [42] used the Reynolds number, Re, based on the gas-droplet relative velocity to define a condition. He reported that the dispersed phase did not enhance turbulence in the gas phase, if $Re \leq 110$. Both of these conditions for neglecting turbulence enhancement are satisfied in the cases modelled in this study. Gates et al. [32] examined if the air stream temperature and velocity changed due to heat exchange between the phases. The authors did not formulate any criterion; they assumed, however, that these changes were negligible when the liquid to air mass ratio was less than 1%. Although the liquid to air mass ratio may be significantly higher than 1% in thick sprays; the simulation domain begins 50 cm downstream the nozzle outlet where this ratio already decreases to the range of 1%. Wang et al. [125] reported that the droplets had little effects on air turbulence in typical clouds where the droplet mass loading was on the order of 10^{-3}, which is also the case in the major part of the wind tunnel in the experiments simulated. Due to the satisfaction of the above conditions, the one-way coupled model was accepted for the cases simulated in this study.

2.3.1 Air velocity field

The air velocity field is determined by the commercial software CFX, which solves the Navier-Stokes equations iteratively by using the finite volume technique. A default

tetrahedral element discretization is used for meshing. Boundary conditions assume no slip at the tunnel walls and zero velocity perpendicular to the wall. Velocities at the inlet and outlet and the geometry of the computational domain are defined as input data for this computation. The level of turbulence and the size of turbulent eddy at the inlet and outlet were defined as inputs in the droplet trajectory code, and their variations through the computational domain were approximated by a simple function which may be chosen according to the modelled process. Then, the turbulent kinetic energy, k, may be obtained from the level of turbulence, Tu, as follows:

$$k = \frac{1}{2}\bar{\mathbf{u}}^2 Tu^2 \tag{2.32}$$

and Equation (2.30) yields turbulent dissipation, ϵ.

2.3.2 Droplet motion

The droplet trajectory code is based on the particle-source-in-cell model constructed by [18], and the droplet equation derived by [86]:

$$\frac{\pi}{6}d^3\left(\rho_d + 0.5\rho_a\right)\frac{\mathrm{d}\mathbf{v}}{\mathrm{d}t} = \frac{\pi}{6}d^3\left(\rho_d - \rho_a\right)\mathbf{g} + 3\pi d\mu_a f\left(\mathbf{u}-\mathbf{v}\right) + \frac{\pi}{4}d^3\rho_a\frac{\mathrm{D}\mathbf{u}}{\mathrm{D}t} \tag{2.33}$$

where $\mathbf{g}$ is the gravity vector, f considers Stokes drag, the derivative $\mathrm{d}/\mathrm{d}t$ denotes time derivative following the moving droplet, and the $\mathrm{D}/\mathrm{D}t$ stands for time derivative following a fluid element. The last term in Equation (2.33) may be neglected, because this term is at least one to two orders of magnitude less than the other ones for all the cases examined. The parameter f, and the drag coefficient, C_D, are defined by the following expressions, respectively [18]:

$$f = 1 + 0.15Re^{0.687} \quad \text{and} \quad C_D = \frac{24}{Re}f \tag{2.34}$$

where the Reynolds number, Re, is based on the gas-droplet relative velocity:

$$Re = \frac{\rho_a\left|\mathbf{u}-\mathbf{v}\right|d}{\mu_a} \tag{2.35}$$

Then, assuming that $\rho_d \gg \rho_a$, and defining the non-dimensional parameters $\tilde{\mathbf{U}} = \mathbf{u}/\left|\mathbf{u}\right|$, $\tilde{\mathbf{V}} = \mathbf{v}/\left|\mathbf{v}\right|$ and $\tilde{T} = t\left|\mathbf{u}\right|/l$, where l is the horizontal length of the computational domain, the non-dimensional droplet equation is obtained after some algebraic operations:

$$\frac{\mathrm{d}\tilde{\mathbf{V}}}{\mathrm{d}\tilde{T}} = \frac{l}{\left|\mathbf{u}\right|^2}\mathbf{g} + \frac{18\mu_a l}{\rho_d d^2\left|\mathbf{u}\right|}f\left(\tilde{\mathbf{U}} - \tilde{\mathbf{V}}\right) \tag{2.36}$$

Since f varies with time, Equation (2.36) is integrated numerically by using the Euler scheme in a predictor-corrector mode:

$$\tilde{\mathbf{V}}_* = \tilde{\mathbf{V}}_j + \left.\frac{\mathrm{d}\tilde{\mathbf{V}}}{\mathrm{d}\tilde{T}}\right|_j \Delta\tilde{T}, \tag{2.37}$$

$$\tilde{\mathbf{V}}_{j+1} = \tilde{\mathbf{V}}_j + \left(\left. \frac{\mathrm{d}\tilde{\mathbf{V}}}{\mathrm{d}\tilde{T}} \right|_j + \left. \frac{\mathrm{d}\tilde{\mathbf{V}}}{\mathrm{d}\tilde{T}} \right|_* \right) \frac{\Delta\tilde{T}}{2}, \tag{2.38}$$

where $\Delta\tilde{T}$ is the non-dimensional time interval, the subscripts j and $j+1$ refer to quantities at the beginning and at the end of the time increment, respectively, while the subscript * refers to an intermediate value. After the droplet velocity, $\tilde{\mathbf{V}}_{j+1}$, at the end of the time increment, $\Delta\tilde{T}$, is determined, the corresponding droplet position, $\tilde{\mathbf{X}}_{j+1}$, is obtained by applying the trapezoidal scheme:

$$\tilde{\mathbf{X}}_{j+1} = \tilde{\mathbf{X}}_j + \left(\tilde{\mathbf{V}}_j + \tilde{\mathbf{V}}_{j+1} \right) \frac{\Delta\tilde{T}}{2} \tag{2.39}$$

2.3.3 Procedure of computation

Input data for the calculation of air velocity field, i.e. air velocities at the inlet and outlet of the simulated domain, are obtained from measurements, and then velocities are computed at many points in between by the commercial software CFX. The airflow field is subdivided into a series of cells, which are regarded as control volumes. An air velocity is associated with each control volume, which velocity was calculated closest to the midpoint of that control volume. The size of control volumes was chosen satisfying the conditions that the difference between the velocities of two neighbouring control volumes be small (in the range of few percents of the absolute value of velocity or less), and that their size be at least an order of magnitude greater than the size of the largest parcel of droplets.

The air velocity field obtained is used as input in the model of two-phase flows, which follows the motion of droplets in the control volumes. Since there are too many droplets to examine individually, they are collected into parcels. The method is based on the concept of the discrete parcel approach [99]. Each parcel contains the same number of drops of identical size, velocity and temperature that are required at the beginning of the computational domain as input data. The number of parcels has to be at least in the range of thousands in order to obtain a reliable statistics; however, increasing number of parcels increases computational costs significantly. As a compromise, 3000 parcels were considered in the simulations, each of which included 3000 droplets. The simulation is terminated after sufficient number of parcels reached the neighbourhood of the icing object to form a distribution, i.e. at least 1000.

The water flow may also be manipulated in the model by changing time step or the number of time steps between the injections of two parcels. The time step, however, is limited by the time scales of the processes modelled, of which collision was found to be decisive [80]. The time step should be small enough to avoid that two parcels "jump" each other during simulation; nevertheless it should be large enough to avoid collision immediately at the inlet.

In order to introduce a DSD into the model, the droplet spectrum is first discretized, 5-μm-wide bins are thereby created, and the diameter of each droplet is replaced by the arithmetic mean of the corresponding bin. The relative frequencies of the appearance of droplets in each bin are then used to obtain the discrete droplet spectrum. An interval

of random numbers corresponds to every discrete value of the droplet diameter in the spectrum. Then, the diameter of each droplet in a parcel is determined by the random number that was generated for that parcel as explained in [72]. Further inputs are the ambient conditions, which are assumed to be constant over the computational domain, and turbulence data, i.e. the level of turbulence and size of turbulent eddy.

The simulation of the two-phase flow proceeds as follows. The parcels are tracked in space and time as if they were single droplets with the size, mass, velocity and temperature of one droplet from that parcel. The fluctuating component of air velocity is modified after each time interval describing the droplet–turbulent eddy interaction. The actual fluctuating velocity is added to the air velocity at the beginning of each time step and is considered in the droplet equation. Then the position and velocity of droplets are determined by applying Equations (2.37)–(2.39), and the droplet size is reduced according to the loss of mass and the droplet temperature is modified due to evaporation and cooling (Equations (2.24) and (2.26)). If the lost mass is greater than or equal to the mass of the droplet itself, then the droplet is evaporated and the parcel is withdrawn from further computation. Afterwards, colliding droplets are sought for. From the collisional point of view, the parcel size is considered larger according to the mass of droplets carried in one parcel. If the distance between two parcels is less than the sum of their radii, they will collide. The outcome of collisions and the sizes and velocities of post-collision droplets are determined by utilizing the composite collision outcome model (see Section 2.1). If coalescence occurs, then the two parcels are replaced by one parcel in which the mass of droplets is equal to the sum of mass of the two colliding droplets. This process is continued in the next time steps until the termination condition of the simulation is satisfied.

2.4 Experimental modelling in an icing wind tunnel

A technique to model atmospheric icing and the modification of the droplet cloud preceding ice formation is to produce a two-phase air/dispersed water flow by injecting water droplets into cold air stream in an icing wind tunnel, and exposing an icing object to this flow. The aerosol cloud undergoes significant changes before reaching the icing object; therefore, its principal parameters including droplet velocity, DSD and LWC, should be measured at different positions in order to gain information about the evolution of cloud characteristics.

2.4.1 Icing wind tunnel

Experiments were carried out at the CIGELE atmospheric icing research wind tunnel in the University of Quebec at Chicoutimi [66, 69, 70, 72, 73, 74, 80]. This facility is a closed-loop, low-speed icing wind tunnel with a total length of about 30 m, including a 3-metre-long test section with a rectangular cross-section 45.7 cm high and 91.4 cm wide. The cross-section of the tunnel at the spray bar is also rectangular with a height of 1.7 m and width of 1.14 m. The tunnel becomes circular 1.5 m downstream from the spray bar with a diameter of 1 m. The cross-section contracts further in the next 1.1 m, and

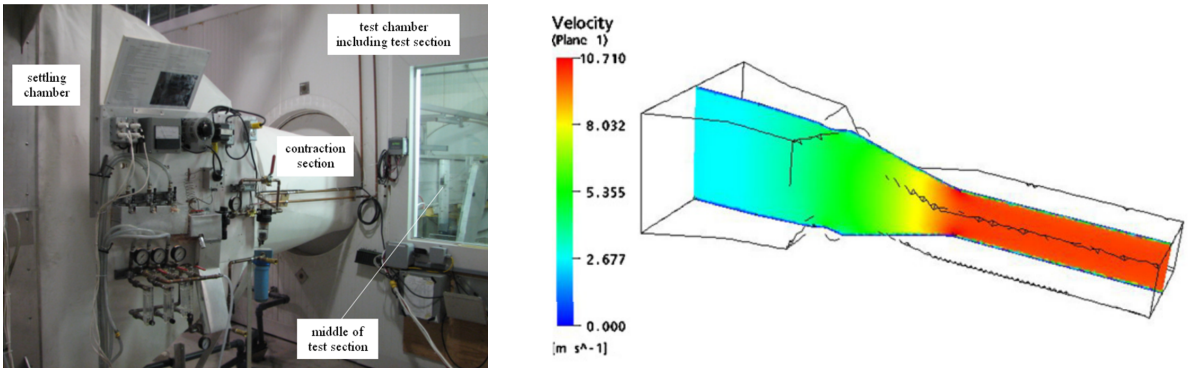

Figure 2.3: The settling chamber, contraction section and test section of the wind tunnel together with its CFX model showing the air velocity field in the middle vertical plane for air velocity in test section of 10 m/s

reaches the final rectangular cross-section with the size of the test section in the following 30 cm. The distance between the spray-bar and the middle of the test section where the icing object is usually placed is 4.4 m. The settling chamber, contraction section and test section are shown in Figure 2.3, together with its model as it is presented in CFX. This figure also shows the calculated air velocity field in the middle vertical plane when the air speed in the test section is set at 10 m/s. The temperature in the test section may be cooled down to $-30°C$. The velocity of circulating air in the test section may reach a maximum of 30 m/s. Water is injected into the air stream through three air-assisted nozzles located on a horizontal spray bar with distances of 20 cm between them. This system can create an aerosol cloud with a median volume diameter (MVD) of 10 to 100 μm along the test section centerline in the middle of test section; however, the MVD may exceed the upper limit in other positions of the test section. The LWC of the produced cloud may be varied from 0.2 to 12 g/m^3 in the middle of test section. Variations in both of these parameters are accomplished through variations in the pressures and thus the flow rates of the water and air lines of the nozzles. These parameters together with the nozzle characteristics have an influence on the liquid jet break-up, and they determine the resulting DSD at the nozzle outlet. This initial DSD is one of the several parameters influencing the DSD and LWC of the aerosol cloud, together with their evolution as the cloud approaches the icing object [69].

2.4.2 Air velocity and droplet velocity measurements

The air velocities and turbulence data at the spray bar and in the middle of test section where the icing object is usually placed were measured by a Pitot tube connected to a differential pressure transducer. Measured velocity data served as input for the CFX calculations which provided the air velocity field in the tunnel. Droplet velocities were also measured in some positions of the test section by a non-intrusive laser optical measurement technique, the particle image velocimetry (PIV). This technique measures the instantaneous velocity components of small particles following the flow. A high-intensity and high-frequency laser is used to produce a light sheet which illuminates the

flow in the target area. A CCD (charge-coupled device) camera captures images, and commercial software is applied to analyze and visualize the flow.

2.4.3 Droplet size distribution and liquid water content measurements

The DSD was measured in the settling chamber by the collargol slide impact method [35] using a tool whose design is based on the one proposed by [21], and its dependence on nozzle-dynamic parameters (NDPs) was scrutinized in detail in [74]. Additional droplet size measurements were performed in [66], at different heights in the middle of the test section. The LWC was measured along the test section centerline in the middle of the test section by the rotating cylinder method [114] for varying air velocities and NDPs [69]. The DSDs obtained close to the nozzles serve as input for the two-phase flow model, while further DSD and LWC measurements in different vertical and streamwise positions in the test section were carried out to study the variation of cloud characteristics in the tunnel and to validate the output of the model.

The methods mentioned in the previous paragraph provide reliable DSD and LWC results; however, they are time consuming, especially the method to obtain a DSD with a sufficient number of droplets. These methods have been replaced by applying an integrated system for icing studies. This system includes two probes for droplet size measurements, the Cloud Droplet Probe (CDP) and Cloud Imaging Probe (CIP). These probes operate based on optical imaging techniques. The CDP is designed to measure particles with diameters between 3 μm and 50 μm, whereas the CIP measures particles ranging in size from 25 μm to 1550 μm. The CIP is a combination probe, also including a heated-element LWC sensor, air temperature sensor, and Pitot tube air speed sensor. The measured data are displayed by the Particle Analysis and Display System (PADS), which is a software package designed to interface with the instruments. The air temperature and air speed may also be entered manually in the PADS. This is recommended for low air speeds because the probe is designed for aircraft, thus providing reliable velocity and temperature measurements at air speeds in the range of 50-150 m/s.

2.5 Vertical and streamwise variations of droplet cloud characteristics

Among the parameters characterizing droplet clouds in atmospheric icing processes and in low-speed wind tunnel, the DSD and LWC are modified the most significantly between different positions. They vary vertically due to gravity, which causes separation of droplets of different sizes, and they also change in the streamwise direction due to cloud deformation, droplet collision and evaporation. This section scrutinizes the effects of these processes in the droplet motion, and in the variation of droplet size and LWC.

Different combinations of the characteristics of the cloud produce unique natural icing environments for specific meteorological phenomena. Cloud characteristics under

Parameter	In-cloud icing (CI)	Freezing drizzle (ZL)
Air temperature (°C)	−10	−5
Air velocity in test section (m/s)	20	10
Relative humidity of air (-)	0.95	0.8
Median volume diameter in settling chamber (μm)	27	62

Table 2.1: Atmospheric parameters assumed under in-cloud icing and freezing drizzle conditions

these phenomena are described in the literature [15, 50, 51]. The LWC and droplet size calibration of the wind tunnel is essentially important before the experimental simulation of atmospheric icing and the prevailing meteorological phenomena [44, 45]. The DSD and LWC in supercooled aerosol clouds produced in low-speed icing wind tunnel were investigated in detail in [69, 74]. In what follows, two specific icing conditions representing in-cloud icing (IC) and freezing drizzle (ZL) are considered in the study. Table 2.1 summarizes the atmospheric parameters which were assumed during these conditions. Turbulence data were measured at the spray bar and in the middle of test section, and the decay of turbulence along the tunnel is assumed according to a decreasing power function based on the suggestion of [111]. Further details on these conditions and related parameters are available in [66, 70].

2.5.1 Droplet trajectory and droplet velocity

Droplet motion is influenced most considerably by gravity among the processes under examination. Therefore, first an individual droplet was tracked in [72] in order to study the effect of gravity on droplet motion. The droplet trajectory and the droplet velocity were determined for different values of the free stream velocity and the droplet diameter. The vertical deflection of droplet trajectory and the vertical component of droplet velocity increased with decreasing free stream velocity and increasing droplet diameter. These observations mean that the largest droplets (close to 100 μm) in low air velocity (5-10 m/s) may reach the bottom of the wind tunnel in the middle of the test section.

Droplet velocity was also determined experimentally by PIV for two different droplet clouds in about a 4.5 cm by 4.5 cm domain located at mid-height of the wind tunnel described in Section 2.4.1 and 0.5 m downstream the middle of test section [70]. The air velocity was 10 m/s in both cases shown in Figure 2.4a and 2.4b, but the DSDs were different with MVDs of 10 μm and 74 μm, respectively. The average of the vertical component of droplet velocity increases in absolute value as the droplet moves downstream and approaches a limit. The averages of the measured vertical components shown in Figure 2.4a and 2.4b are –0.019 m/s and –0.274 m/s, respectively.

Consequently, gravity causes separation of droplets of different sizes, which leads to vertical variation in DSD and LWC. The variation of these parameters will be discussed in the subsequent sections.

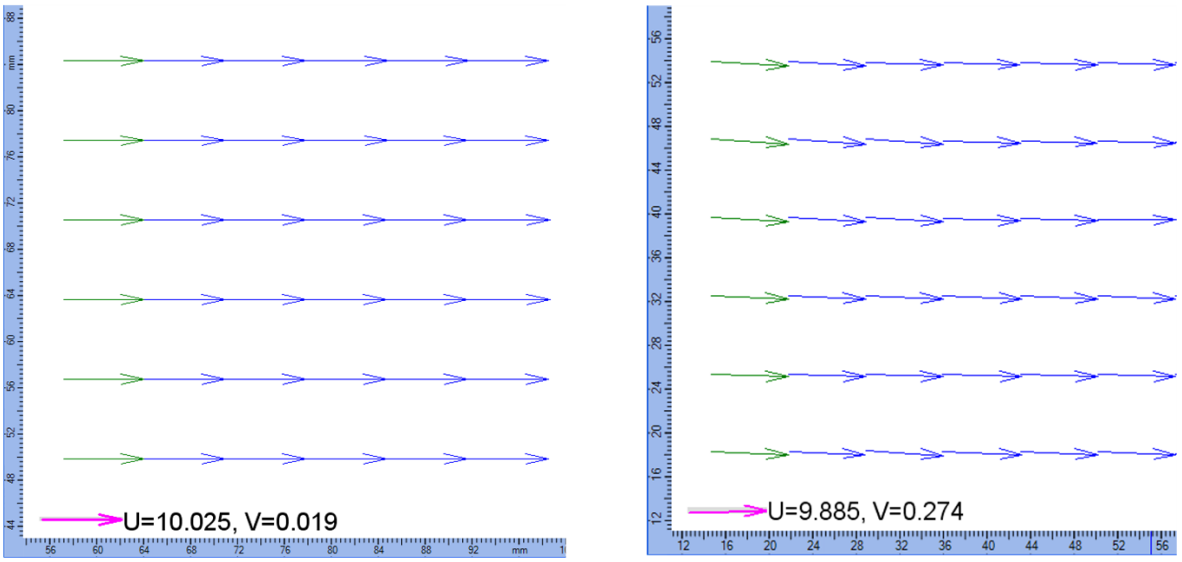

(a) (b)

Figure 2.4: Measured droplet velocities at mid-height and 0.5 m downstream of the middle of the test section in the wind tunnel with a reference velocity on the bottom showing the average values of streamwise components and vertical downward components for air velocity of 10 m/s, (a) MVD is 10 μm, (b) MVD is 74 μm

2.5.2 Vertical and streamwise variations of droplet size

The effects of the processes described in Sections 2.1 and 2.2 on droplet size are summarized as follows. Gravity causes vertical separation of droplets of different sizes as was discussed in Section 2.5.1. Since many of the collisions result in coalescence, the MVD increases due to droplet collision. More precisely, the number of small droplets decreases, the number of middle-size droplets does not change significantly, while the number of large droplets increases [72]. Evaporation and cooling reduce droplet size and temperature; however, once a droplet approaches its equilibrium temperature those effects are significant only in a limiting case of icing conditions, i.e. when air temperature is close to 0°C and air relative humidity drops below 0.75 [73]. Turbulent dispersion modifies droplet trajectories, and consequently, the spatial variation in DSD and LWC [66].

The vertical variation of droplet size was studied in the middle of the test section of the wind tunnel. The DSD was measured at four different positions: $y = +7$ cm, 0 cm, -7 cm, and -14 cm, where y denotes vertical distance and $y = 0$ is the mid-height of the test section, which appears at the same level as the spray bar with the nozzles. Figure 2.5a and 2.5b present the measured and calculated MVDs for CI and ZL conditions, respectively. The results clearly show the difference between the sizes of droplets as they occur under these conditions, and also the vertical separation of droplets of different sizes due to gravity. As discussed in Section 2.5.1, the effect of gravity is important for low air speeds, which is confirmed by the results presented in Figure 2.5. Nearly the same MVDs are measured at different vertical levels for CI when the air speed is 20 m/s, although a slight increase towards the bottom of the tunnel may be observed (less than 20% between

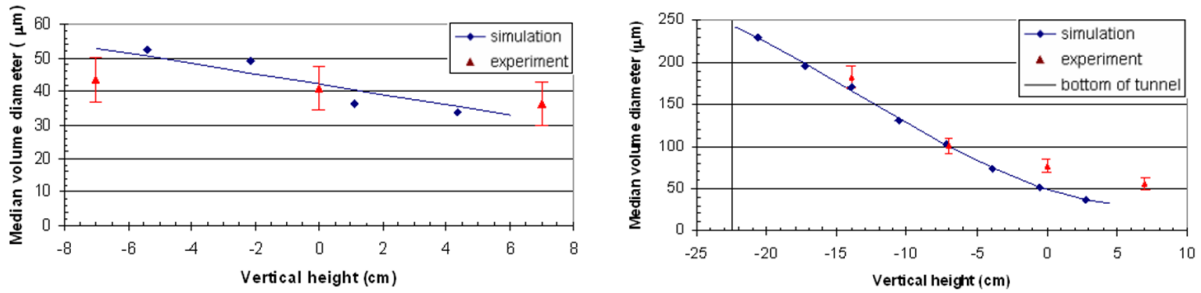

(a) (b)

Figure 2.5: Calculated and measured MVDs at different vertical positions, (a) in-cloud icing (CI) conditions, (b) freezing drizzle (ZL) conditions

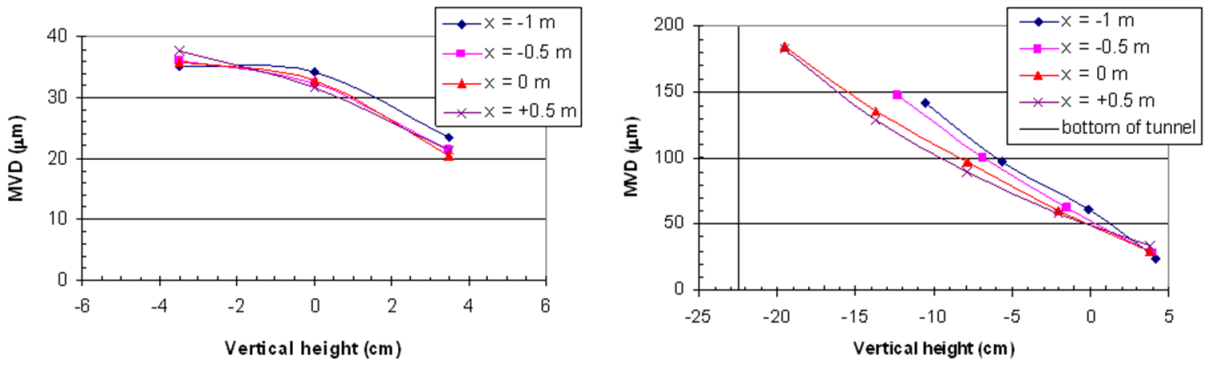

(a) (b)

Figure 2.6: MVDs calculated at different streamwise (x) and vertical positions; (a) in-cloud icing (CI) conditions, (b) freezing drizzle (ZL) conditions

the utmost and bottommost locations). Furthermore, no value appears at $y = -14$ cm, because the aerosol cloud is not extended until this height, and no droplets were captured here. For ZL, however, when the air speed is 10 m/s, and droplets are larger, the MVD increased significantly towards the bottom of the tunnel (more than three times greater at the bottom than at the top), and many droplets were captured even at the location $y = -14$ cm. These tendencies are estimated closely by the model; although a shortcoming may also be observed: the underestimation of droplet size in the top half of the vertical section. It was pointed out in [66] that the model provided improved results with the consideration of turbulence dispersion. The error bars correspond to the measurement error which was evaluated to be $\pm 4.5\text{mm} \pm 5\%$ in [74].

The MVDs calculated at different streamwise and vertical positions are shown in Figure 2.6a and 2.6b for CI and ZL conditions, respectively. The coordinate x increases in the streamwise direction and $x = 0$ denotes the middle of the test section. It may be observed that the droplet size increases toward the bottom of the tunnel at the same section; whereas the MVDs at the same height are approximately constant in the streamwise direction for CI conditions, and they decrease for ZL conditions. This result is explained by the vertical component of droplet velocity. The large droplets move closer and closer to the bottom of the tunnel so that the MVD is greater at a lower height in

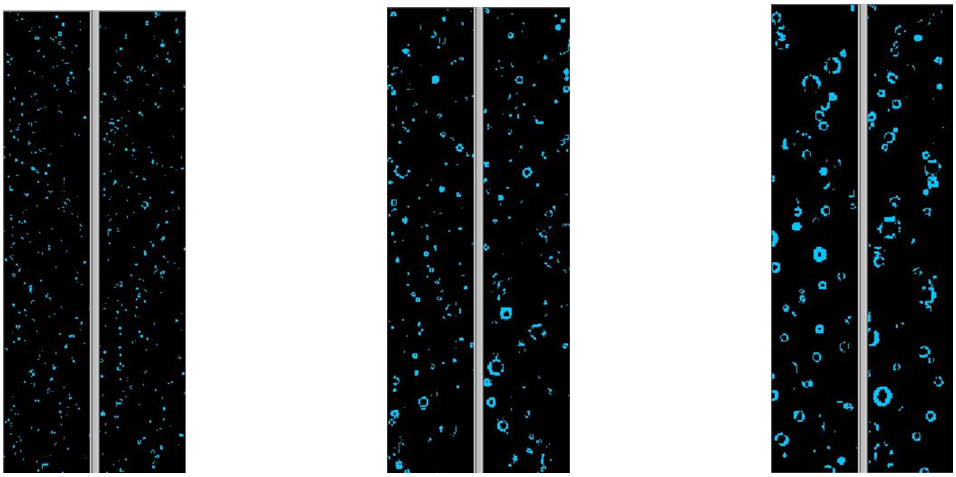

(a) (b) (c)

Figure 2.7: Images captured during droplet size measurements; (a) in-cloud icing (CI) conditions, $y = 0$ cm, (b) freezing drizzle (ZL) conditions, $y = 0$ cm, (c) freezing drizzle (ZL) conditions, $y = -7$ cm

the same vertical section, and it decreases at the same height as the droplet cloud moves downstream. Farther downstream, the largest droplets will occupy the bottommost part of the tunnel where the cloud was not extended upstream (see the domain below the height of −15 cm in Figure 2.6b); and finally they reach the bottom when they are withdrawn from further calculation. The comparison of Figure 2.6a and 2.6b reveals that the droplet size varies in the vertical direction to a significantly lower degree for CI conditions, and that the variation in the streamwise direction is negligible. In this case the droplets are smaller and the air velocity is higher; consequently, the vertical separation of droplets according to their size is less noticeable. The droplet cloud expands vertically to a lower degree and it remains more uniform.

Typical DSDs are illustrated visually in Figure 2.7, where images captured during droplet size measurements in the middle of the test section ($x = 0$ m) are presented. Figure 2.7a and 2.7b show droplets observed at mid-height of the test section ($y = 0$ cm) in the cloud simulating CI and ZL conditions, respectively. Figure 2.7c shows droplets at $y = -7$ cm for ZL conditions. These results confirm that droplet size is greater under ZL conditions than under CI conditions; furthermore, the droplet size increases toward the bottom of the tunnel when large droplets are present.

Figure 2.8 compares four DSDs measured at the nozzle outlet and in the mid-height of the test section for both conditions examined. The aerosol cloud modelling ZL includes larger droplets even initially than the cloud produced under CI conditions. Droplets increase in size in both cases as they reach the test section, which is mainly a consequence of droplet collision, because two smaller droplets form a larger one when the collision outcome is coalescence. The size of an individual droplet decreases due to evaporation, but the decrease in the size of large droplets is negligible, while the smallest droplets are evaporated completely; therefore, this phenomenon may result in either increasing or decreasing droplet size, depending on cloud characteristics.

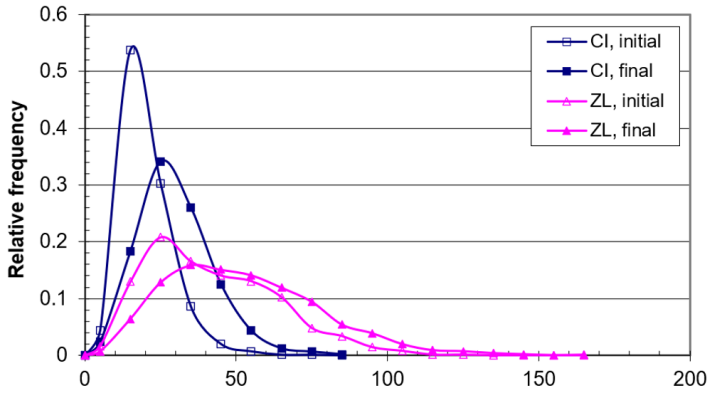

Figure 2.8: Measured DSDs under in-cloud icing (CI) and freezing drizzle (ZL) conditions at the nozzle outlet (initial) and in mid-height of the test section (final)

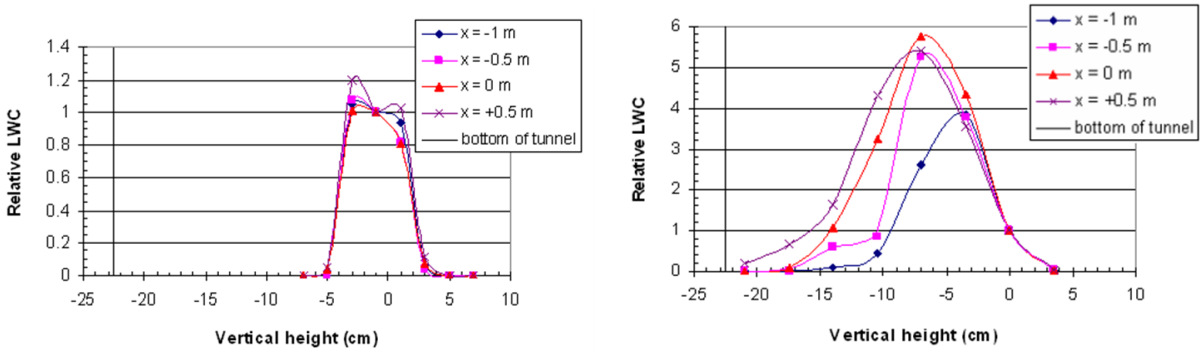

(a) (b)

Figure 2.9: Relative LWC calculated at different streamwise (x) and vertical positions (its value is 1 at $y = 0$ cm); (a) in-cloud icing (CI) conditions, (b) freezing drizzle (ZL) conditions

2.5.3 Vertical and streamwise variations of liquid water content

The two-phase flow model is two dimensional; therefore, it cannot determine the mass of liquid water in a real three-dimensional unit volume. However, the ratio of masses of all the droplets in different computational domains of the same size may be obtained. Thus, the model is applicable to calculate the ratio of LWCs at different positions in the same cross section, and thereby a vertical distribution of LWC may be determined. Measured and calculated vertical distributions of LWC were compared in [72] for different air velocities; while the vertical distributions at different streamwise positions were determined in [70] for CI and ZL conditions. The cross section in the streamwise positions is divided vertically into domains with constant size. The values of relative LWC in each domain is determined so that the relative LWC equals to 1 in the domain including the position $y = 0$ cm. Figure 2.9a and 2.9b show these calculated values for CI and ZL conditions, respectively.

The ratio of LWCs measured at two different vertical positions, $y = -7$ cm and $y = 0$ cm, are listed in Table 2.2, in the four streamwise positions examined. According to measured results, the LWC at $y = -7$ cm is 0.4-0.7 times that measured at $y = 0$ cm for CI conditions, and this ratio increases in streamwise position. The same ratio is 1.6-2.1

Streamwise position	LWC_{-7}/LWC_0(CI)	LWC_{-7}/LWC_0(ZL)
−1 m	0.44	1.91
−0.5 m	0.42	1.57
0 m	0.59	1.86
+0.5 m	0.71	2.12

Table 2.2: The ratio of LWCs measured at $y = -7$ cm and at $y = 0$ cm (LWC_{-7}/LWC_0) in four streamwise positions for in-cloud icing (CI) and freezing drizzle (ZL) conditions

for ZL conditions, and again, this ratio increases as the cloud moves downstream in the test section. The difficulty in comparing the measured and calculated results is that, in both cases, the change near the cloud boundaries is abrupt (see the steeply increasing or decreasing curves at the edges of the cloud, i.e. in the domains including the vertical positions $y = +3$ cm and $y = -3$ cm in Figure 2.9a and $y = 0$ cm in Figure 2.9b. Thus, the LWC is significantly different in the top and in the bottom of the same domain near the edges of the cloud. However, it may be observed in Figure 2.9a that the relative LWC is in the range of 0.4-0.7 at $y = -4$ cm for CI conditions. According to Figure 2.9b, the LWC around the position $y = -7$ cm reaches its maximum, and the ratio 1.6-2.1 listed in Table 2.2 is the ratio obtained in the calculations if this LWC is compared with that at the position $y = -2$ cm instead of $y = 0$ cm. Consequently, the model predicts that a 7-cm-long vertical domain of the cloud is extended to about 4-5 cm only. Therefore, it may be concluded from this comparison that the model provides a qualitatively accurate prediction of the streamwise and vertical variations of LWC; however, it underestimates the vertical extent of the cloud where small droplets prevail.

Figure 2.9 also shows clearly that the droplet cloud is significantly more extended vertically for ZL than for CI conditions, when more droplets approach the bottom of the tunnel leading to increasing LWC in the bottom half as the cloud moves downstream in the test section.

2.6 New results

Main contribution 1 *A composite collision outcome model was developed, which predicts the outcome of binary droplet collisions when modelling two-phase air/dispersed water flows. In particular, the condition for transition between two collision outcomes, coalescence after minor deformation and bounce, has been proposed based on the underlying physics. Coalescence after minor deformation takes place if two conditions are satisfied. (1) The thickness of the gas film trapped between the droplets has to be reduced to a critical thickness for breaking up the gas film and resulting in the coalescence of droplets. (2) During the sliding interaction of droplets coalescence takes place only if the droplets do not pass near each other due to the sliding motion before the film thickness reduces to its critical value. The minimum film thickness that the gas layer may reach is estimated using characteristic values of the involved quantities, whereas the time required for the gas layer to be reduced*

to the critical thickness at rupture is estimated using time-scale analysis. The two-phase flow model verifies these two conditions in each collision case. Criteria applied in the composite collision outcome model to determine the transition between other regimes of collision outcome are based on formerly proposed conditions.
Related publication: Kollár and Farzaneh (2011) [70]

Main contribution 2 *Characteristics of droplet clouds that are responsible for atmospheric icing of structures determine the type, mass and shape of ice accretion. Natural aerosol clouds under icing conditions were modelled theoretically and experimentally in a low-speed icing wind tunnel by creating a two-phase air/dispersed water flow. The modelling procedure proposed considers several factors that modify the characteristics of the cloud including droplet collision and coalescence, evaporation and cooling, gravitational settling, and turbulent dispersion of the dispersed phase. Results provide the vertical and streamwise variations of droplet size and liquid water content under different icing conditions. These parameters were compared for two essentially different icing conditions: in-cloud icing that is characterized by small droplets (MVD of 27 μm in the particular example considered) and relatively higher air velocity (20 m/s); and freezing drizzle conditions with greater droplet size (MVD of 62 μm) and relatively lower air velocity (10 m/s). Observations show that the vertical component of droplet velocity and the resulting vertical separation of droplets of different sizes are almost negligible under in-cloud icing conditions. The variation of MVD in vertical positions in the test section of the wind tunnel is only* $\pm 20-30\%$ *compared to that at mid-height of the test section. However, droplet size increases significantly towards the bottom of the tunnel under freezing drizzle conditions, the MVD at 20 cm below the middle of the test section may increase to about 4 times greater value than at mid-height. On the other hand, droplet size at the same vertical level decreases downstream in the test section, because large droplets move toward the bottom of the tunnel. This decrease may be 10 to 30% in a streamwise distance of 1.5 m, depending on the vertical position. The MVD averaged over all heights in a vertical section is always greater in the test section than in the settling chamber, which results mainly from the coalescences following droplet collisions. Turbulent dispersion amplifies the effect of droplet collision and causes the occurrence of droplets in a wider vertical domain, whereas the influence of evaporation becomes more significant when air temperature increases towards* $0°C$ *or relative humidity of air decreases.*
Related publications: Kollár and Farzaneh (2007) [66], Kollár and Farzaneh (2011) [70]

Chapter 3

Conductor vibration following ice shedding

Transmission line conductors are suspended in the atmosphere, and they are exposed to dynamic loads due to natural phenomena or to human intervention. These phenomena include wind, ice, or impact from an external source. The dynamic effects may damage some elements of the transmission lines, and thereby essentially reduce the range of operation and lifetime of the structure. Such problems justify the effort to study the sources of dynamic loads and the process of the resulting vibration, and to develop solutions in order to reduce the undesired consequences. This chapter summarizes wind-induced conductor motion briefly, and then focuses on the conductor vibration that follows ice shedding. Different ice shedding scenarios are discussed including its numerical and experimental modelling. The dynamic effects of ice shedding are studied on a single conductor, on conductor bundles, and on conductors connected with interphase spacers. The main interest is to determine conductor rebound height following ice drop together with conductor tension and the transient dynamic forces that act at the suspension during vibration.

3.1 Phenomena inducing conductor vibration

This section describes briefly the phenomena and consequences of wind-induced conductor motion and conductor vibration following ice shedding. Since the focus of the present chapter is the latter one, approaches to model this phenomenon will also be summarized.

3.1.1 Wind-induced conductor motion

Wind-induced conductor motion includes those types of cyclic motion, which gain energy from wind forces applied on the conductor. Such motion is divided into three categories, namely aeolian vibration, galloping, and wake-induced oscillation. They are distinguished by the mechanism that initiates the vibration, by the amplitude and frequency of vibration, and by the effects upon the equipment of the transmission line [25, 29].

	Aeolian vibration	Galloping	Wake-induced oscillation
Cause	alternate shedding of vortices	crosswind acting upon asymmetrically iced conductor	bundled conductors exposed to wind
Frequency	3-150 Hz	0.08-3 Hz	0.15-10 Hz
Amplitude (expressed in conductor diameter)	0.01-1	5-300	0.5-80
Damage	metal fatigue of conductor and shield wire strands	conductor, support hardware, insulators	suspension failure, crushing of conductor strands, fatigue of spacers

Table 3.1: Main characteristics of wind-induced conductor motions

The basic cause of aeolian vibration is the regular shedding of vortices from the conductor. This vibration develops when low-velocity wind (below 7 m/s) is present, and it is characterized by high frequency and low amplitude. The frequency range may vary from 3 to 150 Hz, and the amplitude rarely exceeds one conductor diameter, usually decreasing for higher-velocity winds. Consequently, this vibration does not cause damage in a short time, but it leads to metal fatigue of conductor and shield wire strands if the cyclic bending repeats many times.

Galloping is a movement-induced excitation occurring when ice accretion modifies the circular shape of the conductor and generates an aerodynamically unstable profile. It is usually caused by moderately strong, steady crosswind (7 to 18 m/s) acting on the asymmetrically iced surface. Aerodynamic explanation of the galloping phenomenon was first provided by [19]. Galloping is a high-amplitude, low-frequency vibration. The frequency is in the range of 1 Hz, and the amplitude may reach several hundred times the conductor diameter, peak-to-peak amplitudes up to 15 m have been reported. This type of conductor motion can cause much damage to many elements of the transmission line in the shortest time, even after a couple of hours.

Wake-induced oscillation occurs on bundled conductors exposed to moderate to strong crosswinds (4 to 18 m/s). It arises from the effect of the windward conductor on the leeward conductor that is in the wake of the previous one. The frequency and amplitude of this vibration are in the mid-range if compared to the other two types of wind-induced conductor motion. It usually causes wear in suspension hardware or fatigue of spacers, but in the worst cases it may lead to suspension hardware failure or crushing of conductor strands due to clashing.

Main characteristics of the three types of wind-induced conductor motion is summarized in Table 3.1. Huge research effort has been done on studying and modelling wind-induced conductor motions, and developing line protection methods that help reducing

the damages due these types of vibration. The review of this research and development is out of the scope of this dissertation, but some methods, developed to attenuate vibration and presented in Section 4, are applicable to suppress vibration and thereby reduce the harmful effects of wind-induced motion as well.

3.1.2 Phenomenon and consequences of conductor vibration following ice shedding

Ice shedding from transmission-line conductors may cause serious dynamic effects on the power line elements. Ice shedding occurs when ice builds up on the conductor and subsequently sheds due to changes in the ambient conditions. Strain energy is stored in the conductor that is deformed due to the ice deposit, and when this load drops from the conductor, the strain energy is converted into kinetic energy and then into potential energy. The falling of large ice chunks results in high-amplitude vibration of the de-iced conductor, giving rise to important dynamic forces acting on the transmission line. Initially, the amplitude of vibration is comparable to that during galloping, but then the vibration decays mainly due to structural damping of the conductor and to the air resistance over the conductor displacement.

The damage as a consequence of such vibration may be considerable. High conductor rebound may trigger flashovers between adjacent phases, whereas the excessive dynamic load may cause suspension failure and even cascading damage to several towers [29]. Spacer dampers in conductor bundles help maintain the distance between the subconductors and reduce the amplitude of aeolian vibration and subspan oscillation. On the other hand, interphase spacers may contribute to avoiding the contact between phases. However, their application increases the load on the conductors and on the related structure. When a subconductor in a multiconductor bundle sheds, the rotation of the bundle may also be significant, leading to bundle collapse in extreme cases. Bundle collapse occurs when the bundle rotation exceeds a critical angle so that the bundle loses its stability and does not untwist itself after load removal [85, 93]. A review of ice-related dynamic problems on overhead lines, including ice shedding and bundle rolling, is provided in [41]. These problems justify the particular interest in cold climate regions to predict the conductor jump height and transverse movement as well as the tension developing in the conductor and at the suspension during vibration following ice shedding.

Dynamic effects on the power line elements depend on the ice shedding process. Ice may shed in small pieces and the shedding propagates along the span or part of the span with its associated sudden release of the additional weight of the ice. In other cases, the ice detachment propagates along the span, but the detached ice chunk does not fall immediately because it remains connected to other parts of the ice accretion, and when it finally falls, it exerts an additional pull on the conductor due to its downward gravity acceleration. A third possibility is the sudden ice shedding from the entire span or from a long part of it, when a big ice chunk is detached from the conductor and falls suddenly [76]. Sections 3.2-3.4 are devoted to the numerical and experimental modelling of different ice shedding processes from different line configurations. The processes modelled include

sudden ice shedding and ice shedding propagation from single conductor, from conductor bundles with spacer dampers, and from conductors connected with interphase spacers.

3.1.3 Modelling conductor vibration following ice shedding

Field observation of ice shedding is a difficult task, because of the unforeseeable and non-repetitive occurrence of the phenomenon. Therefore, great effort has been made for several decades to simulate ice shedding numerically and experimentally on small-scale or full-scale test lines in order to understand the dynamic effects of ice shedding. Morgan and Swift [89] modelled ice shedding experimentally by load dropping tests on a five-span section and observed the resulting conductor jump. Ice shedding from a two-span section of a single conductor was modelled numerically in [49] using the commercial finite-element analysis software ADINA [3], and model predictions were validated on a small-scale laboratory model. Roshan Fekr and McClure [106] studied the effects of ice thickness, partial shedding, and different line parameters on the dynamic response of ice shedding on transmission lines by a similar numerical approach. Their model was also used to simulate a tower failure which occurred in a 220 kV transmission line following ice shedding [107]. The vibration of a two-span section due to ice shedding from one span was investigated in [64] by considering different types of ice. Kálmán et al. [55] proposed a model to simulate the mitigation of ice failure and ice shedding in a one-span section due to pulse-type excitation. Propagating ice shedding was simulated on a full-scale test line in [122]. In more recent developments, formulae and methods to directly calculate conductor rebound height after ice shedding were also proposed in the literature. Yan et al. [132] suggested a formula based on numerical simulations. Wu et al. [129] developed a theoretical method to determine rebound height, and previously proposed formulae were verifed and modifed in [43]. Xie et al. [130] studied the dynamic effects of ice shedding experimentally on a test system including two spans and three towers. They analyzed the dynamic behaviour of the conductor following different ice-shedding scenarios, where the tower was also designed in the experimental set-up. Dynamic effects of ice shedding influence the transmission-line tower as well. Gao et al. [31] analyzed the dynamic response of wine-cup shape power transmission tower-line system due to ice shedding, and carried out progressive collapse simulation based on numerical modelling. Ice shedding may induce tower collapse, which was simulated numerically in [82]. They also analyzed the effects of span length and insulator length on the consequences of ice shedding.

Sections 3.2-3.4 present the development on numerical and experimental models of vibration of bundled conductors following ice shedding. First, a spacer model is developed and the dynamics of bundled conductors following ice shedding from one subconductor is analyzed [67]. Then, the numerical model is improved and a small-scale experimental model is constructed to simulate sudden ice shedding [71]. Finally, in the third part, the numerical and experimental models are further improved so that they would be applicable to simulate ice shedding propagation. The numerical model is also applied for several spans of conductors linked with interphase spacers [75, 76].

3.2 Numerical modelling of vibration of bundled conductors following ice shedding

Former numerical models of ice shedding are improved by developing and involving a model of spacer dampers that are applied in bundled conductors. Then, the dynamics of bundled conductors following ice shedding from one subconductor is analyzed with a special emphasis on how the amount of ice, the distance between adjacent spacers, and the number of subconductors influence the severity of the vibration [67].

3.2.1 Bundled conductors with spacers

Bundled conductors are frequently used for overhead transmission lines where the individual conductors are connected by spacers. The particular construction of each spacer varies depending on the manufacturer, but all of them are designed so as to maintain a constant distance between the subconductors. Spacers were applied for electrical reasons originally, but they also play an important role from the mechanical point of view, since they help reduce the severity of conductor vibration. A spacer of typical design consists of a rigid central frame to which arms are attached via flexible joints. Each of these arms grips one of the subconductors by means of a clamp located at the free end of the arm. The geometrical and physical parameters of some spacers used in bundles of four conductors are provided in [39] where the authors also present a test program aimed to compare the performance of different spacers. Edwards and Boyd [24] summarizes design requirements of spacers including basic engineering requirements, general design parameters, and physical requirements. A survey on spacers including types, materials, design characteristics, test methods and field experience is presented in [14].

Spacers are subject to various types of loads due to mechanical tensions in the cables, short circuits or high-amplitude vibrations. The highest cable tension and stress during cable vibration usually develop near the suspension clamps as well as in the neighborhood of the spacer clamps. Hagedorn et al. [5, 38] determined the forces acting at the spacer clamp and developed a mathematical model for vortex-induced vibrations in bundled conductors with spacer dampers. The severity of wake-induced oscillations of bundled conductors was examined on a full-scale experimental line in [40]. In what follows, a finite element model of spacers is constructed and is integrated to the model of one span of an overhead transmission line with bundled conductors. This model makes it possible to calculate the forces acting at any part of the conductors including the vicinity of the spacer during the vibration induced by ice shedding from any subconductor.

3.2.2 Finite element model of a single span of bundled conductors with spacers

The finite element model of a single span of bundled conductors with ice load is constructed using ADINA [3]. The cable model and ice model are based on the ones developed in [49] and [106], and will be described below together with the spacer model.

Conductor

Two-node isoparametric truss elements with large kinematics are used for conductor modelling. A constant initial pre-strain corresponding to the installation conditions is prescribed as an initial condition for all conductor elements. This initial strain is obtained from the following formula:

$$\epsilon_0 = \frac{T_0}{AE} \tag{3.1}$$

where A is the cross-section of the conductor, E is the Young's modulus, and T_0 is the tension that may be determined from the equilibrium of the conductor under its own weight [47]. Conductor material properties are defined for tension only, not allowing compression and assuming Hookean small strain behaviour in tension. The conductor is assumed to be perfectly flexible in bending and torsion. The mesh selected for the conductor contains 100 truss elements in each conductor, which was found to be adequate.

Conductor damping is considered in the model by defining nonlinear spring elements. The damping force is given in the form $|F_D| = C\left|\dot{U}\right|^N$, where $\dot{U}$ is the relative velocity between the element end nodes. The structural damping of the conductor is modelled by applying viscous dashpot elements in parallel with each conductor element with exponent $N = 1$ and viscous damping constant:

$$C_S = 2\zeta\sqrt{AE\mu} \tag{3.2}$$

The ζ is the damping ratio, μ is the mass per unit length of the conductor or the conductor-ice composition. The damping ratio is chosen as 2% for the bare cable and 10% for the iced cable following the recommendation in [106]. Aerodynamic damping is considered by defining dashpot elements between each conductor-element node and the ground, and applying them to the vertical motion of the conductor. The exponent N is equal to 2 in this case, while the damping constant is calculated as follows

$$C_A = \frac{1}{2}C_D\rho A_p \tag{3.3}$$

where C_D is the drag coefficient, ρ is the air density, A_p is the projected area. The drag coefficient, C_D, is assumed to be 1.25, as proposed in [101].

Ice load and ice shedding

Ice load is taken into account by assuming that conductor element density in the static analysis increases proportionally with the weight of ice load. In order to simulate ice shedding, density of the subconductor where ice sheds from is decreased in the dynamic analysis [106]. Thus, the density of an ice-shedding conductor is different in the static and in the dynamic analysis, which causes an abrupt change in the mass matrix and leads to vibration. The density of ice depends on the type of ice that accumulates on the conductor. The model considers glaze ice accretion, which usually causes the highest ice load and which is assumed to have a constant density of 900 kg/m^3.

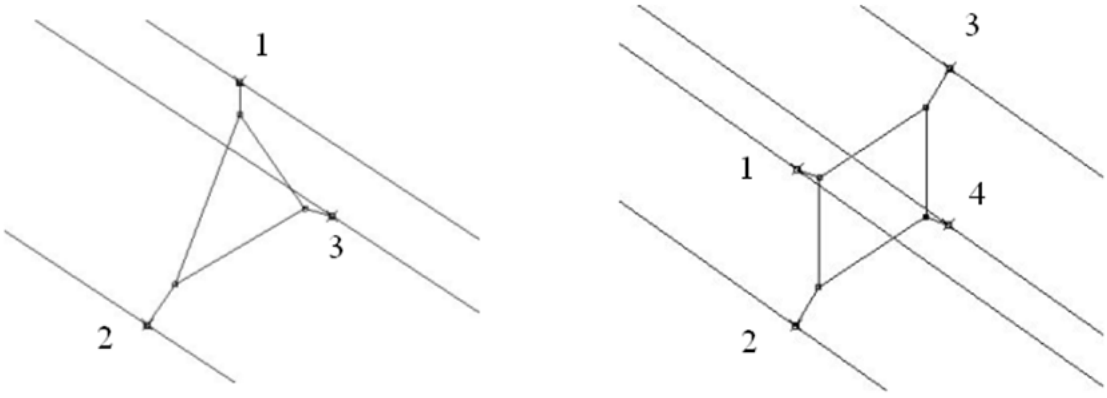

(a) (b)

Figure 3.1: Models of spacers applied in conductor bundles; (a) triple bundle; (b) quad bundle

Spacer

The spacer model of the present approach was first introduced in [65], where spacers were modelled by two-dimensional beam elements. This approach was improved in [67] by considering the flexibility and damping properties of the spacer. Two-node truss elements associated with nonlinear elastic material are applied in order to achieve this goal. The calculation of mass, damping, stiffness matrices and load vector, as well as the construction of the equations of motion for truss elements are discussed briefly in [65], and in detail in [9]. A cubic stress-strain curve describes the material of spacer arms which are allowed to rotate a few degrees around the joint with increasing resistance until the rotation is blocked. Further deformation may occur only by the elongation of the material, which is modelled by a linear stress-strain curve. Thus, the force–deformation relationship, $F_s(\Delta l)$, which describes the flexibility of the spacer, is given by the following formula:

$$F_s = \begin{cases} c_{s3}\Delta l^3 & \text{if} \quad \Delta l < |\Delta l_{cr}| \\ c_{s0} + c_{s1}\Delta l & \text{if} \quad \Delta l \geq |\Delta l_{cr}| \end{cases} \tag{3.4}$$

where Δl_{cr} is the increase of spacer length at the maximum angle of arm rotation. The constants, c_{s0}, c_{s1} and c_{s3} are obtained from the conditions that the tangent of the force–deformation relationship at the connection, Δl_{cr}, should be equal to $E_s A_s/l_s$, and that the cubic and linear functions take the same value at the connection. The parameters, E_s, A_s and l_s are the Young's modulus, cross section and length of spacer, respectively. The stress-strain relationship may readily be deduced from Equation (3.4).

Spacers for a twin bundle are simple rods clamped to a conductor at each end, whereas for a triple and for a quad bundle they consist of 6 and 8 truss elements, respectively. The models of spacers for triple and quad bundles are shown in Figure 3.1. The distance between two subconductors is 0.5 m, and the spacer dimensions are chosen so that mass and inertia are in a realistic range in accordance with the spacers examined in [39]. The

Parameter	Unit	Condor	Bersfort
Conductor diameter	(mm)	27.8	35.6
Cross-sectional area of the conductor	(mm^2)	455.1	747.1
Weight per unit length of the conductor	(N/m)	14.9	23.2
Conductor density	(kg/m^3)	3337	3171
Young's modulus of the conductor	GPa	68.3	67.6
Span length	(m)	200	200
Sag of unloaded conductor	(m)	6	6
Initial conductor tension	(kN)	12.43	19.39

Table 3.2: Geometrical and material data of conductors and span

material properties are defined to be similar to those of aluminum (density of 2700 kg/m^3, Young's modulus of 70 GPa and Poisson's ratio of 0.35), and the arms are associated with the nonlinear elastic material described in the previous paragraph.

The damping properties of spacers are modelled by nonlinear spring elements with exponent $N = 1$, and the damping constant may be obtained from Equation (3.2) after substituting the material properties of the spacer. The damping ratio was chosen to be 0.2, which is based on the values reported in [39].

3.2.3 Results and discussion

Five different configurations of a single span of an overhead transmission line with fixed end-points are modelled in [67]: single cable, twin bundle with spacers in the horizontal plane, twin bundle with spacers in the vertical plane, triple bundle and quad bundle. Ice sheds from one subconductor of the bundle, which is the upper cable in the triple bundle (subconductor 1 in Figure 3.1a), and one of the upper cables for the quad bundle (subconductor 1 in Figure 3.1b). Ice shedding from lower cable and ice shedding from upper cable are both simulated for the twin bundle with spacers in the vertical plane. The conductors used for the simulations are Condor ACSR 54/7 and Bersfort ACSR 48/7, which are made of 54 and 48 aluminum alloy strands, respectively, reinforced with a seven-wire steel core. Conductor data and parameters describing the span in static equilibrium are listed in Table 3.2. Six load cases are examined with ice thickness ranging from 10 mm to 60 mm whose maximum was chosen to correspond with the ice load considered as the extreme case under natural conditions. The number of spacers or the distance between adjacent spacers in the span under scrutiny is also varied in consecutive simulations. The application of 1, 2, 3, 4 and 5 spacers corresponds to a respective constant distance of 100, 67, 50, 40 and 33 m between adjacent spacers. These values cover the range of 40 to 60 m, which is generally used on the Hydro-Quebec transmission lines, although unequal sub-span lengths were not considered.

This section discusses the effects of three parameters, (i) ice thickness, (ii) distance between adjacent spacers, and (iii) number of subconductors in the bundle. The parameters calculated describe the characteristics of the vibration induced by ice shedding, more

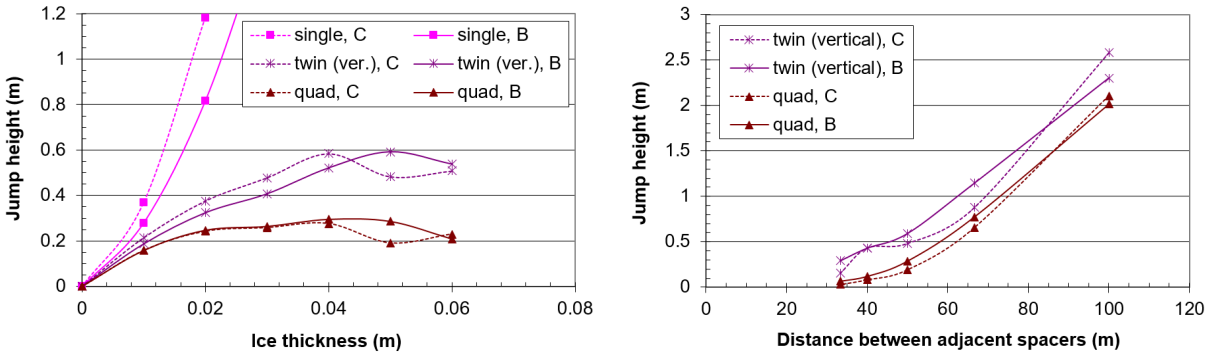

(a) (b)

Figure 3.2: Maximum jump height of the ice-shedding conductor above unloaded position, C – Condor conductor, B – Bersfort conductor, (a) distance between adjacent spacers: 50 m, (b) ice thickness: 50 mm

precisely, (i) the maximum jump height of the conductor which ice sheds from, (ii) the maximum drop of the conductor(s) which remain loaded, and (iii) the maximum conductor tension arising during the vibration.

Maximum jump height of the conductor which ice sheds from

Ice thickness was varied between 10 mm and 60 mm, and the conductor bundle was connected by 3 spacers in the first set of simulations. Figure 3.2a shows values of maximum jump height of the ice-shedding conductor above its unloaded position, which arises during one of the first few cycles of vibration. It is clear from this figure that there is a steep increase in jump height for a single conductor with increasing ice thickness. This increase is significantly slower for twin bundles, and less than 0.1 m for triple and quad bundles, for ice thickness of 30 mm and more. The results obtained for twin bundles in horizontal plane are close to those in vertical plane. Likewise, similarity was observed between maximum jump heights in triple and quad bundles. The jump height of a single conductor in the extreme case, i.e. after the shedding of 60-mm-thick ice chunk was calculated as 5.84 m, and 10.25 m, for the Bersfort and the Condor conductor, respectively. However, the jump heights of bundled conductors of these two types are in the same range.

The number of spacers was varied between 1 and 5, while ice thickness was set to 50 mm in the next series of simulations. It can be observed in Figure 3.2b that the maximum jump height of the ice-shedding conductor increases with the distance between adjacent spacers and that the jump height is smaller for higher number of subconductors.

Maximum drop of the conductors which remain loaded

The lowest position during vibration of the conductor bundle is reached by one of the conductors which remain loaded. Figure 3.3a shows that the maximum drop below the unloaded position increases proportionally with ice thickness, and it is about 30-40% greater for Condor conductor than for Bersfort conductor. The curves representing the maximum drop for different bundles of the same conductor almost coincide, which can

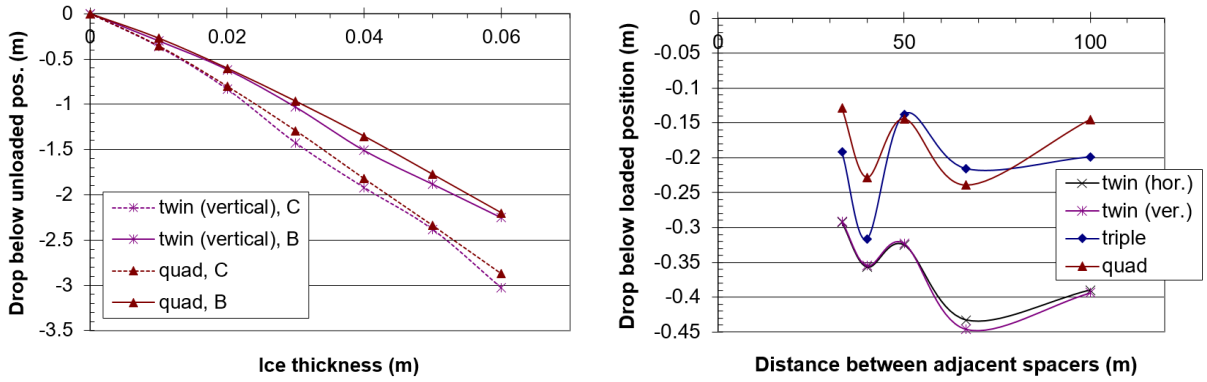

(a) (b)

Figure 3.3: Maximum drop of the conductor which remains loaded (a) below unloaded position, C – Condor conductor, B – Bersfort conductor, distance between adjacent spacers: 50 m, (b) below loaded position, Bersfort conductor, ice thickness: 50 mm

be explained by the following fact. The drop below the loaded position is significantly lower than the increase in the sag due to ice load (around 10-15%), and the increase of the sag due to ice load is approximately the same for each configuration. However, the decrease of maximum drop below the loaded position with the number of subconductors is significant.

A similar tendency may be observed in Figure 3.3b, where the maximum drops below the loaded position are shown as a function of the distance between adjacent spacers. The maximum drop in absolute value decreases with the number of subconductors in the bundle. However, the difference between Figures 3.2b and 3.3b is striking. The maximum jump height increases with the distance between adjacent spacers, while the maximum drop is significantly greater for distances of 40 and 67 m (4 and 2 spacers, respectively), than for distances of 33, 50 and 100 m (5, 3 and 1 spacer(s), respectively). This result is due to the fact that there is no spacer at mid-span when the number of spacers is even, so that the maximum drop occurs at mid-span where the cable drop can be considerably greater. If the maximum drop below the unloaded position is considered, then its value varies by a maximum of 5% only for an odd number of spacers, and is about 5-15% greater when the number of spacers is even.

If ice sheds from the lower subconductor while the upper one remains loaded, then the possibility of contacts between the vibrating conductors will increase as compared with the case when ice sheds from the upper subconductor (in case of a heavy ice load, they will be in contact even in static equilibrium). However, since the maximum jump and the maximum drop usually do not appear at the same location along the span, the distance between two corresponding points involving two subconductors should be calculated during vibration in order to know when the above-mentioned contact may occur. The selected points are the mid-points of the sub-spans closest to the middle of the span, because that is where the vibration is expected to have the highest amplitude. The variation of minimum distance between these points with ice thickness and spacer distance was analyzed in the case of a twin bundle in vertical plane in [67]. Vibrating

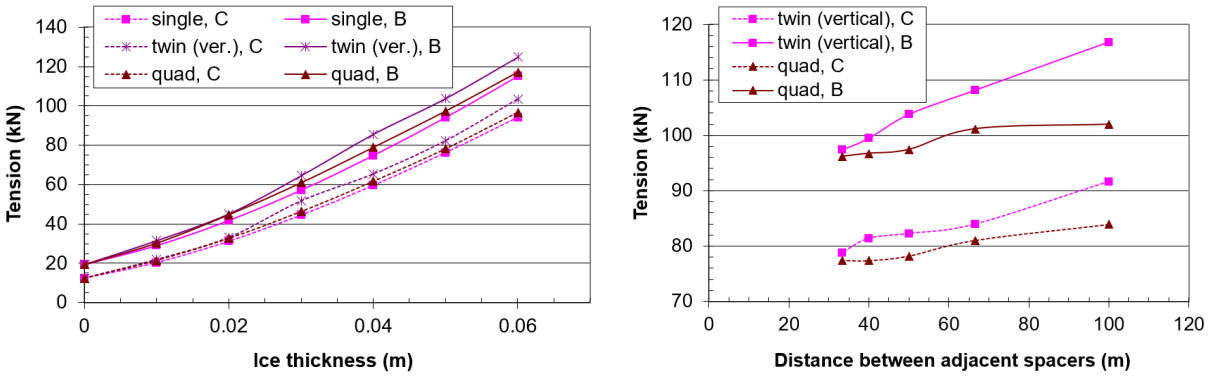

(a) (b)

Figure 3.4: Maximum conductor tension, C – Condor conductor, B – Bersfort conductor, (a) distance between adjacent spacers: 50 m, (b) ice thickness: 50 mm

conductors will contact if ice thickness is at least 30 mm even if the spacer distance is only 33 m. Furthermore, if this distance is increased to 100 m, impact will occur even for the lowest ice loads considered. It was also observed that the minimum subconductor distance was, in general, greater for the Bersfort conductor, i.e. the threat of contact between conductors was less severe.

The above discussion refers to the case when ice sheds completely from one conductor while the other one remains fully loaded. It should be noted, however, that the model may easily be adapted to simulate ice shedding from more than one subconductor, or to simulate partial shedding, by changing the material properties of some conductor elements in the dynamic analysis.

Maximum conductor tension

The calculation of conductor tension is also important, since high transient dynamic forces may damage the conductor or other elements of the transmission line. The maximum tension during vibration occurs near a suspension or a spacer. Figure 3.4a and 3.4b show the increase in conductor tension as a function of shedding-ice thickness and spacer distance, respectively. Conductor tension is lowest for a single conductor because there are no constraints from other conductors. It is highest for a twin bundle, and it decreases with the number of subconductors in the bundle. The conductor tension of the Bersfort conductor is greater than that of the Condor conductor due to the former's greater weight (see Table 3.2). The critical load at which the suspension structure fails was estimated at 100 kN in [81], although this value depends on the particular suspension structure. For the Condor conductor, this value is exceeded only after the shedding of a 60-mm ice chunk from a twin-bundled subconductor. For the Bersfort conductor, however, it is exceeded for all configurations after the shedding of a 60-mm ice chunk, and it is also exceeded in some cases after the shedding of a 50-mm ice chunk.

The simulation results presented in this section revealed the effects of ice thickness, distance between adjacent spacer and number of subconductors on the vibration following ice shedding from one subconductor in a bundle. The displacements and conductor

tension during vibration increase with ice thickness. The maximum jump height and the conductor tension increase with distance between adjacent spacers as well. However, the maximum drop also depends on whether there is a spacer in the middle of the span, when the maximum drop is smaller. Increasing the number of subconductors reduces the severity of vibration. The maximum jump height of a single conductor is significantly greater than that of a conductor bundle; the conductor tension, however, is slightly lower for a single conductor during vibration, since no constraint is transmitted from other conductors in this case. Kollár and Farzaneh [67] approximated the maximum jump height and the maximum drop as power functions of ice thikcness and distance between adjacent spacers. Although these power functions depend on further parameters, they were found to be useful tools to express qualitative relationships between the parameters examined. Recommendations for future research included the investigation of the effect of ice shedding on the torsion of the bundle and the validation of simulation results by comparing them to experimental observations. This study was carried out and published in [71], which is the subject of the subsequent section.

3.3 Numerical and experimental modelling of sudden ice shedding

The numerical model presented in the previous section is improved so that it (i) predicts transverse cable motion and, consequently, bundle rotation; (ii) simulates shedding of concentrated loads as it occurs in experimental modelling of ice shedding; and (iii) considers cable damping by a different approach providing more realistic results. The experimental simulation is implemented by load shedding tests on a small-scale laboratory model based on ideas proposed in [49, 89], and extending them to bundled conductors. Numerical model predictions are validated by comparing them to observations obtained during these experiments as well as during former full-scale tests. Finally, the model is applied to simulate sudden ice shedding from a subconductor in a full-scale twin bundle [71].

3.3.1 Experimental set-up

The experimental setup was constructed for modelling one span of a twin bundle with spacers in the horizontal plane. The distance between the cables was 5 cm. Two identical Vanguard 7x19 construction stainless-steel cables were connected at each end to aluminum plates hinged to the suspensions. Cables with two different diameters were used in different tests; their parameters are provided in Table 3.3. The span length was limited to 6.4 m, because of the laboratory chamber size. In the setup, simple bars acted as spacers, satisfactorily modelling the spacers' role of maintaining a constant distance between the subconductors. However, the bars could not simulate the damping effects of the spacers. Experiments were carried out with up to five spacers. Although subspan lengths are usually unequal in practice, equal subspan lengths were applied to these tests for the

Parameter	Unit	Vanguard 1/8"	Vanguard 3/16"
Cable diameter	(mm)	3.2	4.8
Cross-sectional area of the cable (sum of strand cross-sections)	(mm^2)	5.50	12.33
Mass per unit length of the cable	(kg/m)	0.043	0.097
Sag of unloaded cable	(m)	0.290	0.309

Table 3.3: Parameters of Vanguard 7x19 construction stainless-steel cables

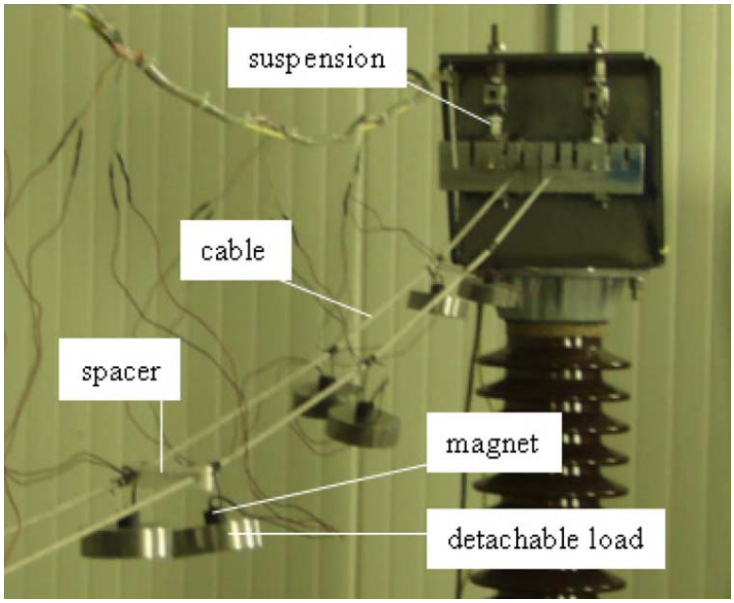

Figure 3.5: Part of the experimental setup showing the main elements

sake of simplicity. The stress-strain curves of the cables were determined in tensile tests carried out according to the ASTM SA-370 Standard [7]. The stress-strain curves were approximated by piecewise linear relationships that served as input when defining cable material properties in the numerical model.

The ice load was modelled by weights attached to the cables via electromagnets. Eight weights of 0.812 kg each were attached to both cables with approximately constant distances in between, representing a load of 8 times 0.812 kg in 6.4 m (i.e. 1.015 kg/m). The current in the electromagnets was switched on before the weights were attached, meaning that switching off the current released the weights, thereby simulating ice shedding from the corresponding area of the cable. When simulating sudden shedding from the whole span, the eight weights on either cable were released at the same time. The main elements of the experimental setup are shown in Figure 3.5.

The time history of vertical displacement of cables following load shedding was observed at midspan by fixing a scale closely behind the cables and recording cable movement by a digital video camcorder. The angle of bundle rotation was also determined at midspan by using the horizontal and vertical coordinates of the spacer attachment points. In order to achieve this goal, a scale was placed horizontally above the cables, another scale was fixed vertically near the cables, and the vibration was recorded by the same camera.

Coordinates of the spacer attachment points were given by the pixel numbers in the video recording, and the scales were used to calibrate the pixel size. The highest jump was occurring at midspan when there was no spacer there, so that a vertical vibration was observed in the configurations without spacers (i.e. single cable), and with two and four spacers. However, since the bundle rotation was measured at midspan by using the spacer attachment points, bundle rotation was observed when applying one, three, or five spacers, one of them located at midspan.

The model scale factor can be determined from the ratio of the dynamic elasticity of a real conductor to that of the model conductor [57]. According to this definition, the scale factor of the present model is quite small (around 7), which means that the span length of the corresponding full-scale line (approximately 45 m) is significantly shorter than those used in practice. Therefore, the numerical model presented in Section 3.3.2 will also be applied to full-scale lines with longer span length in order to observe tendencies as to how conductor jump height and bundle rotation vary with the number of spacers in the span or, in other words, with subspan length.

3.3.2 Numerical model

The model for a single span of bundled conductors is based on the finite element model that was presented in Section 3.2.2. The present section details further developments including models of conductor damping, suspension, and spacer. In the experiments, as in those of [89], ice shedding is modelled by load shedding. Some details of the numerical model simulating this process are discussed at the end of this section.

Conductor

The conductor model described in Section 3.2.2 has been improved as follows. The material properties of the conductor are accounted for by a nonlinear elastic material model, not allowing compression and defining a piecewise linear stress-strain curve. This stress-strain relationship is based on tensile tests when modelling the experimental setup, and on the data provided in literature when modelling full-scale transmission lines.

Conductor damping is modelled by Rayleigh damping following the proposition of [105]. In this case, the Rayleigh damping parameters were obtained from the natural circular frequencies and damping ratios in two different vibration modes [9]. The natural circular frequencies were determined from the linear theory of free vibration of suspended cables [48]. The damping ratios were calculated from the logarithmic decrement which was obtained following the observation of the decay of vertical cable vibration. The damping ratio of Vanguard cables used in the laboratory experiments was obtained as 0.02.

Suspension

The subconductors in the experimental setup are connected to an aluminum element which is hinged to the suspension. This aluminum element is modelled by one truss element at each cable attachment with a simplification of its geometry obtained by defining a

uniform area of cross section. This element is associated with elastic isotropic material representing aluminum. Rotation around the transverse axis is allowed at the points where the cable is attached to the aluminum element, and where the latter is hinged to the suspension.

Spacer

A spacer model was described in [67], which was later improved in [68] where the spacer damper properties were determined more precisely in material tests. When modelling the small-scale experiments in [71] and the torsional tests of [93], a simplification is applied, since rigid spacers were used in most of these experiments. This simplified model is summarized briefly as follows.

Spacers for a twin bundle are considered as simple rods clamped to a conductor at each end [67]. They are modelled by two-node truss elements in the load shedding tests and by beam elements in the torsional tests, and are associated with an isotropic linear elastic material. In the dynamic load-shedding tests, the structural damping of spacers is considered by a nonlinear spring element with exponent 1 and with a damping constant calculated from

$$C_s = 2\zeta_s \sqrt{E_s A_s \mu_s} \tag{3.5}$$

where ζ_s is the spacer damping ratio (which was set at 0.005 when simulating the small-scale experiments), E_s is the Young's modulus, and A_s and μ_s are the cross section and mass per-unit length of the spacer element, respectively.

Ice load and ice shedding

Ice usually appears on transmission-line conductors as a distributed load. Since distributed loads cannot be applied on truss elements, Roshan Fekr and McClure [106] proposed a model as explained in Section 3.2.2.

The present model considers ice load and shedding in a different manner that better approximates the load-shedding tests presented in Section 3.3.1 and those reported in [89]. This model considers the load resulting from several point loads along the conductor. If these concentrated loads are attached to many points of the conductor, they provide a satisfactory approximation of the distributed ice load. Thus, in the static analysis, concentrated loads are applied along the span at constant distances similar to the experiments. Then, these loads are removed at the beginning of the dynamic analysis, simulating sudden shedding. This model is applied to simulate uniformly distributed ice along the conductor with the same initial ice mass on each subconductor. However, it can easily be adapted to simulate nonuniform ice accumulation and different ice masses on the subconductors by varying the concentrated loads.

3.3.3 Validation of the numerical model

The numerical model is first validated by comparisons to full-scale observations. Due to the lack of data on sudden ice shedding tests or field observations on full-scale conductor

Parameter	Unit	Copper-eq. steel-cored Al	795 MCM ACSR (26x7)	Bersfort ACSR
Conductor diameter	(mm)	19.6	28.2	35.6
Cross-sectional area of the conductor (sum of strand cross-sections)	(mm^2)	227.6	460	747.1
Mass per unit length of the conductor	(kg/m)	0.85	1.628	2.37
Sag of unloaded conductor	(m)	5.18	3.34	6.0

Table 3.4: Parameters of copper-equivalent steel-cored aluminum, 795 MCM ACSR 26x7 and Bersfort ACSR conductors

bundles, the numerical model was applied to simulate ice-shedding tests on a full-scale line of single conductors [89] as well as static torsional tests on a full-scale span of a twin bundle [93]. Then, the model is also validated by simulating load-shedding tests on the small-scale experimental twin bundle presented in Section 3.3.1.

Sudden load shedding on a full-scale line of single conductors

The numerical model is applied to simulate vertical conductor vibration following the sudden release of loads on a full-scale five-span section of single conductors. The measured and computed sags of the loaded span in static equilibrium and the conductor jump heights are compared. The results of the original load-shedding tests were reported in [89]. The five-span section is located on an inclined surface where the altitude differences between the suspension points of each span beginning from the leftmost span are 5, 16, 28, 16, and 8 m. The corresponding span lengths are 283, 387, 247, 213, and 309 m, respectively. Four of the shedding scenarios in [89] were repeated numerically for the present comparison: suspension with standard suspension string and full shedding from the middle span with loads of 1.49, 2.98, 4.47, and 5.96 kg/m (1, 2, 3 and 4 lb/ft). The loads were attached at every second nodes in the numerical model, and they were calculated so that the total load was the same as in the experiments. The conductors were made of copper-equivalent steel-cored aluminum whose data are provided in Table 3.4. Its stress-strain curve was considered linear for positive strains with Young's modulus of 91.8 GPa, and no compression was allowed. Dead ends were assumed at the extreme suspensions, whereas at the other suspensions, the only free degree of freedom was the rotation around the horizontal axis perpendicular to the plane determined by the suspension and the connecting conductors. One time history of vertical conductor oscillation was shown in [89], which was used to approximate the logarithmic decrement and to estimate the damping ratio of the conductor as $\zeta = 0.03$.

The sags of the loaded span in the static equilibrium and the conductor jumps above the loaded position after shedding are shown in Figure 3.6a and 3.6b, respectively. These figures support the reliability of the model for dynamic analysis of full-scale transmission

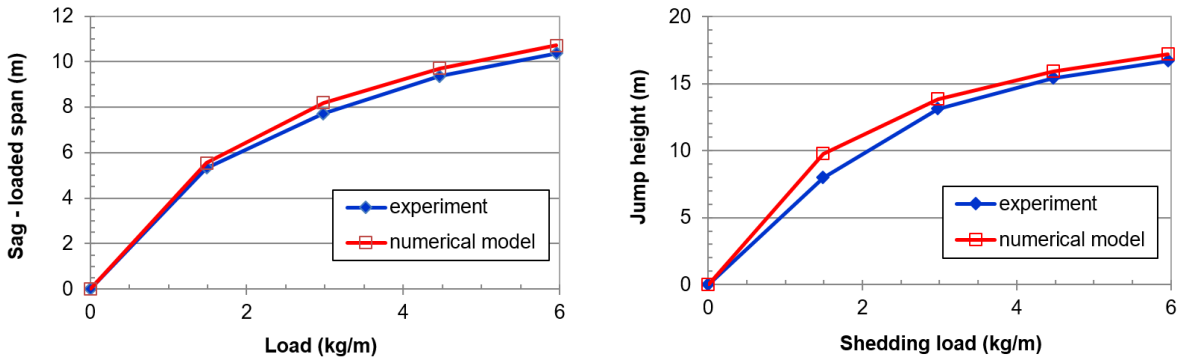

(a) (b)

Figure 3.6: Simulation of load-shedding tests on a full-scale five-span section with single conductors; experimental results were reported in [89]; (a) static sag of the loaded span; (b) conductor jump height above the loaded position

lines. The only considerable overestimation of the model, by 22%, appears for the jump height after the shedding of the 1.49 kg/m load. In all other cases, the overestimation was in the range of 3%–6%. The period of vibration was reported at 4.12–4.16 s in [89], whereas it occurred at 4.2 s for the 1.49-kg/m load and then reduced to 3.6 s for higher loads according to numerical calculations. Since the original experiments were carried out with single conductors, these comparisons cannot validate how the model predicts bundle rotation in a full-scale line during vibration.

Torsional tests on a full-scale span with a twin bundle

In order to evaluate the model concerning bundle rotation in full-scale transmission lines, some of the static torsional tests of [93] were also simulated numerically. They applied a torque on twin and quad bundles until the bundle collapsed. They varied the span length, the subconductor spacing, the number, location, and type of spacers and the conductor tension. Two of these tests were repeated numerically where the complete moment-rotation curves were presented. These tests were conducted on a horizontal arrangement of a twin bundle with one spacer at midspan, and with three spacers at 1/4, 1/2, and 3/4 of the span. The span length was 244 m, and the subconductor spacing was 0.457 m. The conductor type was 795 MCM ACSR (26x7) whose data are provided in Table 3.4. The stress-strain curve of conductors in the model was considered linear for positive strains with a Young's modulus value of 75.1 GPa, and no compression was allowed. The moment was applied at midspan. Rotation around the axis perpendicular to the vertical plane of the conductor in static equilibrium was allowed at the suspension, and further degrees of freedom were fixed.

The moment-bundle rotation relationships are shown in Figure 3.7. When one spacer is applied (Figure 3.7a), the model overestimates the measured moments and, consequently, the collapse moment by about 20%. The theory presented in [93] underestimates the measured moments to a similar extent, up to 45°, then the two curves approach each other, and the collapse moment and collapse angle are overestimated. The numerical

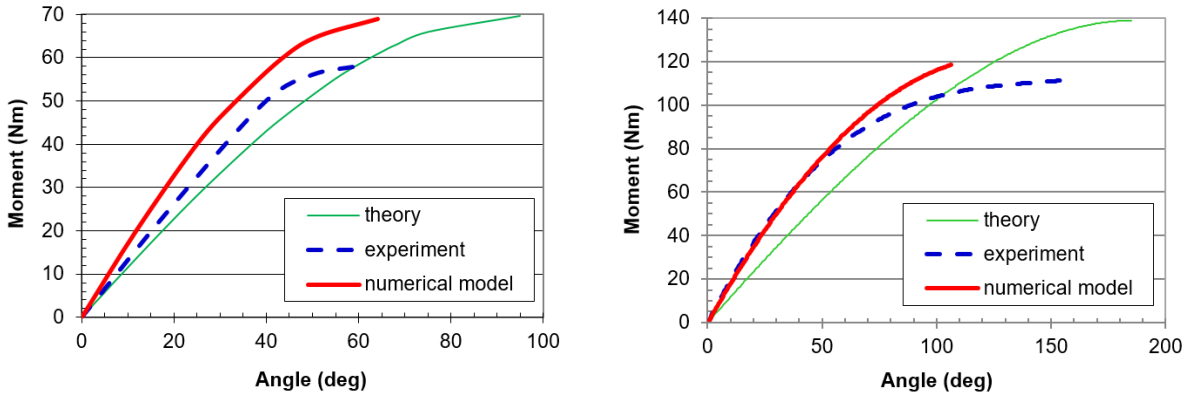

(a) (b)

Figure 3.7: Simulation of static torsional tests on twin bundles; experimental results were reported and theory was proposed in [93]; (a) one spacer at mid-span; (b) three spacers at 1/4, 1/2, and 3/4 span

model provides a significantly closer estimation of the collapse angle than this theory. The discrepancy between the experimentally and numerically obtained curves for three spacers (Figure 3.7b) is different from that for one spacer (Figure 3.7a), which may be due to the different methods as how the moment was applied in the experiments or due to the different spacer types used in the experiments. The estimation of the numerical model is excellent, the two curves coincide up to 50°. Then, the numerical model overestimates the measured moment for angles greater than 50° including the collapse moment, and it underestimates the collapse angle. The theory underestimates the measured moments up to about 100°, and then it overestimates the collapse moment and collapse angle. It may be concluded from Figure 3.7 that the numerical model is reliable when the angle of bundle rotation is a sharp angle, but improvement is needed in the range of obtuse angles to consider a faster increase of angle with the applied moment.

Small-Scale Experiments

The numerical model was also validated by simulating load-shedding tests on the small-scale experimental twin bundle presented in Section 3.3.1, and comparing: (i) the calculated and measured static sags of the loaded cable; (ii) the vertical components of cable vibration after the load shed from one of the cables; and (iii) the angles of bundle rotation. Experiments were carried out with the two Vanguard cables whose properties are listed in Table 3.3. The static sag of the cables with diameters of 3.2 and 4.8 mm is increased by 3.7 and 1.5 cm, respectively, after attaching the loads. The same increments in the sag are 3.3 and 1.5 cm according to the numerical model. Results of the dynamic analysis implemented by the model are compared to experimental observations in Tables 3.5-3.7. These results were obtained for the cable of 3.2-mm diameter when loads shed suddenly from one cable while the other cable remains loaded. Each shedding scenario was repeated twice with an alternation of load-shedding cable, so that two numbers appear in the column “small-scale experiments”. The cases when a spacer is attached at midspan (odd

Number of spacers	Small-scale experiment (cm)	Small-scale model (cm)	Full-scale model (m)
0 (single cable)	18.9 / 21.4	16.1	4.085
2	13.3 / 14.4	11.6	2.88
4	9.0 / 9.7	8.2	2.09
1	4.8 / 5.2	4.8	1.23
3	5.5 / 5.5	5.0	1.76
5	5.4 / 5.5	5.0	1.70

Table 3.5: Jump height of shedding cable at mid-span above loaded position during vibration following shedding from either cable when the other one is loaded

Number of spacers	Small-scale experiment (%)	Small-scale model (%)	Full-scale model (%)
2	67 - 70	72	71
4	45 - 48	51	51
1, 3, 5	24 - 29	30 - 31	30 - 43

Table 3.6: Ratio of jump height of shedding cable in twin bundle and that of shedding single cable during vibration following shedding from either cable when the other one is loaded

number of spacers along the span), and when there is no spacer at midspan (even number of spacers) must be discussed separately. The reason for this is that the jump height is significantly lower in the proximity of a spacer; and the highest jump usually appears in the middle of the subspan which is closest to midspan. This position falls midspan for an even number of spacers. However, the jump at midspan is considerably reduced for an odd number of spacers. Furthermore, bundle rotation was observed only for odd number of spacers at midspan by recording the movement of spacer attachment points.

Tables 3.5-3.6 compare experimental and numerical results, namely, the cable jump at the midspan above the loaded position during the vibration following shedding from either cable when the other one is loaded. It may be observed clearly that the jump height decreases by adding an even number of spacers, and that this jump height, when there is a spacer at midspan, is nearly independent from the number of spacers along the span. The magnitude of jump height is underestimated by 5% to 20% by the numerical model (see Table 3.5), but the tendencies according to the number of spacers are approximated closely. Although the ratio of jump height of the shedding cable in the twin bundle to that of a shedding single cable is overestimated by up to 20%, the discrepancy is below 10% in most cases (see Table 3.6). It should be noted that these ratios depend on such other parameters as the shedding load weight, which were kept constant in the experiments.

Table 3.7 shows the maximum angle during bundle rotation, which appears to be around 70° for one spacer. However, it may approach or even exceed 90° for three and five spacers. Thus, increasing the number of spacers will not reduce bundle rotation; contrarily, further connections between the cables in the bundle may help the shedding

Number of spacers	Small-scale experiment (deg)	Small-scale model (deg)	Full-scale model (deg)
1	62 / 69	72	91
3	88 / 110	86	102
5	88 / 106	77	104

Table 3.7: Maximum angle of bundle rotation during vibration following shedding from either cable when the other one is loaded

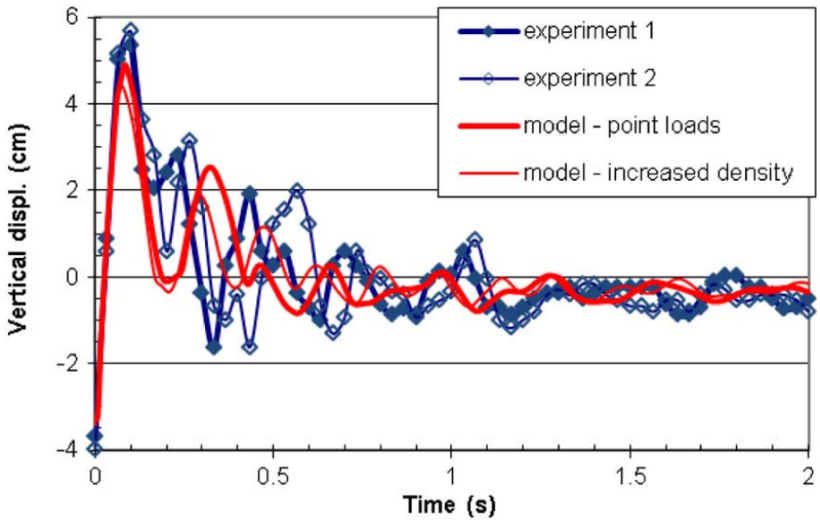

Figure 3.8: Vertical vibration of shedding cable when the other one is loaded with four spacers; experiment 1 and experiment 2: experimental results with shedding from cable 1 and cable 2, respectively, model — point loads: ice load considered by point loads, model — increased density: ice load considered by increased cable density

cable to move above the other one everywhere along the span. The probable explanation of this result lies in the fact that the relative motion of the two cables is nonuniform along the span. The greatest transverse and vertical displacements of the shedding cable appear close to the middle of the subspan, which is far from the spacer where the angle is measured. However, when the number of spacers is increased, this relative motion becomes more uniform and the several connection points (spacers) between the two cables contribute to increasing the angle of rotation at midspan. Since the maximum angle of bundle rotation for one spacer was a sharp angle in the experiments, the model provided a close prediction, but it underestimated the bundle rotation by 10%–20% for three and five spacers when the bundle rotation approached or exceeded a right angle.

In Figure 3.8, typical time histories of vertical displacement are compared with the results of the numerical model for the cases of even numbers of spacers when one cable is shedding, and the other one is loaded. Also, an ice-load model by increasing the cable density proportionally with the ice-load weight as proposed by [106] was applied to these cases. It was used to verify whether the shedding of distributed loads can be simulated by the shedding of eight point loads attached symmetrically along the span. The resulting vibration is slightly more severe with the point-loads model. However, the difference is

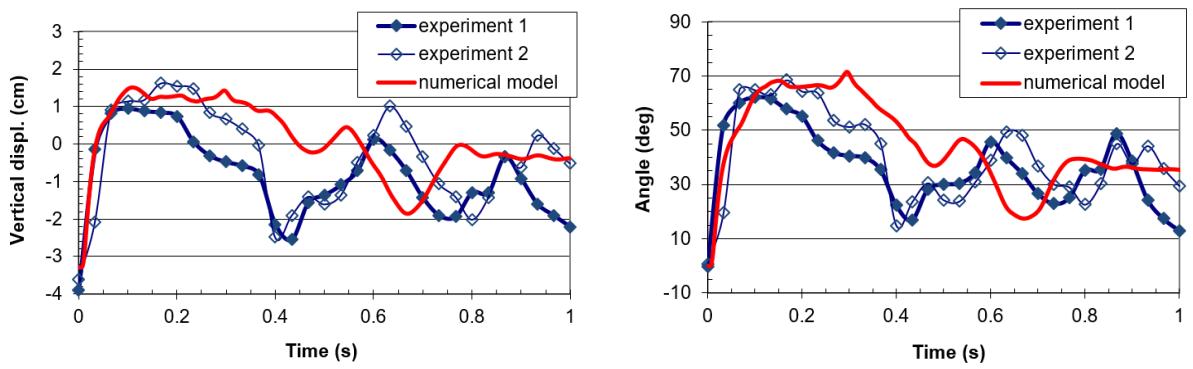

(a) (b)

Figure 3.9: Vertical displacement of shedding cable and angle of rotation of bundle with one spacer at midspan following shedding from either cable when the other one is loaded; (a) vertical displacement; (b) rotation angle

not significant, for example, the discrepancy between the jump heights is less than 5%. Considering that a similar discrepancy also appears even between the two experimental results obtained under the same conditions, the approximation of distributed loads by point loads is satisfactory. Model predictions underestimate the jump height obtained experimentally by 10%–20%, which is in accordance with the results listed in Table 3.5. The reason for this difference probably lies in the simplification of suspension modelling. Another reason may be an overestimated value for cable damping, although it is less probable, because the decay of vibration is closely predicted by the model.

Figure 3.9 presents typical time histories of the vertical displacement and rotation of bundle in the case of an odd number of spacers during the vibration following shedding from one cable while the other one is loaded. Figure 3.9 compares the results of experimental measurements to those of numerical simulations. The model approximates closely the jump height of the shedding cable and the maximum angle of bundle rotation. The discrepancy between the computed and measured values is 15% or less. The model underestimates the extent of drop after the first peak, so that the peaks following this drop are predicted about 0.1 s earlier as observed in the experiments. Further numerical simulations and experiments with the 4.8-mm-diameter cable revealed the extent to which the increase in cable diameter reduces the jump height and maximum angle of bundle rotation. It should be clear, however, that the application of cables with greater diameters increases the load due to deadweight with the third power of cable diameter.

3.3.4 Application for a full-scale span with a twin bundle

The numerical model was used to simulate sudden ice shedding from the full-scale span of Bersfort conductors presented in [67], so that in addition to vertical cable vibration, bundle rotation was also simulated. The model considers one span with a length of 200 m, including Bersfort conductors whose geometrical data are provided in Table 3.4. Its stress-strain curve is considered linear for positive strains with Young's modulus of 67.6 GPa, and no compression is allowed. Dead ends are assumed at the suspensions where

the only free degree of freedom is the rotation around the axis perpendicular to the plane of the structure. Each cable was simulated by 100 elements, and concentrated loads were applied at every fourth points. It was verified that increasing the number of loads along the span caused negligible differences in the results. The applied load corresponded to a load due to 50-mm-thick glaze ice whose density was 900 kg/m^3. The damping ratio of the spacer was set at $\zeta_s = 0.2$ in correspondence with [39].

Tendencies similar to those obtained for the small-scale model were observed concerning the effects of the number of spacers on jump height and on the maximum angle of bundle rotation following ice shedding. The reduction in the ratio of jump height of the shedding cable in the twin bundle to the jump height of a shedding single cable due to additional spacers was similar to that observed in the small-scale tests (see Tables 3.5 and 3.6). It should be kept in mind, however, that when the ice load is lower, the reduction in the jump height due to additional spacers is less considerable. Table 3.7 shows that after the shedding of high ice load (thickness of 50 mm), the maximum angle of rotation exceeded 90°, which significantly increases the risk of bundle collapse. The maximum angle of bundle rotation was greater for three and five spacers than for one spacer, which also corresponds to the tendency observed in the small-scale experiments.

This section summarized the numerical and experimental simulation of cable vibration and bundle rotation following sudden ice shedding from either subconductor of a twin bundle. The numerical model was validated by full-scale and small-scale experiments, and was applied to a full-scale span with a twin bundle. The full-scale tests involved (i) load shedding from a single conductor where the conductor jump was studied and (ii) static torsional tests on twin bundles where the bundle rotation was observed. The small-scale tests simulated different load-shedding scenarios with up to five spacers along the span. The vertical component of cable vibration and the bundle rotation at midspan were recorded and calculated. Similar scenarios were simulated, and the same parameters were determined when the model was applied to a full-scale twin bundle. The following conclusions are drawn from the results.

- The tendency of reduction in the cable jump height above the loaded position due to an increasing number of spacers along the span was predicted within 10% by the model, approaching 20% in some cases. The same discrepancies were observed between the numerically and experimentally obtained values for jump height.

- The maximum angle of bundle rotation was estimated satisfactorily for sharp angles. However, improvement to the model is needed by considering the configuration of the vibrating span more precisely for severe vibrations when the bundle rotation exceeds a right angle.

- Increasing the number of spacers by up to four reduces the cable jump height significantly compared to the jump height of the single cable. The application of a spacer at midspan may lead to a further decrease in the cable jump, although in this case, a greater jump may appear elsewhere. However, the bundle rotation cannot be reduced by increasing the number of spacers.

The presented scenarios considered extreme cases when one subconductor sheds suddenly and fully, these results being useful to predict extreme dynamic effects. However, further tests and the corresponding modification of the numerical model were recommended for future research in order to simulate more representative ice shedding propagation, which is the subject of Section 3.4.

3.4 Modelling ice shedding propagation on transmission lines with or without interphase spacers

The numerical model of the preceding sections is further improved to simulate ice shedding propagation on a single conductor and on several spans of conductors linked with interphase spacers. In order to validate the model simulation results are compared to experimental observations on a full-scale test line [122]. The model is applied to predict vertical and transverse conductor displacements and conductor tension variation during the vibration initiated by ice shedding propagation. A further goal involves the comparison of the dynamic effects of the following three shedding processes: (i) propagation of ice shedding along the length of the span, (ii) propagation of ice shedding along the length of the span plus an additional downward pull induced at discrete locations along the span by the detachment of ice chunks, and (iii) sudden and simultaneous ice shedding from the whole span or part of the span [76].

3.4.1 Numerical model

The models of the conductor and the suspension are described in Sections 3.2.2 and 3.3.2. Interphase spacers are considered as simple rods clamped to a conductor at each end. They are modelled with beam elements, and are associated with an isotropic linear elastic material. Approaches for the consideration of ice load in the model are also presented in Sections 3.2.2 and 3.3.2, and the models of different ice shedding processes developed in [76] are detailed in what follows.

Ice load is modelled by attaching concentrated loads at several discrete points along the span. Ice shedding propagation is then simulated through the removal in a defined sequence of the concentrated loads. The propagation velocity is controlled by associating each concentrated load with a time function which determines the removal time of that specific load. In the calculation, the load is multiplied in each time instant by the value the time function takes in that time instant. The three ice shedding processes mentioned in the introduction of Section 3.4 may be modelled by using two different time functions which were proposed in [75]. In both time functions, the time, t_i, denotes the beginning of load removal, Δt_r stands for time interval of load removal, and Δt_s is the time step in the numerical simulation. It is assumed that a load is removed suddenly, i.e. $\Delta t_r < \Delta t_s$.

When ice shedding propagates along the span with its associated load removal, the time function shown in Figure 3.10a is applied for each load at different time instances. If n loads act along the span and T_w denotes the wave propagation time along the span,

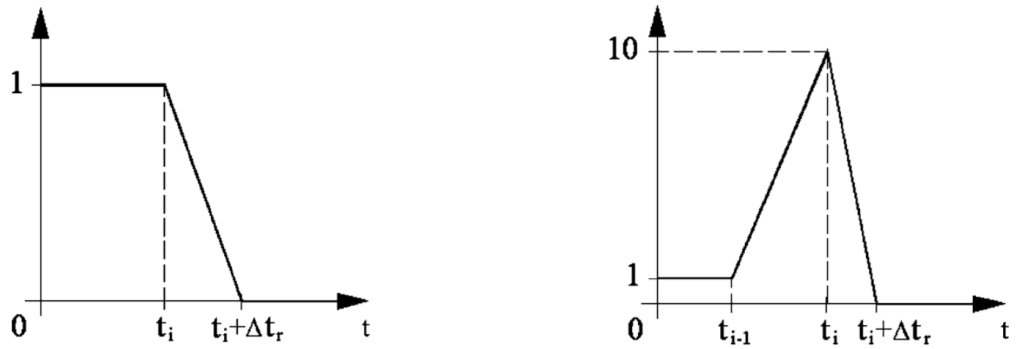

(a) (b)

Figure 3.10: Time functions for load removal

then the time instance when the defined time function is applied for the ith load may be determined as follows:

$$t_i = \frac{i}{n+1} T_w \qquad i = 1, \ldots, n \tag{3.6}$$

When ice detachment propagates along the span, but the ice falls in big chunks, then the detached ice does not break off the ice which is still attached to the remaining part of the conductor and applies an excess load on the conductor where the ice is still attached. Thus, a time function which considers a significant increase in the load locally before load removal should be applied as shown in Figure 3.10b. The time instance, t_i, when the time function is applied for the ith load is obtained from Equation (3.6).

When ice is detached and falls suddenly in big chunks, then the time function presented in Figure 3.10a is applied; however, the time instance of application, t_i, is the beginning of the dynamic analysis for each load (which means mathematically that $T_w = 0$). The subsequent sections discuss the dynamic effects of the three shedding processes presented, but the numerical method may easily be adjusted to simulate further shedding processes: e.g. non-uniform ice load along the span may be modelled by varying the magnitudes of the n loads; partial ice shedding may be simulated by applying time function only for some of the loads; and a non-constant propagating velocity can also be considered by modifying Equation (3.6), i.e. the time instance of application of time function.

The procedure of computation is summarized as follows. The initial profile, i.e. the profile of the unloaded span, is determined using the catenary equation [47]. The initial configuration is then constructed in ADINA [3], and the point loads simulating the accumulated ice are added in the static analysis that provided the loaded profile of the modelled configuration. The time function describing the shedding propagation is applied in a separate, dynamic analysis that simulates the load removal and the resulting conductor vibration in the following few seconds.

3.4.2 Simulation of ice shedding propagation on a full-scale line

Ice shedding propagation is simulated on the Hydro-Quebec test line. Its numerical model is constructed in this section, then simulation results are presented.

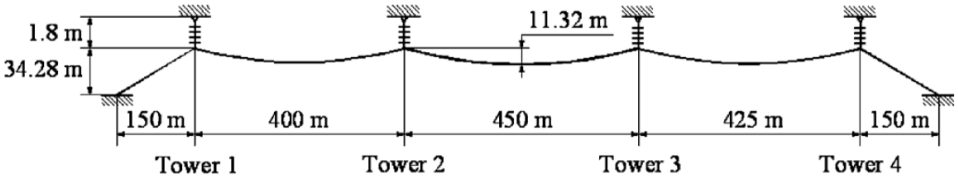

(a)

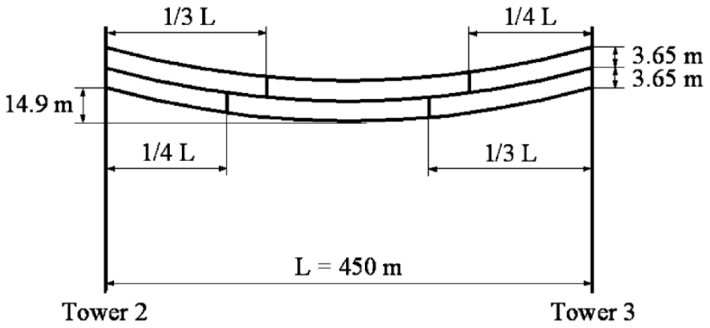

(b)

Figure 3.11: Sketch of numerical models of test lines (not to scale), (a) configuration with single conductors, (b) middle span in configuration with three conductors (the middle conductor is not in the same vertical plane as the other two conductors)

Construction of numerical model

The Hydro-Quebec test line consists of three suspension spans and two dead-end spans. Ice shedding propagation on the middle span from a single conductor and from a conductor in a vertical arrangement of three conductors was simulated in [122]. Two of these tests (called Test A and Test C in [122]) are modelled numerically in [76]. Figures 3.11a and 3.11b sketch the numerical model of the unloaded test line with single conductors (Test A), and that of the middle span with the vertical arrangement of three conductors (Test C), respectively. In the latter case, the top and bottom conductors are in the same vertical plane, but there is a transverse distance of 0.98 m between the vertical plane of the middle conductor and that of the other two conductors. The ice shedding tests were performed on Condor ACSR 54/7 conductors suspended with glass I-insulator strings. The conductor damping was found due mainly to aerodynamic resistance. The Rayleigh damping coefficients were calculated using the damping ratio that was determined in [120]. In the tests with three conductors per span, the conductors in each span were linked with four interphase spacers as shown in Figure 3.11b. Details of these interphase spacers are provided in [120], but the numerical model simplifies them to have constant cross section and material properties defined for aluminum.

Ice weight was modelled in the experiments of [122] by a conductor which was held initially by pulleys at each end of the span, and which was connected to the test conductor by strings at every 15 m along the span. Shedding was initiated by releasing the pulley at the end of the span near Tower 2, and then the strings broke one after the other simulating the propagation of load shedding toward Tower 3. Correspondingly, concentrated loads were considered at every 15 m in the numerical model, thereby applying $n = 29$ loads

Test	Unit	A	C
Initial sag	m	11.32	14.90
Additional sag - experiment	m	2.77	2.32
Additional sag - numerical	m	2.75	2.52
Initial tension	kN	33.4	25.4
Tension in loaded conductor - experiment	kN	36.6	42.6
Tension in loaded conductor - numerical	kN	37.7	41.9

Table 3.8: Sag and tension of unloaded and loaded conductor

along the 450-m-long middle span. Since the shedding process in the experiments was closest to the propagation of ice detachment followed by falling of a big chunk, the time function shown in Figure 3.10b was applied in the numerical model. In Test A, a load of 0.6 kg/m was applied on the conductor in the middle span, and it took 3 s to break all the strings holding the dead-weight conductor (i.e. $T_{w,A} = 3$ s). This load corresponds to the weight of 6-mm-thick cylindrical ice accretion on Condor conductor if glaze ice with density of 900 kg/m^3 is assumed. In Test C, the three conductors in the middle span were loaded initially. The load on the top and mid conductor was 2.37 kg/m (corresponding to ice thickness of 18 mm), whereas the load on the bottom conductor was 1.5 kg/m (corresponding to ice thickness of 13 mm). Since the top and mid conductors remained loaded during the test, they were loaded in the experiments by attaching D-shapes to them with additional masses. Consequently, the cross section of these two conductors was increased in the numerical model in order to consider the load on them. The bottom conductor was unloaded during the test, and the whole span was unloaded in 16 s (i.e. $T_{w,C} = 16$ s).

Simulation results

This section compares results of numerical simulations and experimental observations reported in [120] and in [122] for Tests A and C. The load is applied in the static analysis, when the displacement and tension in the loaded conductor are determined. Then, the dynamic analysis calculates the conductor rebound height together with the time histories of conductor displacement and tension.

The results of static analysis are shown in Table 3.8. For Test A, there is an excellent agreement between the calculated and measured additional displacements at mid-span, which is still below 10% for Test C. It should be noted, however, that there is a more significant asymmetry of the profile in the measurements in Test C. The cable tension in the loaded span was calculated within 2–3% of the measured value for both cases.

Results of dynamic analysis are compared to experimental observations in Figures 3.12, 3.13 and 3.14, and in Table 3.9. The maximum vertical displacements of the conductor above the loaded position at different distances from the suspension are shown in Figure 3.12. The model provides a close approximation of experimental results for Test A. Model predictions for Test C are within 10% compared to the experiments at 75 m from Tower

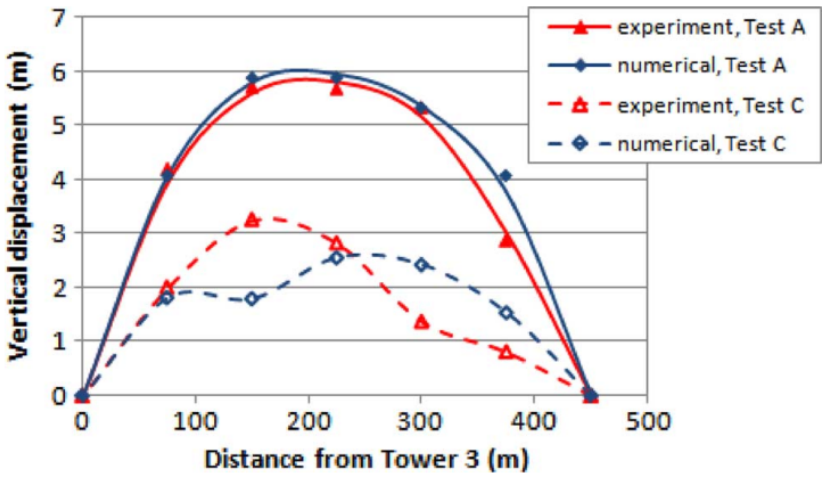

Figure 3.12: Maximum vertical displacements of the conductor above the loaded position at different distances from Tower 3 for Tests A and C

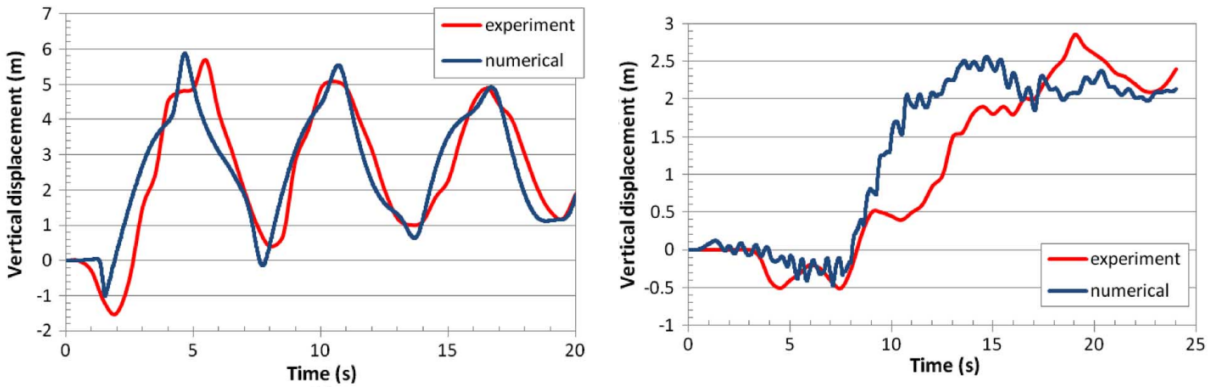

(a) (b)

Figure 3.13: Time histories of conductor vertical displacement at mid-span during the vibration from the beginning of shedding propagation, (a) Test A, (b) Test C

3 and at mid-span (225 m), but a considerable discrepancy occurs at 150 m, 300 m and 375 m. These discrepancies are mainly the consequences of those that were already in the profile after applying the load. The displacements in the numerical static analysis were smaller on the side of Tower 3 and greater on the side of Tower 2 than in the experiments, and the same tendency holds for the conductor jump after shedding. Both of the experimental and numerical results suggest that the maximum conductor rebound above the loaded position is reduced by half (from about 6 m to about 3 m) when using interphase spacers. Since the vertical distance between phases in static equilibrium was 3.65 m (see Figure 3.11b), the risk that conductors touch each other during vibration is reduced significantly by the application of interphase spacers.

Figure 3.13 compares the time histories of conductor displacement when shedding propagates along the span from 0 to 3 s in Test A and from 0 to 16 s in Test C. These time histories show clearly that the conductor drops at the position where the shedding takes place, and then it jumps. In Test A, shedding propagates along the 450-m-long span in 3 s; thus, it arrives to 225 m from Tower 3 after 1.5 s. The conductor at this point

	375 m Exp.	375 m Num.	225 m Exp.	225 m Num.	75 m Exp.	75 m Num.
Peak (m)	3.0	4.1	5.7	5.9	4.2	4.1
Drop (m)	-0.4	-0.4	-1.5	-1.0	-0.9	-1.7
Period (s)	6.2	6.1	5.6	6.0	6.1	6.1

Table 3.9: Maximum conductor rebound after shedding, conductor drop before shedding, and period of vibration in Test A

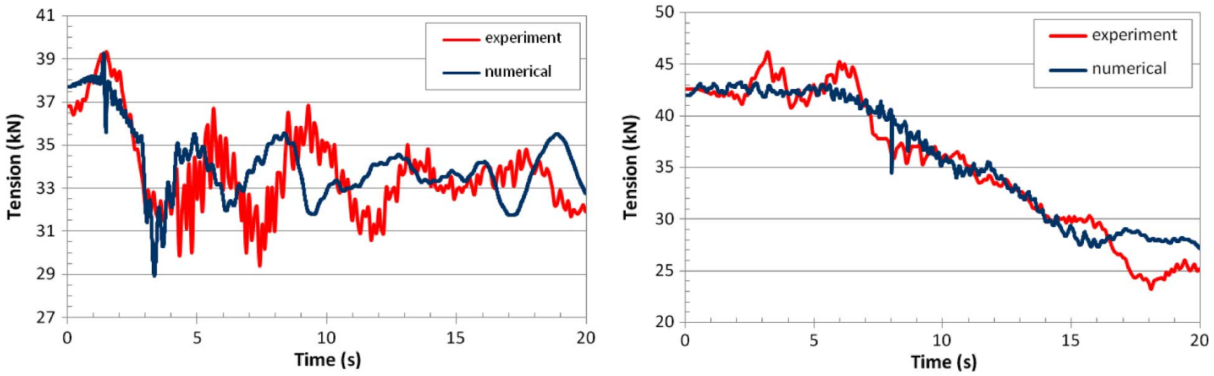

(a) (b)

Figure 3.14: Time histories of conductor tension at mid-span during the vibration from the beginning of shedding propagation, (a) Test A, (b) Test C

reaches its lowest position in this time instance, and then it moves upward quickly. The maximum rebound of the single conductor according to the numerical simulation appears at 190 m from Tower 3, i.e. it is farther from the tower where the shedding propagation begins and closer to the tower which is connected to the longer span. In Test C, the shedding propagation arrives to mid-span after about 8 s, when the conductor reaches its lowest position. The maximum rebound appears at about 250 m from Tower 3, which is close to the half distance between the two interphase spacers located at 150 m and 336 m from Tower 3.

Some data related to the displacement time histories, namely the conductor drop before shedding, the maximum conductor rebound after shedding, and the period of vibration, are listed in Table 3.9 for Test A. The calculated and measured conductor drops at 375 m from Tower 3 coincide, but then the model predicts increasing drop along the span, whereas it was measured greater at mid-span than at 75 m from Tower 3. The model overestimates the first peak at 375 m, whereas the prediction is excellent (2–3% discrepancy compared to measured results) at mid-span and at 75 m. The period of vibration coincides; it is about 6 s in both of the experiments and the numerical simulations. Concerning Test C, the model provides an excellent estimation of the conductor drop at mid-span, it underestimates the peak by about 10%, and this peak appears about 4 s earlier than in the experiments (see Figure 3.13b).

The time histories of conductor tension at mid-span are presented in Figure 3.14. The tension increases approximately at the same time when the conductor drops, and then

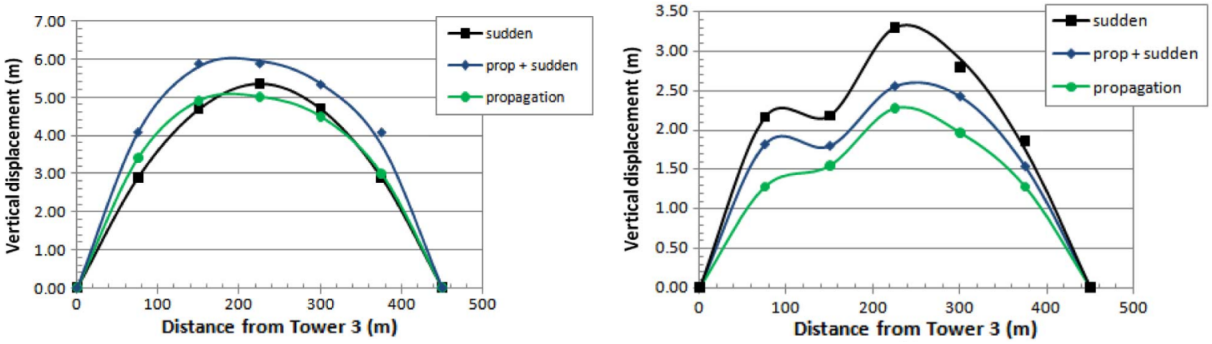

(a) (b)

Figure 3.15: Maximum vertical displacements of the conductor above the loaded position at different distances from Tower 3 for the three shedding processes: sudden shedding (sudden), propagating detachment followed by sudden fall (prop+sudden), and propagating shedding (propagation), (a) single conductor, (b) three conductors with interphase spacers

decreases to the value which was observed without the load. The model provides an excellent prediction for Test A, and the tendency obtained numerically also follows the measured one for Test C, but in this case the model does not predict the increase in the tension before load shedding.

3.4.3 Sudden and propagating shedding on conductors linked with interphase spacers

When ice detachment propagates along the span and ice falls in small pieces, then the conductor rebound also propagates along the span. When the propagation of ice detachment is followed by falling of a big chunk, then the conductor rebound propagates, but a drop precedes the upward movement, and the rebound height is higher due to the increasing load before load removal. When the ice is detached from the conductor suddenly, then the whole conductor jumps immediately. For the sake of simplicity, these processes will be referred to as propagating shedding, propagating detachment followed by sudden fall, and sudden shedding. The numerical model is applied to simulate these three shedding processes on the Hydro-Quebec test line in the same configurations as in Tests A and C. The various shedding processes are modelled by applying different time functions in the dynamic analysis as discussed in Section 3.4.1.

The maximum vertical displacements of the conductor above the loaded position at different distances from the suspension are compared in Figure 3.15. For a single conductor, there is no significant difference in the conductor rebound heights after propagating shedding and sudden shedding, but they are 10–30% greater after propagating detachment followed by sudden fall. This can be explained by the load increase before removal. It can also be observed that the maximum conductor rebound appears at mid-span after sudden shedding, but in the other two cases it is farther from the tower where the shedding propagation begins. For the three-conductor configuration, the conductor

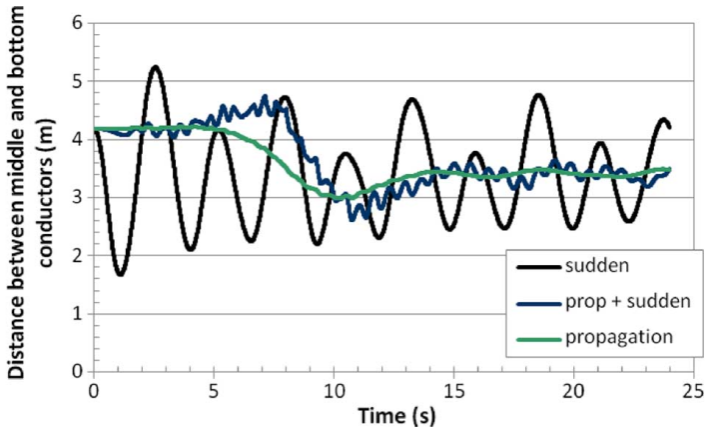

Figure 3.16: Time histories of distance between the middle and bottom conductors at mid-span during the vibrations following the three shedding processes: sudden shedding (sudden), propagating detachment followed by sudden fall (prop+sudden), and propagating shedding (propagation)

rebound heights after propagating detachment followed by sudden fall are about 10–30% greater than after propagating shedding, and they are an additional 10–30% greater after sudden shedding. Thus, the application of interphase spacers reduces conductor movement to a lesser extent after sudden shedding. It should be noted that the reduced jump height obtained at 150 m is due to the interphase spacer located exactly at this position.

The relative motion of conductors in the configuration when conductors are linked with interphase spacers is also important, because it gives information whether the conductors touch each other during the vibration. The time histories of distance between the middle and bottom conductors at mid-span are shown in Figure 3.16. Originally, the vertical and transverse distances were 3.65 m and 0.98 m, respectively. When the load is added, the transverse distance reduces, but the vertical distance increases, so that the total distance at mid-span becomes 4.17 m, which is the initial distance in Figure 3.16. The conductors approach each other to the greatest extent after sudden shedding; however, the minimum distance is still 1.67 m. Thus, the interphase spacers can sufficiently reduce the severity of vibration in the case considered.

A numerical model has been developed to simulate different ice shedding processes on transmission lines with conductors linked with interphase spacers. The model was validated by applying it to experimental ice shedding tests carried out on the Hydro-Quebec test line, and then it was used to compare the dynamic effects of three different shedding processes: (i) propagation of ice shedding along the span, (ii) propagation of ice shedding along the span with an additional downward pull on the conductor at the discrete locations where the ice chunks finally part from the conductor, and (iii) sudden and simultaneous ice shedding from the span or part of the span. The model considered ice load by several concentrated loads applied along the span, whose removal was controlled by a time function which was adjusted according to the modelled phenomenon.

The model estimates the conductor profile and tension after the application of the load, and the time histories of conductor displacement and conductor tension during

the vibration following shedding. Simulation results show, in agreement with former experimental observations, that the application of interphase spacers may reduce conductor rebound height above the loaded position by a factor of two approximately, and thereby they contribute to prevent the reduction of conductor clearance during high-amplitude vibrations. The comparison of different shedding phenomena reveals that sudden shedding has the most severe dynamic effects for conductors linked with interphase spacers; however, the rebound height of a single conductor may be higher in the case of ice shedding with ice chunks pulling on the conductor before parting from the conductor.

3.5 New results

Main contribution 3 *A numerical model was developed to simulate the dynamic effects of ice shedding from conductor bundles. An existing model was improved by proposing a model for the spacers that connect subconductors in the bundle. The material behaviour of the spacer damper is considered by nonlinear elastic material properties. A cubic stress-strain relationship describes the behaviour of spacer arms that are allowed to rotate around the joint with increasing resistance until the rotation is blocked. Further deformation may occur only by the elongation of the material, which is modelled by a linear stress-strain relationship. The application of the model reveals the effects of spacers on conductor vibration and bundle rotation following ice shedding. The specific cases of Bersfort and Condor conductor bundles with span length of 200 m and with spacers located in constant distances were examined in detail. The maximum jump height and the conductor tension increase with distance between adjacent spacers, or in other words, they decrease with increasing number of spacers. When high amount of ice (50 mm in thickness) sheds, then increasing the number of spacers from 1 to 5 (or decreasing the distance between adjacent spacers from 100 m to 33 m) reduces the jump height above the unloaded position from 2-3 m to below 0.3 m. However, the bundle rotation cannot be reduced by increasing the number of spacers. The maximum drop of the loaded conductor is greater for even number of spacers, since in that case the maximum drop occurs at mid-span where the cable drop can be considerably greater. If the maximum drop below the unloaded position is considered, then its value varies by a maximum of 5% only for odd number of spacers, and it is about 5-15% greater when the number of spacers is even. Increasing the number of subconductors in the bundle reduces the severity of vibration. The maximum jump height of a single conductor in the cases considered is in the range of 5 to 10 m after shedding of heavy ice load (50-60 mm in thickness). When the conductor bundle is connected by 3 spacers, the jump height reduces to 0.5 to 0.6 m for twin bundles, and below 0.3 m for quad bundles. The conductor tension, however, is slightly lower (difference below 10%) for a single conductor during vibration, since no constraint is transmitted from other conductors in this case. The maximum jump height of the ice-shedding conductor and the maximum drop of the loaded conductor can be approximated as power functions of ice thickness and distance between adjacent spacers.*

Related publications: Kollár and Farzaneh (2008) [67], Kollár and Farzaneh (2013) [71]

Main contribution 4 *Ice shedding processes from transmission line conductors influence the severity of the resulting conductor vibration. An approach has been proposed to simulate various shedding processes through the removal in a defined sequence of the loads modelling ice accretion. The propagation velocity is controlled by associating each load with a time function which determines the removal time of that specific load. In the calculation, the load is multiplied in each time instant by the value the time function takes in that time instant. Models have been developed for the following ice shedding processes: (i) sudden and simultaneous ice shedding from the whole span or part of the span, (ii) propagation of ice shedding along the length of the span, and (iii) propagation of ice shedding along the length of the span with an additional downward pull induced at discrete locations along the span by the detachment of ice chunks.*

The numerical model was improved by considering several phases linked with interphase spacers, and it was validated by experimental observations. Transmission lines with 450-m-long spans were modelled either with a single conductor or with three conductors connected with interphase spacers. Simulation results show that the application of interphase spacers may reduce conductor rebound height above the loaded position by a factor of two approximately (from about 6 m to about 3 m), and thereby they contribute to preventing the reduction of conductor clearance and the risk of flashover during high-amplitude vibrations. The comparison of different shedding phenomena reveals that for a single conductor, there is no significant difference in the conductor rebound heights after propagating shedding and sudden shedding, but they are 10–30% greater after propagating detachment followed by sudden fall. For conductors linked with interphase spacers; however, the conductor rebound heights after propagating detachment followed by sudden fall are about 10–30% greater than after propagating shedding, and they are an additional 10–30% greater after sudden shedding.

Related publication: Kollár et al. (2013) [76]

Chapter 4

Vibration suppression of transmission line conductors

Natural phenomena leads to vibration of transmission line conductors that are suspended in the atmosphere. Section 3 discussed the sources of dynamic loads, together with the process and modelling of the resulting vibration. The present section is denoted to the methods that are proposed to attenuate conductor vibration and to reduce the harmful consequences.

Vibration characteristics depend on the inducing mechanism. The regular shedding of vortices due to wind results in high-frequency, low-amplitude vibration, the so-called aeolian vibration. Another type of wind-induced vibration, the galloping, is a movement-induced excitation, which leads to high-amplitude, low-frequency vibration. Vibration with a great jump height of the conductor may also be caused by shedding of heavy ice chunks from the suspended conductor, although the vibration decays due to structural damping and aerodynamic damping.

Damping devices to mitigate high-frequency cable vibration have been applied for decades. Viscous dampers and torsional dampers help reduce the amplitude of high-frequency vibrations in bridges and in transmission lines [113]. One of the most commonly used device is the Stockbridge damper whose dynamics was studied in a number of publications [8, 123, 124]. Several types of dampers have been developed, and they attenuate the vibration to a non-damaging level, but their application has limitations. The magnetorheological damper is another conventional vibration control technique that was implemented on stay cables of bridges [30]. An overview on the vibration control of transmission lines is presented in [12], including the description of different types of dampers. Overcoming the limitations of the passive dampers has become the motivation of further research to suppress conductor vibration. Saadabad et al. [109] designed a semi-active control method to suppress forced vibrations induced by wind excitation. Wang et al. [126] proposed a voice coil motor-based active vibration absorber for single and multiple frequency vibration control. An active vibration control method was proposed in a recent research [87]. The authors developed the idea of an electrical vibration absorber that can be installed at any location of the conductor and that is effective in a relatively wide frequency range. The effects of tuned-mass-dampers on reduction of forced vibration in

power transmission lines are investigated and optimum design of such dampers is presented in [1]. Vibration of transmission line conductors may be induced by ice accretion as well; therefore, research efforts has also been made to develop such devices for icing monitoring as the vibration-sag-tension-based sensor [34].

High-amplitude vibrations of transmission line conductors may be mitigated by the application of a control device, e.g. detuning pendulum, by forming bundles of several conductors with spacer dampers or by connecting phases with interphase spacers [26, 29]. The effects of spacer dampers on the vibration of conductor bundles following ice shedding were studied in [67, 71], whereas ice-shedding-induced vibrations of phases with interphase spacers were simulated in [76]. These methods and the dynamics of such systems formed the subject of Section 3.

When active control is applied, the time delay must also be taken into account, and it affects the dynamics of the controlled system. In general, increasing time delay tends to destabilize the dynamical system [16, 46, 116, 117]. When a system is controlled digitally by a computer, then samples are taken in finite time intervals and the action of control system is applied after processing the measured data. Thus, sampling delay and processing delay are included in the system that can be described by a discrete-time model. Time delay influences the stability of such systems as well [78]. Samukham et al. [110] proposed an approach to quickly generate stability charts for delay differential equations that govern dynamic processes involving time delay. In most of the studies, time delay is an undesired property of the dynamics, but it is also employed as a control design parameter. Olgac and Holm-Hansen [96] proposed an active vibration absorption technique that utilizes a controlled time delay in the feedback loop. This delayed resonator can remove oscillations for a wide range of frequencies with the proper selection of time delay and feedback gain. The authors also investigated how the delayed resonator could handle time dependent excitation frequency [97]. Active control via a time-delayed absorber was also studied experimentally in [131]. They carried out stability analysis, and examined the efficiency of the time-delayed absorber as well as the effects of the time delay and feedback gain on the performance of the absorber.

The present section describes the development of an active control methodology that successfully attenuates conductor vibration at the location where the control is applied. The section is divided into three main parts. The first part is based on [61] and introduces a simplified model for the conductor with a controlled vibration absorber, which is applicable for attenuating high-frequency, low-amplitude conductor vibration due to periodic excitation modelling aeolian vibration. The model considers the time delay that is always present in digital control due to sampling. The second part that is based on [62] takes into account the nonlinear elastic material behaviour of the conductor. Thus, the vibration control may successfully attenuate even high-amplitude vibration that follows ice shedding. Finally, the third part based on [63] improves the model introduced in the first part so that it involves such practical problems as time delay and backlash at the driving together, which leads to limitation in the applicability of control. Backlash influences control when the direction of control force changes, since the control force is

not transmitted in the small domain of backlash. The presence of time delay and backlash together results in a motion with some irregularity what justifes the detailed study of the dynamic behavior in order to evaluate the types of motion that may arise in such systems.

4.1 Control of conductor vibration with time delay

This section presents a simplified model for active vibration control with time delay of a suspended conductor exposed to periodic excitation, and to investigate the effects of time delay in the digital control. The periodic excitation considers the effects of wind under such circumstances that cause high-frequency, low-amplitude vibration. The PD control methodology is applied including time delay due to sampling the data that are used to determine the control force. The discrete-time model is then developed, the stability of the system is examined, and the effects of sampling delay on the control is discussed [61].

4.1.1 Mathematical model

Simplified model of conductor with vibration absorber exposed to wind

The simplified model of the conductor is a vibration system that considers the conductor at the position where the absorber is attached, together with its elasticity and structural damping, which determines the vertical motion of the suspended conductor. Simplified models of conductors in a bundle with spacer dampers were proposed in [68]. The mass of conductor was represented by a mass in the vibration system, which was assumed in the middle of the span where the spacer damper was also attached to the conductor. The elastic behaviour of the conductor was based on the statics of suspended cables. That model was applicable in mid-span only, but it also took into account the elasticity of the cable in the transverse direction. The motion in the present study is principally vertical; therefore, transverse motion is not simulated and corresponding parameters are not considered in the model. However, the model considers the natural frequencies of the modelled system, what is crucial for successful control of the vibration, and the elastic properties are calculated so that the model becomes applicable at positions other than mid-span.

The simplified model of the conductor with vibration absorber is the two degree-of-freedom (DOF) system depicted in Figure 4.1. The coordinate system is chosen so that x, y and z refer to the longitudinal, transverse and vertical directions, respectively. The simplified model describes motion in the vertical direction. The parameters m, k and c denote mass, spring stiffness and damping coefficient, respectively. Index 1 refers to the conductor where the excitation $F(t)$ acts, which considers the effects of the wind. Index 2 refers to the vibration absorber that can apply a control force between the conductor (m_1) and the absorber itself (m_2). The vibration absorber can be placed at different positions along the conductor, and its actual position is considered in the calculation of the parameters of the simplified conductor model.

The spring stiffness k_1 is determined by the elastic properties of the conductor, and it

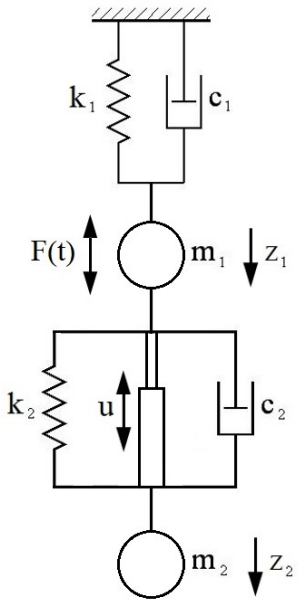

Figure 4.1: Simplified model of conductor with vibration absorber

can be calculated based on the statics of suspended cables [47]. If a vertical force P_z is applied on the conductor at a specified position x_p along the conductor, then the vertical displacement caused by this force at a position x along the span, where x_p and x are measured from the suspension point, can be obtained as follows

$$w_p(x) = \begin{cases} \frac{P_z L}{H+h_p}\left[\left(1-\frac{x_p}{L}\right)\frac{x}{L} - \frac{\mu g L h_p}{2HP_z}\frac{x}{L}\left(1-\frac{x}{L}\right)\right] & 0 \le x \le x_p \\ \frac{P_z L}{H+h_p}\left[\frac{x_p}{L}\left(1-\frac{x}{L}\right) - \frac{\mu g L h_p}{2HP_z}\frac{x}{L}\left(1-\frac{x}{L}\right)\right] & x_p \le x \le L \end{cases} \tag{4.1}$$

where μ is the mass per unit length of the conductor, g is the gravitational acceleration, L is the span length, and H is the initial horizontal tension in the conductor. The additional horizontal tension h_p due to the application of the concentrated force P_z is the solution of the following equation

$$h_p^3 + \left(2+\frac{\lambda_c^2}{24}\right)Hh_p^2 + \left(1+\frac{\lambda_c^2}{12}\right)H^2 h_p - \lambda_c^2 \frac{P_z H^3}{2\mu g L}\left(1+\frac{P_z}{\mu g L}\right)\left(\frac{x_p}{L}-\frac{x_p^2}{L^2}\right) = 0 \tag{4.2}$$

where the parameter λ_c is obtained from the following expression

$$\lambda_c^2 = \left(\frac{8f_s}{L}\right)^2 \frac{EA}{H\left(1+8\left(f_s/L\right)^2\right)} \tag{4.3}$$

The parameters E and A denote the Young's modulus and the cross section of the conductor, respectively, and f_s stands for sag. In order to obtain the spring stiffness, the relationship of the force P_z and the displacement w_p at the position x_p should be determined, which may be obtained after substituting $x = x_p$ in Equation (4.1). The relationship of the force P_z and the displacement w_p may closely be approximated by a third-order polynomial in a wide range of displacements [68]. However, the amplitude

of vibration under examination is in the range of conductor diameter; and a linear relationship is acceptable for such small displacements

$$P_z = k_1 w_p \tag{4.4}$$

The spring stiffness k_1 is obtained as the tangent of the line fitted on the curve provided by this relationship for small values of displacements.

The damping coefficient c_1 can be determined from the geometrical and material properties of the cable [67, 68]. However, the presence of the vibration absorber changes the damping coefficient locally; therefore, it is determined from comparing the decay of vibration with that obtained under the same conditions by the finite element model that was developed in [71].

The mass m_2 is a constant based on the design of the vibration absorber. The damping c_2 of the vibration absorber is so small that it is neglected in the model. The remaining parameters, the mass m_1 and the spring stiffness k_2 are determined together from the condition that the natural frequencies of the 2DOF system are equal to the first two natural frequencies, in vertical vibration modes, of the conductor with the vibration absorber. It should be noted that the higher natural frequency has to be adjusted in some cases in order to obtain real numbers for the mass and spring stiffness. The in-plane motion of cable vibration consists of antisymmetric and symmetric in-plane modes [47, 48]. The natural frequencies in the nth antisymmetric in-plane mode are given by

$$\omega_{n,a} = \frac{2n\pi}{L}\sqrt{\frac{H}{\mu}} \tag{4.5}$$

The natural frequencies in the nth symmetric in-plane mode are given by

$$\omega_{n,s} = \beta_n \sqrt{\frac{H}{\mu}} \tag{4.6}$$

where β_n is the solution of the following transcendental equation

$$\tan\left(\frac{1}{2}\beta_n L\right) = \frac{1}{2}\beta_n L - \frac{4}{\lambda_c^2}\left(\frac{1}{2}\beta_n L\right)^3 \tag{4.7}$$

These natural frequencies approximate closely those of the system where the vibration absorber is attached to the conductor. More accurate calculation of natural frequencies is possible by such a numerical method as the finite element model developed in [67].

The force $F(t)$ due to wind is considered by a harmonic excitation

$$F(t) = F_0 \cos(\omega t) \tag{4.8}$$

where F_0 is the amplitude, and ω is the circular frequency of excitation. The components of the force due to wind that is perpendicular to the plane of the suspended conductor are lift and drag, of which the fluctuating component that acts in the vertical direction is

the lift force. The amplitude of this force may be calculated from the following formula

$$F_0 = \frac{1}{2} C_L \rho A_p v^2 \tag{4.9}$$

where ρ is the air density, A_p is the cross-section that is exposed to wind, v is the wind speed, and C_L is the lift coefficient that may be obtained from experimental observations [95]. The circular frequency ω is obtained from the frequency that characterizes aeolian vibration.

Control methodology

The PD control methodology is applied in this study. Meng and Kollár [87] discusses some relevant details of the PID control methodology, including the advantage and disadvantage of the application of the integral term. The control force $u(t)$ without the integral gain can be written as follows:

$$u(t) = \mathbf{D}\mathbf{z}(t-\tau) = Pz_1(t-\tau) + D\dot{z}_1(t-\tau) \tag{4.10}$$

where

$$\mathbf{D} = \begin{bmatrix} P & D & 0 & 0 \end{bmatrix}; \quad \mathbf{z} = \begin{bmatrix} z_1 & \dot{z}_1 & z_2 & \dot{z}_2 \end{bmatrix}; \tag{4.11}$$

P and D are the proportional and differential gains, respectively, and τ denotes time delay. The control parameters are determined from the excitation frequency. When the excitation frequency is equal to the natural frequency of the simplified 1DOF system modelling the conductor, then the vibration amplitude of the mass in the primary system may significantly be reduced by the addition of an adequately tuned vibration absorber without applying active control. However, this vibration absorber does not work for different values of the excitation frequency. Therefore, the active control is applied and the proportional gain P is chosen so that together with the spring stiffness k_2, they provide the adequately tuned vibration absorber for the actual excitation frequency. The proportional gain that satisfies this condition is obtained by the following formula

$$P = k_2 - m_2\omega^2 \tag{4.12}$$

The vibration control works without differential gain D when small absolute values of the proportional gain P should be applied. However, when the excitation frequency is significantly greater than the natural frequency of the primary system, then the differential gain D will become necessary for reducing vibration amplitude. The choice of the differential gain will be explained after deriving the stability domain in Section 4.1.3.

The governing equations of motion of the 2DOF model including control can be organized in the following form:

$$\dot{\mathbf{z}}(t) = \mathbf{A}\mathbf{z}(t) + \mathbf{b}u(t) + \mathbf{c}F(t) = \mathbf{A}\mathbf{z}(t) + \mathbf{B}\mathbf{z}(t-\tau) + \mathbf{f}(t) \tag{4.13}$$

where $\mathbf{B} = \mathbf{b}\mathbf{D}$; $\mathbf{f} = \mathbf{c}F$ and

$$\mathbf{A}=\begin{bmatrix} 0 & 1 & 0 & 0 \\ -\frac{k_1+k_2}{m_1} & -\frac{c_1+c_2}{m_1} & \frac{k_2}{m_1} & \frac{c_2}{m_1} \\ 0 & 0 & 0 & 1 \\ \frac{k_2}{m_2} & \frac{c_2}{m_2} & -\frac{k_2}{m_2} & -\frac{c_2}{m_2} \end{bmatrix}; \quad \mathbf{b}=\begin{bmatrix} 0 \\ \frac{1}{m_1} \\ 0 \\ -\frac{1}{m_2} \end{bmatrix}; \quad \mathbf{c}=\begin{bmatrix} 0 \\ \frac{1}{m_1} \\ 0 \\ 0 \end{bmatrix}.$$

The first term includes system parameters, the second term with time delay includes the control force, and the third term includes the excitation force. Since a digital computer carries out the control, it is more convenient to use a discrete-time model.

Discrete-time model

The digital control takes samples of the controlled parameters at discrete time instants or sampling time, and the corresponding control force acts after the processing delay. The control is based on the sample-and-hold technique [100, 112]. The control force is held constant until the next sample is taken, and the time interval between taking samples and the processing delay are the same. Thus, if samples are taken at time instants $j\tau, j=1,2,\ldots$, then the control force is written in the form

$$u(t)=Pz_1((j-1)\tau)+D\dot{z}_1((j-1)\tau) \quad t\in[j\tau;(j+1)\tau) \tag{4.14}$$

It can be derived that the solution to system (4.13) at the first sampling takes the form

$$\mathbf{z}(\tau)=\mathrm{e}^{\mathbf{A}\tau}\mathbf{z}(0)+\int_0^{\tau}\mathrm{e}^{\mathbf{A}(\tau-s)}\mathrm{d}s\mathbf{b}u(0)+\int_0^{\tau}\mathrm{e}^{\mathbf{A}(\tau-s)}\mathrm{d}s\mathbf{c}F(0). \tag{4.15}$$

The initial state $\mathbf{z}(0), u(0), F(0)$ is assumed to be known. Then, the discrete-time model is described by the following equation

$$\mathbf{z}_{j+1}=\mathbf{A_d}\mathbf{z}_j+\mathbf{b_d}u_j+\mathbf{c_d}F_j \tag{4.16}$$

where $\mathbf{A_d}=\mathrm{e}^{\mathbf{A}\tau}$; $\mathbf{b_d}=\int_0^{\tau}\mathrm{e}^{\mathbf{A}(\tau-s)}\mathrm{d}s\mathbf{b}$; $\mathbf{c_d}=\int_0^{\tau}\mathrm{e}^{\mathbf{A}(\tau-s)}\mathrm{d}s\mathbf{c}$.

Similarly to Equation (4.13), the first term in Equation (4.16) includes system parameters, the second term includes the control force, and the third term includes the excitation force. In the dicrete-time model, however, the state $\mathbf{z}, u, F$ changes only after each time interval with duration τ.

4.1.2 Validation of the static and dynamic behaviour of the model

The model is applied for a representative example that considers the parameters of a small-scale laboratory model of a transmission line described in [71] with a vibration absorber attached at one-tenth of the span length. Parameters of the conductor and the span are given in the first column of Table 4.1, whereas the parameters of the mechanical model calculated as described in Section 4.1.1 are listed in the second column. Calculations

Parameters of conductor and span		Parameters of mechanical model	
Mass per unit length, μ (kg/m)	0.043	Mass of cable, m_1 (kg)	0.093
Span length, L (m)	6.4	Spring stiffness of conductor, k_1 (N/m)	50.3
Sag, f_s (m)	0.29	Damping coefficient of conductor, c_1 (Ns/m)	0.32
Conductor cross section, A (mm^2)	5.5	Mass of absorber, m_2 (kg)	0.16
Young's modulus, E (GPa)	18	Spring stiffness of absorber, k_2 (N/m)	86.82
Damping ratio, ζ	0.02	Damping coefficient of absorber, c_2 (Ns/m)	0

Table 4.1: Parameters of the suspended conductor and its mechanical model with vibration absorber

throughout this study including stability analysis were carried out using Matlab.

The static behaviour of the model is validated by calculating the displacements due to the application of concentrated forces, and comparing them to the displacements obtained under the same conditions by the finite element model of [71]. The force under the conditions describing a small-scale laboratory model of a transmission line is in the range of 0.1 N according to Equations (4.8)-(4.9), whereas it is at least an order of magnitude greater for full-scale lines. The force–displacement relationships are drawn in Figure 4.2a. The simplified model approximates closely, i.e. with difference in the range of few percent, the relationship obtained by the finite element model when the force is in the range of 0.1 N. The discrepancy grows above 20% as the force increases above 1 N. This observation is a consequence of the nonlinear material behaviour of the conductor. However, the parameter values in the simplified model depends on the structure examined, and a greater spring stiffness would be chosen to model a full-scale structure where significantly greater forces may act due to wind.

The dynamic behaviour of the model is validated via simulations of the free vibration following the removal of concentrated forces. The jump height after the force removal, i.e. the initial peak in the vibration, is determined and compared to the initial peak obtained under the same conditions by the finite element model of [71]. According to Figure 4.2b, the simplified model overestimates the jump height by about 20%. This discrepancy means a relatively small error in the displacement for forces in the range of 0.1 N, but it becomes substantial for greater values of the forces.

Consequently, the simplified model may be applicable when the external force is relatively small. It means that the model can be adjusted for different size of suspended conductors by changing parameter values as long as the force is small enough to cause only small-amplitude vibration. However, the nonlinear material behaviour of the conductor should be considered, when modelling high-amplitude vibration with relatively greater forces.

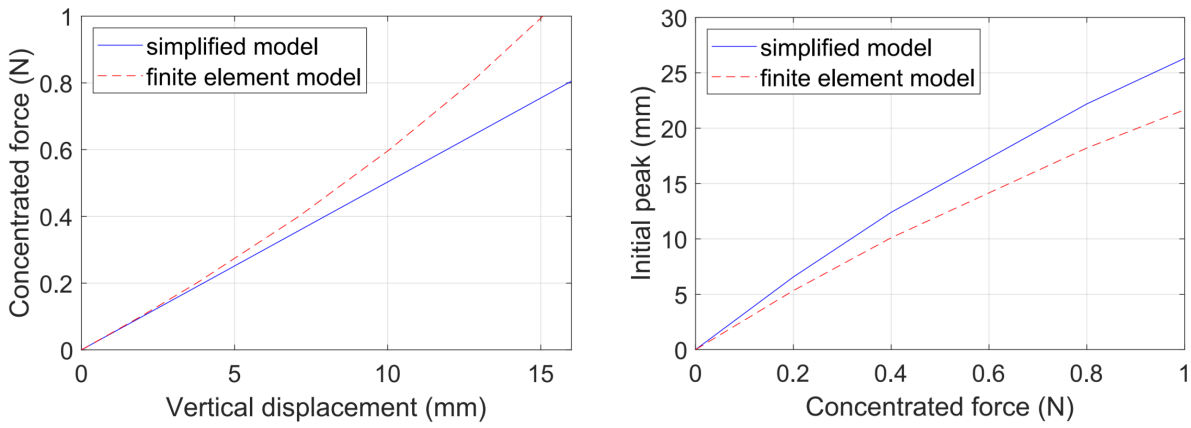

(a) (b)

Figure 4.2: Comparison of static and dynamic behaviour of the simplified model and the finite element model of [71]; (a) displacement due to concentrated force; (b) initial peak in the vibration following force removal

4.1.3 Stability of the controlled system

Stability analysis of the controlled system without time delay

The static equilibrium of the conductor is stable, but wind causes vibration that should be damped by the application of control. Mathematically, the $\mathbf{z} = \mathbf{0}$ equilibrium of system (4.13) without excitation and control (which is a linear homogenous system of ordinary differential equations) is stable, but vibration develops due to a harmonic excitation leading to a nonhomogenous system of equations. When feedback control is added, system parameters are changed so that the decay of vibration may be faster; however, the wrong choice of control parameters may make the equilibrium of the system unstable. The stability domain of the system without considering time delay can be obtained by the application of the Routh-Hurwitz criterion [28, 108]. The conditions when the Routh-Hurwitz criterion is satisfied guarantee local stability. The limitation of the linear stability analysis is based on the fact that great enough perturbation leads to nonlinear behaviour of the spring modelling conductor elasticity.

The $\mathbf{z} = \mathbf{0}$ equilibrium of the homogenous system with control is stable if the real parts of all of the characteristic roots, i.e. the zeros of the characteristic polynomial

$$p_1(\lambda) = \det(\lambda \mathbf{I} - (\mathbf{A} + \mathbf{B})) \tag{4.17}$$

are negative, where $\mathbf{I}$ is the identity matrix. This polynomial is a fourth-degree polynomial for the present model, i.e. $p_1(\lambda)$ can be written in the form

$$p_1(\lambda) = a_4\lambda^4 + a_3\lambda^3 + a_2\lambda^2 + a_1\lambda + a_0. \tag{4.18}$$

The Routh-Hurwitz criterion assures asymptotic stability if the coefficients of the polynomial $a_0, \ldots, a_4$ and the 2×2 and 3×3 Hurwitz determinants, H_2 and H_3, respectively,

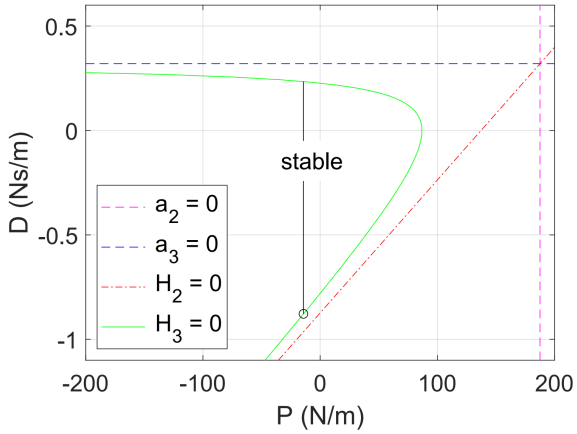

Figure 4.3: Stability domain in the plane of control parameters P and D for the system of conductor with absorber neglecting time delay; the boundary is determined by the curve $H_3 = 0$

are positive:

$$a_j > 0, \quad j = 0, \ldots, 4; \quad H_2 = \begin{vmatrix} a_1 & a_0 \\ a_3 & a_2 \end{vmatrix} > 0 \quad \text{and} \quad H_3 = \begin{vmatrix} a_1 & a_0 & 0 \\ a_3 & a_2 & a_1 \\ 0 & a_4 & a_3 \end{vmatrix} > 0. \tag{4.19}$$

Stability analysis is carried out for the example that is described by the parameters listed in Table 4.1, and the stability chart is constructed in the plane of control parameters. The coefficients a_0, a_1, a_4 of the characteristic polynomial are positive numbers independently on the control parameters. The coefficients a_2 and a_3 provide upper boundary for P and D, respectively. The corresponding lines are drawn by the dashed lines in Figure 4.3. The conditions for the Hurwitz determinants are plotted by the dash-dotted line and the continuous curve. The main part of the stability domain when all the four conditions are satisfied is found in the quarter where both of the control parameters are negative, but stability conditions are also satisfied for some small positive values of P and D.

The proportional gain P is chosen by Equation (4.12) as it was already explained in Section 4.1.1. In order to choose the differential gain D, the results of stability analysis and the behaviour of the particular solution are considered. For a given value of P, when D decreases inside the stability domain, i.e. when it increases in absolute value, the real part of the characteristic root with the greatest real part increases, then it becomes positive at the boundary of the stability domain. This is indicated by the vertical line in Figure 4.3 with a circle where it reaches the boundary of the stability domain. The stability domain is obtained by studying the homogeneous system; however, the motion of the system with the excitation force is described by the sum of the homogenous and particular solutions. Since the excitation is assumed to be harmonic, the particular solution can be written in the form

$$\mathbf{z}_p = \mathbf{z}_1 \cos(\omega t) + \mathbf{z}_2 \sin(\omega t). \tag{4.20}$$

After substitution into the equations of motion (4.13) with neclecting time delay and

assuming that $\mathbf{f} = \mathbf{f}_0 \cos(\omega t)$, the constants $\mathbf{z}_1$ and $\mathbf{z}_2$ are calculated as follows

$$\mathbf{z}_2 = \left(\omega \mathbf{I} + \frac{1}{\omega}(\mathbf{A} + \mathbf{B})^2\right)^{-1} \cdot \mathbf{f}_0 \quad \text{and} \quad \mathbf{z}_1 = -\frac{1}{\omega}(\mathbf{A} + \mathbf{B}) \cdot \mathbf{z}_2. \tag{4.21}$$

When D decreases for a fixed value of P, e.g. the pair of control parameters is varied along the vertical line toward the circle in Figure 4.3, the amplitude of the particular solution decreases. In other words, D should be chosen close to the border of the stability domain in order to obtain an oscillation with as small as possible amplitude. Therefore, first the value of P is determined by Equation (4.12), then the value of D is chosen near the boundary of the stability domain.

Stability analysis of the controlled system with time delay

In order to show the effects of time delay on the stability of the controlled system, stability analysis of system (4.16) without excitation is also carried out. Again, the $\mathbf{z} = \mathbf{0}$ equilibrium of system (4.16) without excitation and control is stable, but vibration develops due to the excitation. When feedback control is added, the decay of vibration may be faster; however, the equilibrium of the system becomes unstable for the wrong choice of control parameters. The $\mathbf{z} = \mathbf{0}$ equilibrium of the homogenous system with control is asymptotically stable if all of the characteristic roots are in modulus less than one, i.e. the zeros of the characteristic polynomial

$$\tilde{p}_2(\tilde{\nu}) = \det\left(\tilde{\nu}\mathbf{I} - (\mathbf{A_d} + \mathbf{b_d}\mathbf{D})\right) \tag{4.22}$$

lie inside the unit circle of the complex plane. Criteria for the asymptotic stability of the system considering time delay can be obtained from the Routh-Hurwitz criterion after applying the Moebius-Zukovski transformation

$$\tilde{\nu} = \frac{\nu + 1}{\nu - 1}. \tag{4.23}$$

Thus, the polynomial $\tilde{p}_2(\tilde{\nu})$ given by Equation (4.22) has all its roots in the interior of the unit circle if and only if the polynomial

$$p_2(\nu) = (\nu - 1)^4 \tilde{p}_2\left(\frac{\nu + 1}{\nu - 1}\right) = b_4\nu^4 + b_3\nu^3 + b_2\nu^2 + b_1\nu + b_0 \tag{4.24}$$

satisfies the Routh-Hurwitz criterion. In other words, conditions (4.19) after replacing the coefficients a_j by $b_j, j = 0, \ldots, 4$ guarantee stability.

Stability charts are drawn in Figure 4.4 for two different values of time delay. The conditions $b_3 > 0$ and $b_4 > 0$ are satisfied in the entire domain shown in the figure; therefore they are not indicated. When time delay is present, the size of the stability domain becomes finite, and it decreases with increasing time delay. The stability domain is bounded by the curves $b_0 = 0$ and $H_3 = 0$. It should be noted that although the size of stability domain shrinks with increasing time delay, the case $P = 0; D = 0$ always remains

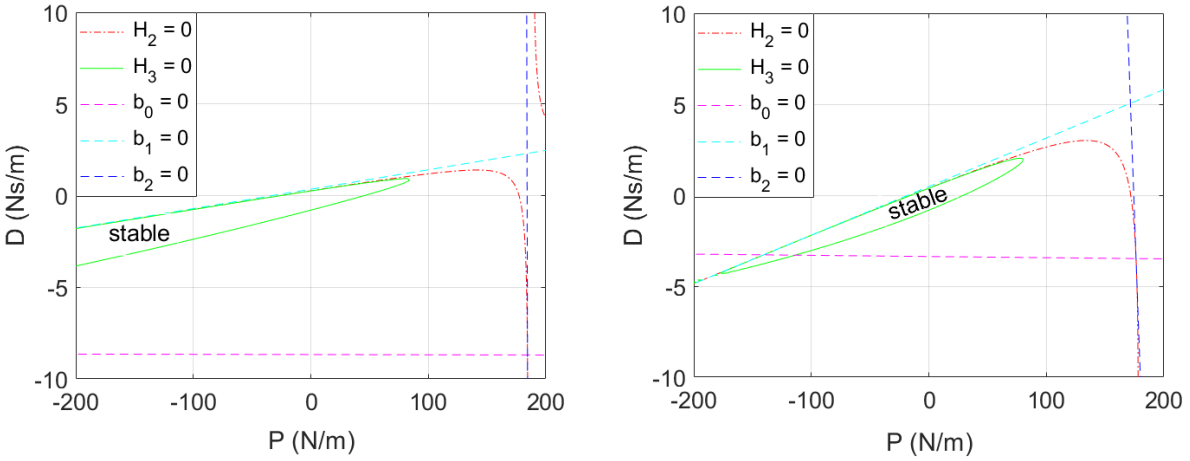

(a) (b)

Figure 4.4: Stability domains on the plane of control parameters P and D for the system of conductor with absorber considering time delay τ; the boundary is determined by the curves $b_0 = 0$ and $H_3 = 0$; (a) $\tau = 0.02$ s; (b) $\tau = 0.04$ s

stable, because the equilibrium of the system without excitation and control is stable. It will be shown in Section 4.1.4 that the amplitude of oscillation due to excitation cannot be decreased by the application of control if the time delay is not small enough.

4.1.4 Dynamics of the controlled system with time delay

Dynamics of the uncontrolled and controlled systems is compared in this section. This study reveals the effects of control on the vibration under consideration together with the effects of time delay due to sampling. The success of control and the sensitivity on the time delay depend on the excitation frequency; therefore, results are presented for varying values of this parameter.

The subject of this study is the mechanical model whose parameters are listed in Table 4.1. The amplitude of the excitation force is obtained from Equation (4.9), and it is in the range of 0.1 N and 1 N in a 1-m-long section of a small-scale model and in a full-scale model, respectively, of a suspended conductor. The excitation frequency is varied up to 50 Hz. Time histories were examined for excitation amplitude of 0.2 N and for excitation frequency of 20 Hz in [61]. Results revealed that the application of control reduced the initial peak during the vibration to less than one-fifth of its value without control, although this reduced value was more than double with a time delay of 10 ms. It took several seconds to reach the steady-state amplitude without control, whereas it was reached in a fraction of a second with control. The rate of reduction in the initial peak and in the vibration amplitude depends on the excitation frequency and on the time delay. This will be discussed in the following.

The vibration amplitude may be reduced close to zero even without the application of active control when the excitation frequency is equal to the natural frequency of the primary system including mass m_1 and spring k_1. This is the case of passive control

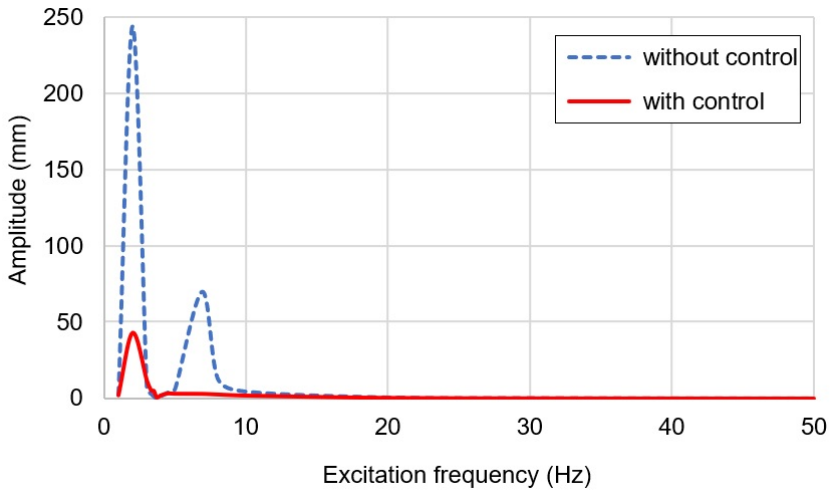

Figure 4.5: Vibration amplitude of mass m_1 with and without active control for amplitude of excitation force $F_0 = 1$ N

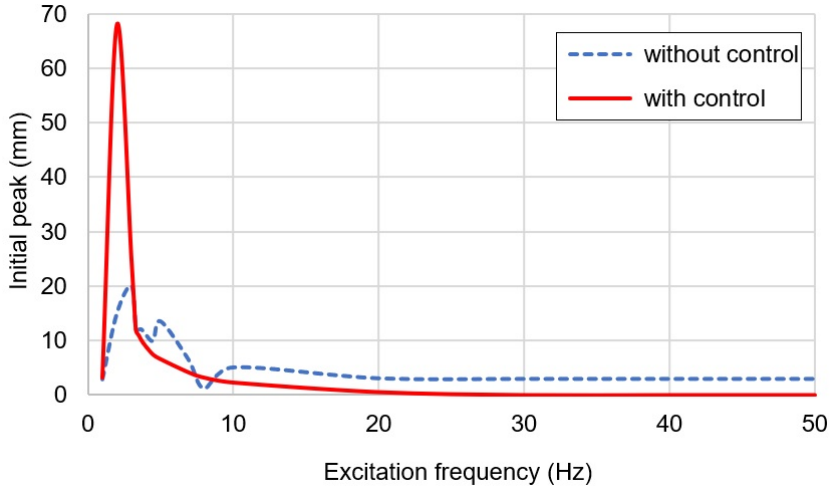

Figure 4.6: Initial peak in the vibration of mass m_1 with and without active control for amplitude of excitation force $F_0 = 1$ N

with the application of a dynamic vibration absorber (see e.g. [56]), because the auxiliary system including mass m_2 and spring k_2 is attached. However, two high peaks occur when the excitation frequency is equal to the natural frequencies of the 2DOF system. The amplitudes at these peaks can be reduced by a factor of more than ten by the application of active control. When the excitation frequency increases, then the amplitude is reduced to a smaller extent. The effects of active control on steady-state amplitude becomes negligible after the excitation frequency exceeds 10 Hz and 20 Hz when the amplitude of excitation force is 0.1 N and 1 N, respectively. These tendencies for the latter case can be observed in Figure 4.5.

The active control also reduces significantly the initial peak in the vibration. This effect holds in almost the entire range of excitation frequencies considered, i.e. up to 50 Hz, except for excitation frequencies close to the natural frequencies of the 2DOF system. These results can be observed in Figure 4.6.

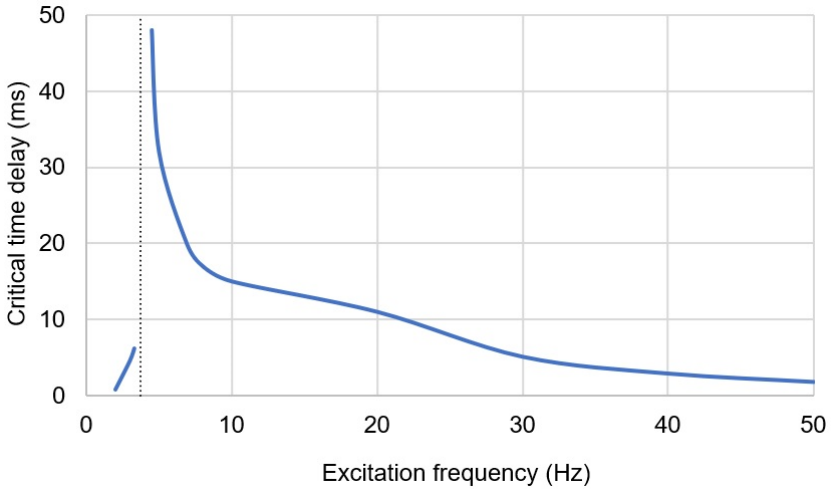

Figure 4.7: Variation of critical time delay with excitation frequency

Time delay due to sampling in the control means that the control required at a given state of the system is applied after the next sample is taken and the system is already in a different state. Obviously, if this delay is too long, then successful control is impossible. The critical value of time delay above which the control cannot be successful is plotted against the excitation frequency in Figure 4.7. The critical time delay is greatest when the excitation frequency is equal to the natural frequency of the primary system, which is 3.7 Hz in the case studied (see the dotted vertical line in Figure 4.7). As it was discussed earlier, active control is not necessary in this case, or in other words, the control parameters are chosen closely to zero. Thus, increasing sampling time does not influence the motion considerably, because passive control works and the active control force that is applied with delay is approximately zero. For smaller values of the excitation frequency, the critical time delay becomes quite small, i.e. in the range of 1–10 ms. However, the 3.7 Hz frequency mentioned above is around the lower limit of frequencies that characterizes the vibration during such phenomena as aeolian vibration. On the other hand, when the excitation frequency increases, then the critical time delay decreases, but it does not drop below 10 ms for excitation frequencies smaller than 20 Hz. Then, after further increasing the excitation frequency, the critical time delay approaches 1 ms when the excitation frequency exceeds 50 Hz. This result reveals a limitation of the control applied, which concerns the case of high excitation frequency where very quick sampling is required for successful active control. It should be noted that for such high frequencies the amplitude of vibration is very small even without the application of active control; however, the reduction of the initial peak by the control is significant. Therefore, a possible solution for such high-frequency excitations is the application of active control initially, and then turning off the active control.

The active control proposed successfully reduces the initial peak of the vibration in the frequency range that characterizes aeolian vibration. It is also successful to reduce vibration amplitude from the lower limit of this frequency range up to about 10 Hz, depending on further parameters as the amplitude of excitation force. However, the

control strategy of this model cannot attenuate high-amplitude vibrations. This limitation could be overcome after improving the model by considering the nonlinear material behaviour of the conductor, which is the subject of Section 4.2.

4.2 Ice-shedding-induced vibration of conductors with active vibration control

The method proposed for attenuating vibration of suspended conductors as described in the previous section was improved in [62] by considering the nonlinear elastic material behaviour of the conductor. Such vibration control may successfully attenuate even high-amplitude vibration that follows ice shedding.

Ice mass reduction or ice shedding from suspended cables or conductors may be induced by different physical mechanisms: ice melting, ice sublimation, and mechanical ice breaking [20]. The shedding process is influenced by several factors including ice properties, meteorological parameters, and radiation intensity, which was analyzed in [133]. Kálmán et al. [54] studied the ice detachment mechanism together with the dynamic effects of the resulting ice shedding and proposed an ice failure model. This model was later improved in [53] by considering the bending strain in the ice deposit, the adhesive force at the ice–cable interface and the cohesive force within the ice. Study on the dynamic response due to ice shedding was detailed in Section 3.1.3, whereas the research on the attenuation of conductor vibration was summarized in the introductory part of Section 4.

This section presents a model of vibration control, which considers the nonlinear elastic behaviour of the conductor, and consequently, it is applicable to attenuate high-amplitude vibration at the position where the absorber is attached to the conductor. The model includes the conductor and the absorber whose weight acts as a concentrated load on the conductor. The mechanical behaviour of this system is validated by simulating the application of concentrated load on the conductor and load removal from the conductor, then comparing the results with those obtained by the finite element model that closely reproduced the experimental observations in [71]. The present study develops the theory of the application of control in this model, which simulates the ice-shedding-induced vibration of a conductor with active vibration control at a specific position. Finally, controlled vibration following ice shedding from a full-scale line is simulated, and conclusions from the results obtained are drawn [62].

4.2.1 Model of conductor vibration

The mathematical model constructed in Section 4.1.1 is a 2DOF model that considers a suspended conductor with vibration absorber. The conductor is taken into account at the position where the vibration absorber is attached, but the model is validated by experimental observations and a finite element model of the entire suspended conductor. This section describes only the modifications made on this model in order to consider the nonlinear elastic material of the conductor.

Model of conductor with vibration absorber

The mechanical model depicted in Figure 4.1 is modified as follows. First, the excitation $F(t)$ is not applied, because ice shedding is followed by free vibration. Second, the elasticity of the conductor is modelled by a nonlinear spring; thus, the spring stiffness cannot be described by a single parameter.

Parameters describing the relationship between a vertical concentrated force applied at a specified position and the vertical displacement of the conductor at the same position due to this force can be derived from Equations (4.1)-(4.3). However, the linear relationship (4.4) is replaced by a third-order polynomial that approximates closely the force-displacement relationship in a wide range of displacements [68]

$$P_z = k_{11} w_p + k_{12} w_p^2 + k_{13} w_p^3. \tag{4.25}$$

The spring stiffness practically means three parameters, i.e. the coeffcients k_{11}, k_{12} and k_{13} in Equation (4.25). Since zero force causes no displacement, constant term does not appear in the nonlinear expression. In order to determine the coeffcients k_{11}, k_{12} and k_{13}, the displacements were determined for different forces, and a cubic polynomial was fit to the data obtained.

The mass m_2 is a constant based on the design of the vibration absorber. The mass of conductor m_1 and the spring stiffness of absorber k_2 are calculated from the equality of the natural frequencies of the 2DOF system and the conductor. The same idea was applied in Section 4.1.1, but the consideration of natural frequencies is different in the present model. One of them is that obtained at the first in-plane (vertical) vibration mode, whereas the second one is chosen so that the mode shape has local maximum close to the position where the absorber is installed. In this study, vibration at mid-span or at 10% of the span is examined; correspondingly, the other vertical modes considered is the 2nd and the 5th or 6th modes, respectively. These are the first antisymmetric in-plane mode (with local maximum at mid-span), and the third antisymmetric or third symmetric in-plane mode (with local maximum close to 10% of the span).

The calculation of the damping coefficients c_1 and c_2 is different from that in the model of Section 4.1.1. The damping coefficient of conductor c_1 is calculated from the parameters of a single DOF vibration system describing the conductor at the position where the vibration absorber would be placed, but without the absorber. The natural circular frequency ω_n of this system can be calculated after linearization so that the stiffness k_{1lin} is obtained as the tangent to the force-displacement curve (4.25) at the displacement caused by the weight of the absorber. The damping ratio ζ is obtained according to experimental observations in [71]. Then, the damping coefficient c_1 is calculated from

$$c_1 = 2 m_1 \omega_n \zeta \quad \text{with} \quad \omega_n = \sqrt{\frac{k_{1lin}}{m_1}} \tag{4.26}$$

The damping coefficient of the vibration absorber c_2 is determined from comparing the vibration following load removal at the position where the absorber is fixed with that

obtained under the same conditions by the finite element model that was developed and validated by experimental observations in [71].

Ice load and ice shedding

Ice load on the conductor cannot simply be simulated by adding the weight of ice to the concentrated force acting on mass m_1, because ice is distributed along the conductor. First, the distributed load is determined from the ice properties. Assuming annular ice shape and uniformly distributed ice along the conductor, the ice load p in a unit length of the conductor is calculated as follows

$$p = \rho_{ice} \frac{(d_c + 2b_{ice})^2 - d_c^2}{4} \pi \tag{4.27}$$

where ρ_{ice} is the ice density, d_c is the conductor diameter, and b_{ice} is the ice thickness. If the distributed load acts between positions x_1 and x_2, then the displacement due to this distributed load at any position x along the span is obtained from the expression [47]

$$w_d(x) = \begin{cases} \frac{pL^2}{H+h_d}\left[\left(\frac{x_2-x_1}{L} - \frac{x_2^2-x_1^2}{2L^2}\right)\frac{x}{L} - \frac{\mu g h_d}{2pH}\left(\frac{x}{L} - \left(\frac{x}{L}\right)^2\right)\right] & 0 \le x \le x_1 \\ \frac{pL^2}{H+h_d}\left[-\frac{1}{2}\left(\frac{x_1}{L}\right)^2 - \frac{x_2 x}{L^2} - \frac{1}{2}\left(\frac{x}{L}\right)^2 - \frac{x_2^2-x_1^2}{2L^2}\frac{x}{L} - \frac{\mu g h_d}{2pH}\left(\frac{x}{L} - \left(\frac{x}{L}\right)^2\right)\right] & x_1 \le x \le x_2 \\ \frac{pL^2}{H+h_d}\left[\frac{x_2^2-x_1^2}{2L^2}\left(1 - \frac{x}{L}\right) - \frac{\mu g h_d}{2pH}\left(\frac{x}{L} - \left(\frac{x}{L}\right)^2\right)\right] & x_2 \le x \le L \end{cases} \tag{4.28}$$

The additional horizontal tension h_d due to the application of the distributed load p is the solution of the cubic equation

$$\begin{aligned} h_d^3 \;+\; & \left(2 + \frac{\lambda_c^2}{24}\right) H h_d^2 + \left(1 + \frac{\lambda_c^2}{12}\right) H^2 h_d - \frac{\lambda_c^2}{2}\frac{pH^3}{\mu g}\left(\frac{1}{2}\frac{x_2^2 - x_1^2}{L^2} - \frac{1}{3}\frac{x_2^3 - x_1^3}{L^3}\right) \\ - \; & \frac{\lambda_c^2}{2}\frac{p^2 H^3}{(\mu g)^2}\left(\frac{1}{3}\frac{x_2^3 - x_1^3}{L^3} - \left(\frac{x_1}{L}\right)^2 \frac{x_2 - x_1}{L} - \frac{1}{4}\left(\frac{x_2^2 - x_1^2}{L^2}\right)^2\right) = 0 \end{aligned} \tag{4.29}$$

The vertical displacement due to ice load (4.27) at the position where the absorber is attached is obtained from Equation (4.28), and it is applied as initial displacement of mass m_1 together with zero initial velocity when simulating ice shedding. Assuming sudden ice shedding at time instance $t = 0$, i.e. when the simulation begins, there is no ice on the conductor during the vibration. If the entire conductor is loaded by ice before shedding, then the substitutions $x_1 = 0$ and $x_2 = L$ should be applied in Equations (4.28) and (4.29). Note that partial ice shedding may also be simulated. In this case, $x_1 > 0$ and/or $x_2 < L$ after ice shedding. Then, the vertical displacement at time instance $t = 0$ is obtained from Equation (4.28), and the remaining ice mass has to be considered in the parameters describing the conductor.

Vibration control

The control methodology applied is based on that described in Section 4.1.1. Time delay is not considered in the present model; therefore, the control force is provided by Equations

(4.10)-(4.11) with $\tau = 0$. The control parameter P is determined from Equation (4.12) where ω in this case is equal to the circular frequency at one of the dominant in-plane (vertical) vibration modes of the conductor. The effects of differential gain D is negligible if the proportional gain is chosen properly; however, a small value (i.e. 2–3 orders of magnitude smaller than P) may help reduce the first peak if the proportional gain is not optimum.

The governing equations of motion of the 2DOF model including control can be organized in the following form

$$\dot{\mathbf{z}}(t) = \mathbf{A}\mathbf{z}(t) - \mathbf{b}z_{nl}(t) + \mathbf{b}u(t) \tag{4.30}$$

where $z_{nl} = k_{12}z_1^2 + k_{13}z_1^3$, and the matrix $\mathbf{A}$ and the vector $\mathbf{b}$ are given after Equation (4.13). The second term on the right-hand side considers the nonlinear terms due to the nonlinear spring stiffness of the conductor.

Apart from the control strategy, the position and the number of absorbers influence the successful application of vibration control. In this study, the goal is to develop the idea of control and to show that it works locally on the conductor. Vibration control may be improved if more than one absorber are applied at different positions, but the optimum arrangement depends on the specific configuration of the transmission line. A rough recommendation on the number of absorbers may be based on the need for control of vibration following partial ice shedding. If ice sheds partially from a region where absorber is not attached, then the effects of control may not be sufficient to attenuate vibration signifcantly. However, too many absorbers overload the conductor; moreover, if ice sheds only from a short part of the conductor, then the resulting vibration is not severe.

4.2.2 Parameter set-up

Model parameters are set up for two cases: (i) small-scale model that was presented and validated by experimental observations in [71]; (ii) full-scale model of a span including Bersfort conductor. The parameters determined by the procedure described below are listed in Table 4.2 together with the parameters of the conductor and span that are modelled.

The spring stiffness of the conductor is determined as explained in Section 4.2.1, and coefficients in a cubic approximation are obtained at the position of absorber as listed in Table 4.2. Once the spring stiffness of the conductor is determined and the mass of the absorber is known, then the mass of conductor and the spring stiffness of absorber in the simplifed model may be calculated as explained in Section 4.2.1.

The damping ratio of the conductor was determined using the finite element model of [71] with Rayleigh damping. The constants in the Rayleigh damping were obtained by comparing the decay of vibration in the simulation and that in the experiments of [71]. In the simplified model, these damping ratios were applied to calculate the damping coefficient by Equation (4.26).

Parameters of conductor and span	Small-scale	Full-scale	Parameters of mechanical model	Small-scale	Full-scale
Mass per unit length, μ (kg/m)	0.043	2.37	Mass of cable, m_1 (kg)	0.0992	130.9
Span length, L (m)	6.4	200	Spring coefficients, k_{11} (N/m), k_{12} (N/m^2), k_{13} (N/m^3)	7.5; 158; 4019	1436; 801.7; 186.7
Sag, f_s (m)	0.29	6.0	Damping coefficient of conductor, c_1 (Ns/m)	0.099	18.2
Conductor cross section, A (mm^2)	5.5	747.1	Mass of absorber, m_2 (kg)	0.16	13
Young's modulus, E (GPa)	18	67.6	Spring stiffness of absorber, k_2 (N/m)	56.0	130.3
Damping ratio, ζ	0.02	0.02	Damping coefficient of absorber, c_2 (Ns/m)	4.0	1.0

Table 4.2: Parameters of the conductor and its mechanical model with vibration absorber for two cases

The damping coefficient of the vibration absorber in the small-scale model is obtained by minimizing the discrepancy between the periods, the first peaks and the decays of the vibration following the removal of 0.2 N at 10% of the span where the absorber is fixed with that obtained under the same conditions by finite element modelling. For the damping coefficient of the vibration absorber in the full-scale model, the load removed is 200 N at 50% of the span where the absorber is attached.

4.2.3 Model validation

The static and dynamic behaviour of the simplified model is validated by comparing its predictions to those obtained by the finite element model that closely simulated the experimental observations in [71].

The static behaviour of the model may be validated by calculating displacements due to vertical concentrated loads and comparing them to displacements obtained from theory or from finite element modelling. For the small-scale span, the finite element model provides displacements close to those obtained from the theory in the entire domain shown by the dots in Figure 4.8a. The domain of applicability using the simplified model is limited, but it is still substantially more extended than that obtained by the model in Section 4.1.1 (cf. Figures 4.2a and 4.8a). The simplified model provides values close to those obtained from the theory (i.e. the discrepancy is within a few %) for vertical displacements of 7–8 cm below and above the unloaded position. Nevertheless, displacements outside this range are not expected at 10% of the span even after shedding of heavy load from the span. In case of the full-scale span, the simplified model provides vertical displacements at mid-span close to those obtained from the theory in the entire domain shown in Figure 4.8b, i.e. from -2.5 m to 3 m.

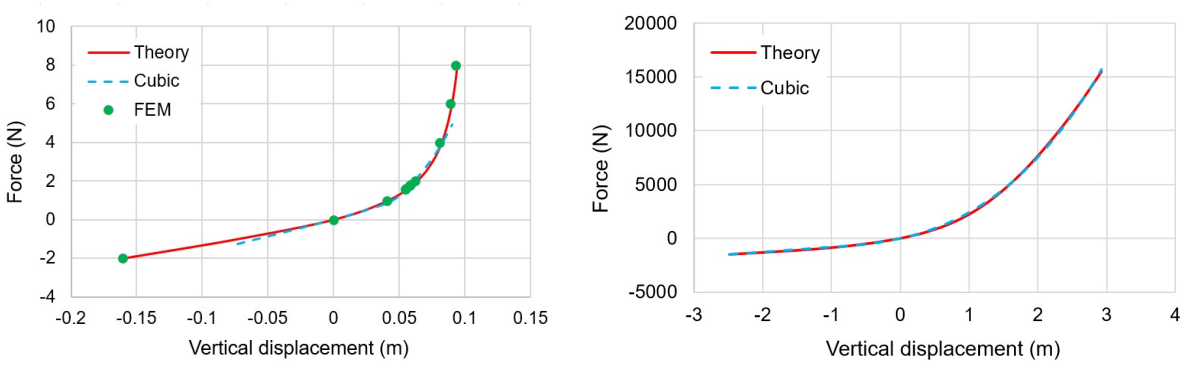

(a) (b)

Figure 4.8: Vertical displacement of conductor due to concentrated force; (a) small-scale model, force applied at 10% of span; (b) full-scale model, force applied at 50% of span

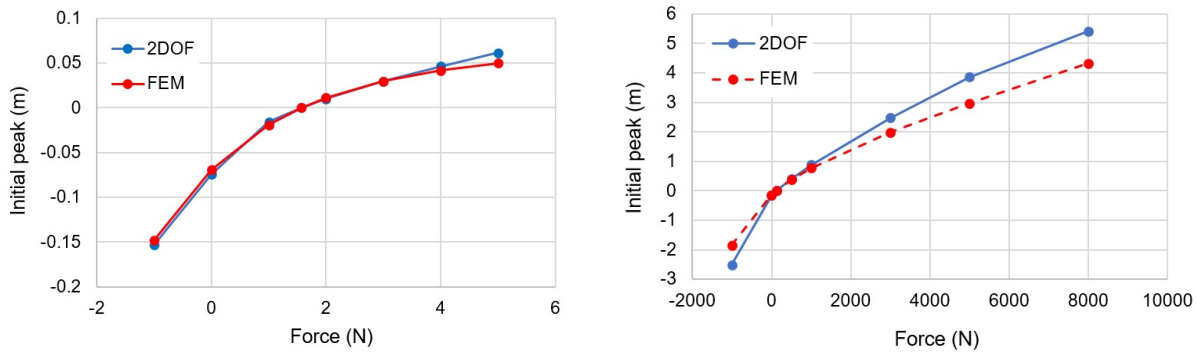

(a) (b)

Figure 4.9: Comparison of dynamic behaviour of the simplified model and the finite element model of [71] by initial peak in the vibration following load removal at the position of absorber; (a) small-scale model, removal at 10% of span; (b) full-scale model, removal at mid-span

The dynamic behaviour of the model is validated via simulations of the free vibration following the removal of concentrated forces. The rebound height after the force removal, i.e. the initial peak above the loaded position, is determined and compared to that obtained under the same conditions by the finite element model. Figure 4.9 reveals that in case of the small-scale span increasing discrepancy between the two curves occurs when approaching the highest load, which is the upper limit of applicability of the cubic approximation of the nonlinear spring modelling the elasticity of the conductor. In case of the full-scale span, the greatest discrepancies obtained are in the range of 20–25%. Although similar discrepancies can be observed in some cases of the removal of smaller loads from the full-scale span, but then the period and decay of vibration are closely predicted. Consequently, the simplified model is reliable to simulate vibration at the position of absorber when the external force and the corresponding displacement are in the range of applicability of the model, which covers the domain of practical interest.

4.2.4 Vibration of conductor with damper following ice shedding

This section is divided into three parts. First, vibrations following ice shedding from the small-scale model without and with active control are presented. Then, the results of the vibration control applied for the full-scale model are shown.

Vibration following ice shedding without active control

Ice is modelled as a load distributed uniformly along the span. The change in vertical position due to the distributed load at any horizontal position of the conductor can be calculated from Equation (4.28). First, the increase of sag and the additional conductor tension due to the distributed load are calculated, and then the vertical displacement at the position of absorber due to its weight is determined. In this latter calculation, the following parameters should be modifed in Equations (4.1)-(4.3): the mass per unit length considers the mass of conductor itself together with the ice mass; the initial horizontal tension in the conductor is increased by the additional tension obtained from the distributed load; and the sag is increased according to the profile of conductor with ice load.

Ice with annular shape with thickness of 5 mm and density of 900 kg/m^3 is assumed on the small-scale model, and the corresponding distributed load is calculated by Equation (4.27). The initial vertical position of the conductor at the location of absorber is determined as the sum of the vertical displacements of the conductor due to the distributed load and due to the weight of absorber. Ice shedding is simulated by considering this vertical position as initial condition, which is not the equilibrium of the system; thus, vibration is initiated and the system will approach its equilibrium as vibration decays. The vibration following ice removal, but keeping the absorber on the conductor is also simulated by the finite element model. The first few seconds of the vibrations obtained by the two models are plotted in Figure 4.10. There is a close agreement between the time histories, but the vibration in the simplified model is delayed by 0.05 s due to a small peak at the beginning of vibration, which is not reproduced by the simplified model.

When ice sheds from a conductor, vibration develops where the first peak, or one of the first few peaks, in the vertical displacement is usually maximum, then the vibration decays due to the structural damping of the conductor. The conductor tension also reaches its maximum value at the beginning of vibration, then it approaches the value that describes the static equilibrium. The application of a vibration damper reduces the conductor rebound height, or in other words, the first peak in the vertical displacement; and it also contributes to eliminating the first few peaks in conductor tension since its weight acts as a concentrated force in the conductor even if control is not activated. A drawback of attaching a damper to the conductor is that it acts as an additional load. However, the additional conductor tension due to the weight of damper is relatively small in case of the full-scale model. The vertical displacements at 10% or at 50% of the span increase by 4% and 1.6%, respectively. Furthermore, when heavy ice load (50 mm in thickness), is added to the conductor, then the additional vertical displacement reduces well below 1% as compared to the loaded profile. The conductor tension increases by 1.4% or 3.8% when

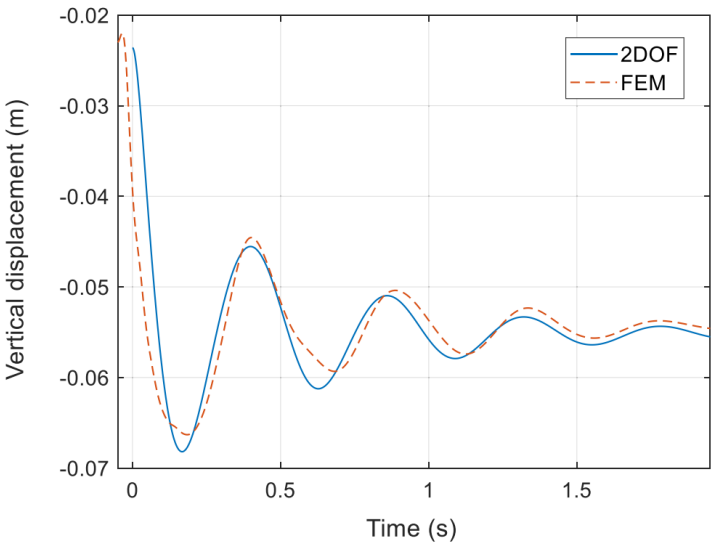

Figure 4.10: Time histories obtained after ice shedding by the simplified model and by the finite element model

the damper is attached at 10% or at 50% of the span, respectively. If the same heavy ice load is considered on the conductor, then the additional conductor tension reduces well below 1% as compared to the tension in the loaded conductor. These results suggest that the additional displacement and the additional tension due to the damper or vibration absorber do not increase signifcantly the risk of flashover or conductor rupture.

Controlled vibration following ice shedding

The PD control described in Section 4.2.1 is applied in this section in order to attenuate vibration due to ice shedding. The application of proportional gain is necessary in order to reduce the peaks in the vibration, and the differential gain may contribute to further decrease the first peak, but the wrong choice may slow down the decay of vibration. Three time histories are plotted in Figure 4.11. They are calculated by the simplified model and obtained at 10% of the span during the vibration following the shedding of ice defined above in this section. The initial position at 10% of the span where the damper is attached is 2.36 cm below the position that would be obtained from the catenary profile without any load. Since the damper applies a concentrated load at this position, this point of the conductor moves downward after ice shedding to reach the equilibrium position without ice at 5.52 cm below the catenary profile. The lowest position during the vibration reaches 6.82 cm (or 1.30 cm below the equilibrium position without ice) without control. This value can be reduced to 5.856 cm (or 0.336 cm below the equilibrium position without ice) by the application of proportional gain, and it can further be reduced to 5.83 cm (or 0.31 cm below the equilibrium position without ice) if differential gain is also applied in the control. According to the data written in parentheses, the drop below the equilibrium position with damper and without ice, is reduced to about one-fourth of the value obtained without control.

The proportional gain was determined as defined by Equation (4.12), but the adequacy

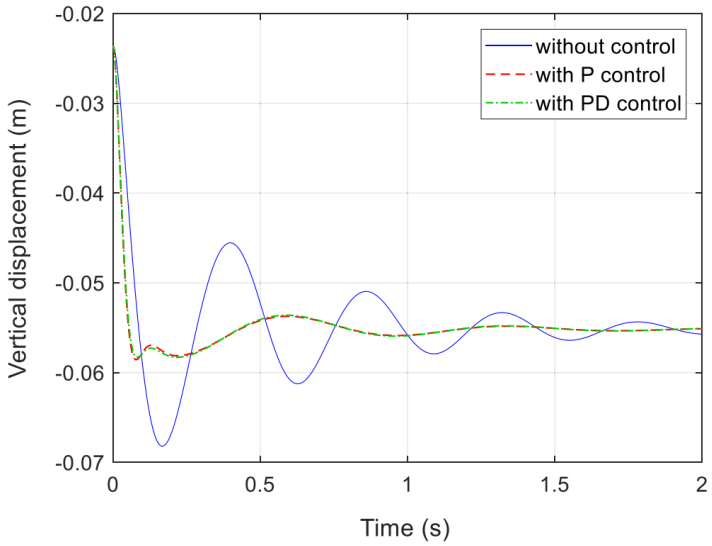

Figure 4.11: Time histories of conductor vertical displacement at 10% of span where damper is attached during vibration following ice shedding in the small-scale model without and with control (simulation by simplified model)

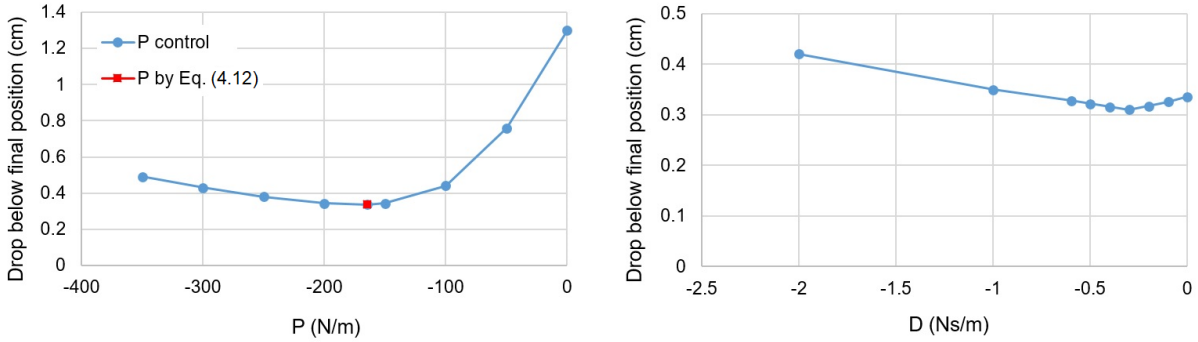

(a) (b)

Figure 4.12: First peaks, i.e. conductor drops, at the position of damper during vibration following ice shedding; (a) P is varied, $D = 0$; (b) $P = -164.6$ N/m, D is varied

of this choice is verified numerically. Figure 4.12a plots the conductor drop below equilibrium position without ice as a function of proportional gain. The conductor drop obtained for the chosen value of proportional gain is shown by the red square, which is among the smallest drops that may be achieved only by the application of proportional gain. According to Figure 4.12b, the minimum drop may further be reduced by applying a small value of differential gain; however, if the absolute value of differential gain is too high, i.e. at least in the range of 1 Ns/m, then the drop will increase.

Application of vibration control for full-scale model

Ice with annular shape with thickness of 50 mm and density of 900 kg/m^3 is assumed on the full-scale model of Bersfort conductor described in Section 4.2.2. Vibration damper is assumed to be attached at mid-span, i.e. 50% of the span. The initial position is

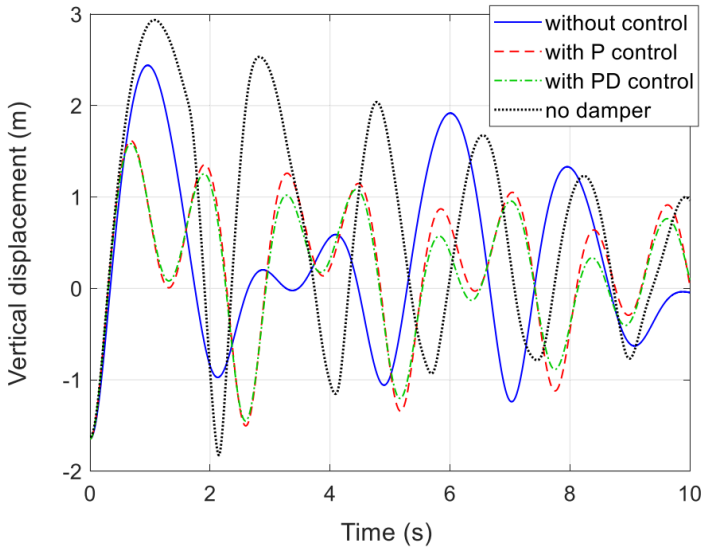

Figure 4.13: Time histories of conductor vertical displacement at mid-span where damper is attached during vibration following ice shedding in the full-scale model without and with control (simplified model) and without damper (finite element model)

determined and ice shedding is simulated in the same manner as explained for the small-scale model. The initial position at mid-span due to ice load is 1.62 m below the unloaded position in the catenary curve, and it increases by an additional 0.0269 m due to the weight of the damper. These values are obtained from the calculation detailed in Section 4.2.1, and the parameter values listed in Table 4.2. The equilibrium position at mid-span of the unloaded conductor with damper is 0.0847 m below the unloaded position in the catenary. The sudden shedding of the 50-mm-thick ice load leads to a great rebound height of the conductor. The first peak reaches 2.937 m above the unloaded position (see the curve 'no damper' in Figure 4.13 obtained by finite element simulation). This peak is reduced to 2.441 m when the damper is attached at mid-span, but control is not activated (curve 'without control' in Figure 4.13). The application of control with proportional gain contributes to further decreasing the peak to about two-third of its value without control, and the application of differential gain causes an additional few percents reduction in the peak. It should be noted that smaller value of the first peak could be reached by further increasing the absolute value of the differential gain, but it would also lead to a slow decay of vibration, and above a critical value, the amplitude may even increase.

The model proposed for conductor vibration control in this section is based on the geometrical, material and dynamic properties of a conductor with absorber. The model considers the nonlinear elastic behaviour of the conductor; and thereby, it is applicable to attenuate such high-amplitude vibrations as that following ice shedding from transmission line conductors. Simulation results demonstrate that the application of control can contribute to substantially reducing the first peak of vibration. The present research considered PD control where the application of proportional gain was particularly important for the reduction of conductor drop or rebound height. Differential gain may further decrease the first peak of vibration, but it also results in a slower decay. The model may further be improved by different aspects, which are subjects of future research.

- Control methodology may be improved by combining a PD control where the differential gain has a relatively great absolute value and a P control or vibration without control after the first few cycles in order not to slow down the decay.

- The control may further be improved by applying other control strategies that are more efficient for nonlinear vibrations.

- The time delay due to sampling influences the success of control; therefore, its consideration in the control is another significant direction of future research.

- Construction and testing of a prototype that can apply active vibration control under laboratory conditions is a further subject of future study.

These developments will also contribute to the attenuation of such high-amplitude vibrations that are maintained by excitation.

4.3 Dynamics of digitally controlled forced vibration of conductors with backlash

The effects of time delay on vibration control of a suspended conductor was already discussed in Section 4.1. When the control force is provided by a motor via mechanical driving, then backlash occurs at the driving of the motor. The control force is not transmitted in the domain of backlash each time when the motor changes the direction of rotation, as it is the case e.g. for gear pairs [118]. Backlash may lead to the fact that the equilibrium of the vibration system cannot be stable, but a periodic motion appears around this equilibrium. When a suspended cable is exposed to wind, then a periodic excitation acts on the corresponding vibration system, and a periodic motion develops around the equilibrium. The aim of the control in this case is to reduce the amplitude of that periodic motion. The influence of backlash in such vibration control was investigated in [88], where conclusions warned that successful control with backlash might require a driving system that can produce frequent changes in the direction of rotation.

Both of time delay and backlash influence the stability of vibration systems and result in limitation of the vibration control. Considering them together is a challenging problem in the modelling and in providing successful control as well. Apart from the combined limitations due to time delay and backlash, an irregular motion arises that was observed in delayed piecewise linear systems [78, 79]. The main goals of this section are (i) improving the model introduced in Section 4.1 by considering both of time delay due to sampling and backlash at the driving; (ii) providing the conditions for control that successfully reduces vibration amplitude when periodic excitation acts in such systems; and (iii) characterizing the resulting motions. Correspondingly, this section describes what is novelty in the mechanical model, and then focuses on the stability analysis of the controlled vibration system, and on the dynamics of resulting motions [63].

4.3.1 Mathematical model of controlled conductor vibration

The mathematical model is based on the 2DOF model presented in Section 4.1. That model is improved here in three aspects, of which the first two were considered in the model of Section 4.2 as well: (i) the location of the absorber is considered when the natural frequencies are prescribed for the calculation of the mass of reduced conductor and the spring stiffness of the absorber; (ii) the damping of the absorber is not neglected; (iii) backlash at the driving is taken into account. This section describes only modifications.

Control of forced conductor vibration with time delay

The mechanical model is shown in Figure 4.1. The calculation of the spring stiffness of the conductor k_1 is based on the statics of suspended cables [47], and explained in detail in Section 4.1.1. The mass of the absorber m_2 is based on its design. Then, the mass of the conductor m_1 and the spring stiffness of the absorber k_2 can be calculated together as was explained in Section 4.2.1. The damping coefficient of conductor c_1 is calculated from the Equation (4.26) where ω_1 is the natural circular frequency of the single DOF system that describes the conductor at the position where the vibration absorber would be placed. The damping coefficient c_2 and the excitation force $F(t)$ are determined as explained in Sections 4.2.1 and 4.1.1, respectively.

The control methodology is described in Section 4.1.1. The control force is determined by Equation (4.10) where the control parameter P is calculated from Equation (4.12). The vibration control works without the differential gain D, but its application makes the control more efficient in some cases by a faster reduction of the vibration amplitude.

Backlash at the driving

The PD control may be implemented using a DC motor and a set of mechanical driving units. Driving via gear wheel or teeth belt results in backlash that influences the control and the resulting motion. When the direction of rotation in the motor changes, the control force is not transmitted in the domain of backlash where the contact between the teeth ceases. Let the value of backlash be r_0, and assume that the relative displacement $\Delta z = z_2 - z_1$ is directly proportional to the angle of rotation of the DC motor. Two conditions are applied to imply that the system is in the domain of backlash.

- Condition 1: The angular velocity of the driving wheel of the motor is zero, which may be expressed using the relative velocity as follows

$$\dot{z}_2 - \dot{z}_1 = 0. \tag{4.31}$$

  It should be noted that this is an instantaneous equilibrium when the direction of rotation changes. Let Δz_{bl} denote the relative displacement in this time instance.

- Condition 2: The interval that describes the domain of backlash depends on the sign of relative velocity just before it became zero, and it can be expressed with the

relative displacement Δz_{bl} as follows

$$\Delta z_{bl} - r_0 \leq \Delta z \leq \Delta z_{bl} \tag{4.32}$$

if the relative velocity was previously positive; and

$$\Delta z_{bl} \leq \Delta z \leq \Delta z_{bl} + r_0 \tag{4.33}$$

if the relative velocity was previously negative.

The system is in the domain of backlash as long as the relevant condition (either (4.32) or (4.33)) is satisfied. When the system is outside the domain of backlash, then the computational process first verifies Condition 1. If it is not satisfied then the system is still not in the domain of backlash. If it is satisfied then Δz_{bl} is calculated, Condition 2 is verified, and the system is in the domain of backlash as long as this latter condition is satisfied. In this case, Condition 1 is not verified, because Δz_{bl} and the boundaries of the domain of backlash do not change even if the relative velocity changes its sign. If Condition 2 is not satisfied then the system is outside the domain of backlash, and Condition 1 has to be verified again.

Equations of motion

The governing equations of motion of the 2DOF model is given by Equation (4.13). The control force $u(t)$ can be organized in the following form considering backlash

$$u(t) = \begin{cases} \mathbf{D}\mathbf{z}(t-\tau) & \text{outside backlash} \\ 0 & \text{domain of backlash} \end{cases} \tag{4.34}$$

where $\mathbf{D}$ is given by Equation (4.11). The discrete-time model is described by Equations (4.14)-(4.16) with the exception that Equation (4.14) provides control force outside backlash only; otherwise it is equal to zero. Consequently, the control force in the discrete-time model is obtained as follows

$$u_{j+1} = \begin{cases} \mathbf{D}\mathbf{z}_j & \text{outside backlash} \\ 0 & \text{domain of backlash} \end{cases} \tag{4.35}$$

Alternatively, system (4.16) can be organized in the following form

$$\tilde{\mathbf{z}}_{j+1} = \begin{cases} \mathbf{S}\tilde{\mathbf{z}}_j + \tilde{\mathbf{c}}F_j & \text{outside backlash} \\ \mathbf{S}^*\tilde{\mathbf{z}}_j + \tilde{\mathbf{c}}F_j & \text{domain of backlash} \end{cases} \tag{4.36}$$

where $\tilde{\mathbf{z}}_j = \begin{bmatrix} \mathbf{z}_j \\ u_j \end{bmatrix}$, $\mathbf{S} = \begin{bmatrix} \mathbf{A_d} & \mathbf{b_d} \\ \mathbf{D} & 0 \end{bmatrix}$, $\mathbf{S}^* = \begin{bmatrix} \mathbf{A_d} & \mathbf{b_d} \\ \mathbf{0} & 0 \end{bmatrix}$ and $\tilde{\mathbf{c}} = \begin{bmatrix} \mathbf{c}_j \\ 0 \end{bmatrix}$.

Parameters of mechanical model	
Mass of cable, m_1 (kg)	0.0767
Spring stiffness of conductor, k_1 (N/m)	50.3
Damping coefficient of conductor, c_1 (Ns/m)	0.079
Mass of absorber, m_2 (kg)	0.16
Spring stiffness of absorber, k_2 (N/m)	74.4
Damping coefficient of absorber, c_2 (Ns/m)	4.0

Table 4.3: Parameters of the mechanical model with vibration absorber at one-tenth of the span

4.3.2 Parameter set-up and model validation

The mechanical model of the small-scale laboratory set-up of a transmission line described in [71] was constructed. The parameters of the conductor and span in the experimental set-up are listed in Table 4.1. However, parameters of the mechanical model are different due to the modified procedure to determine them. Details of calculation are provided in [63], and the parameters obtained are listed in Table 4.3.

The static behaviour of the model was validated by calculating displacements due to the application of concentrated forces and comparing them to the displacements obtained under the same conditions by the finite element model of [71]. This model was validated by measurements on the same experimental set-up that is modelled here. The displacement-force relationships coincided in the range of 0.1 N that was typical during small-amplitude vibrations of the set-up modelled. The discrepancy reached 10% when the force exceeded 0.4 N above or below the weight of absorber.

The dynamic behavior of the model was validated by simulating the vibration following the removal of concentrated forces and comparing the initial peaks in such vibration to those obtained by the finite element model. The discrepancy between the initial peaks obtained by the two models does not reach 10% as long as the removed force is smaller than 0.4 N. Further details of validation may be found in [63], which shows the reliability of the 2DOF model to simulate vibration at the position of absorber when small forces act.

4.3.3 Dynamics of controlled conductor motion with time delay and backlash

The stability analysis was carried out by following the methodology explained in Section 4.1.3; therefore, only a summary is provided here. Stability charts are similar to those of the same section; however, the present model takes the damping of the absorber into account; consequently, the size of the stability domain is significantly greater. The smallest amplitude of vibration for a given value of the proportional gain P may be achieved if the differential gain D in absolute value is significantly smaller than that at the boundary of stability domain. Kollár [63] suggested considering the sampling delay and the condition

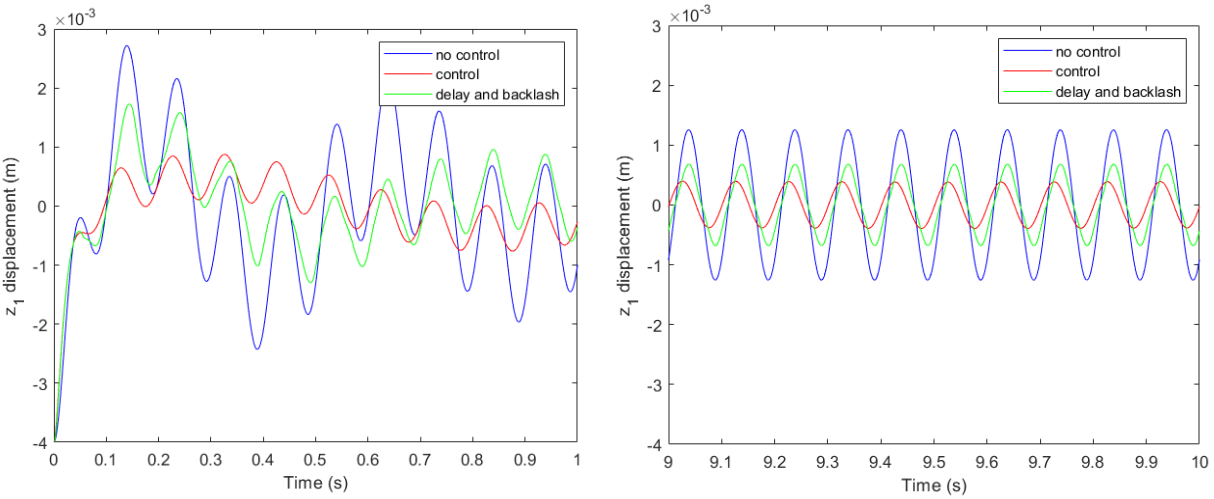

Figure 4.14: Time histories for excitation $F_0 = 0.5$ N, $f = 10$ Hz, control parameters $P = -557$ N/m and $D = -13$ Ns/m, sampling delay $\tau = 1$ ms, and backlash $r_0 = 0.5$ mm; (a) first second after initiating the vibration; (b) steady-state motion (9 s after initiating the vibration)

$b_0 = 0$ when choosing the differential gain.

The control force is not transmitted in the domain of backlash, which means that the amplitude of forced vibration cannot be reduced. In practice, the system passes the domain of backlash each time when the direction of motion changes. If the backlash is very small then its effects may be negligible. In the other extreme case, when the value of backlash is very high, the system behaves as if control was not applied. In between, the backlash influences the resulting motion what is discussed in the following.

Kollár et al. [78, 79] found irregular motion in digitally controlled piecewise linear systems where the control was applied in order to stabilize an unstable equilibrium. The motion was characterized to be more complicated than quasiperiodic, but it was not classified as chaotic since it did not satisfy all the conditions of chaos. The motion obtained in the present study also involves control with time delay and backlash that is described by a piecewise linear system, but the control is applied to attenuate the vibration caused by force excitation.

Assume that the amplitude and frequency of excitation is 0.5 N and 10 Hz, respectively; and the control parameters are chosen as $P = -557$ N/m and $D = -13$ Ns/m. Figure 4.14 shows a typical example for the time history of the displacement of mass m_1 that represents the simplified model of the conductor when the sampling delay is 1 ms and the value of backlash is 0.5 mm. According to Figure 4.14a, the highest peak above the equilibrium position is about four times greater without control (blue curve) than with control (red curve). However, if time delay and backlash are considered, then this reduction is significantly smaller, the peak in the controlled vibration (green curve) is approximately 63% of that without control. This ratio decreases to almost 50% if the amplitudes of the steady-state vibrations are compared (blue and green curves in Figure 4.14b). If the value of backlash is very high, then the entire motion occurs in the domain

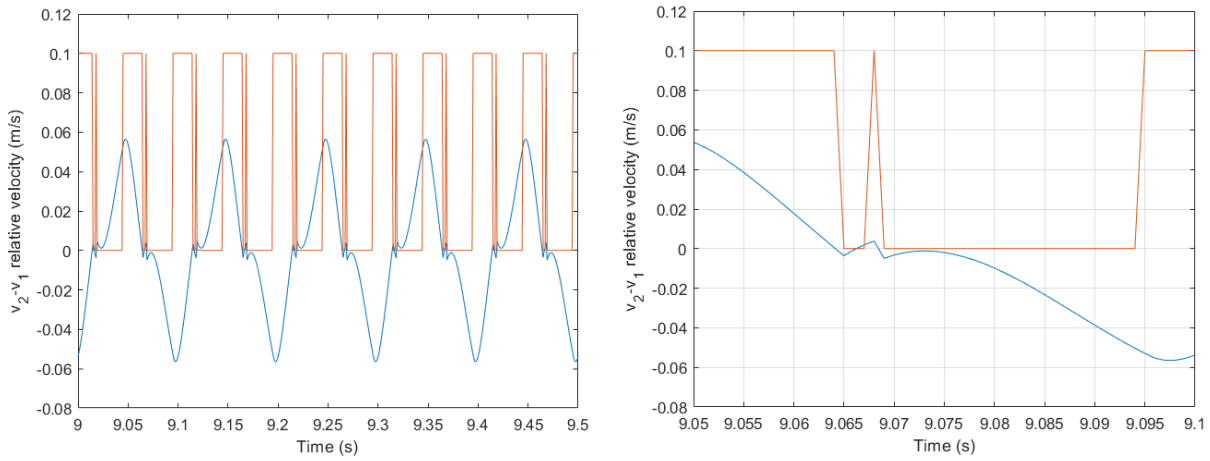

(a) (b)

Figure 4.15: Time history of relative velocity $\dot{z}_2 - \dot{z}_1$ (or $v_2 - v_1$) in the steady-state motion for excitation $F_0 = 0.5$ N, $f = 10$ Hz, control parameters $P = -557$ N/m and $D = -13$ Ns/m, sampling delay 1 ms, and backlash $r_0 = 0.5$ mm; blue curve: time history, red curve: 0 inside the domain of backlash and 0.1 outside the domain of backlash; (a) interval of 0.5 s; (b) interval of 0.05 s enlarged

of backlash, meaning that practically no control is applied. In this specific example, it would happen when the value of backlash reaches approximately 3 mm.

In order to identify the domain of backlash, the relative velocity $\dot{z}_2 - \dot{z}_1$ during the steady-state motion for sampling time of 1 ms and backlash of 0.5 mm is drawn by the blue curves in Figure 4.15. The motion enters the domain of backlash when this relative velocity reaches zero. The red curve is plotted only to visualize the domain of backlash, but the values on the curve have no physical meaning. It shows a value of zero in the domain of backlash, whereas the value is 0.1 outside the domain of backlash. An interval of 0.05 s is enlarged in Figure 4.15b, which helps analyze the motion. The relative velocity was positive and changes its sign at 9.065 s. However, it remains negative for two time steps only (i.e. 0.002 s), because it increases. This may be explained by the effects of the spring between masses m_1 and m_2. After one more time step, i.e. at 9.068 s, the system leaves the domain of backlash via its upper boundary; therefore, the control force acts again. The relative velocity becomes negative in one time step (at 9.069 s) due to the application of the control force; therefore, the system enters to the domain of backlash and the control force is not transmitted again. Consequently, the relative velocity slightly increases again; however, now it does not reach zero, but it becomes decreasing after 9.073 s. The system reaches the other, i.e. the lower, boundary of the domain of backlash at 9.095 s, and then the control force acts again.

Three cases of the example considered will be examined in the following for different values of sampling delay and backlash. These cases are named Case A that was the subject of the above discussion: $\tau = 1$ ms; $r_0 = 0.5$ mm; Case B: $\tau = 1$ ms; $r_0 = 2$ mm; and Case C: $\tau = 11$ ms; $r_0 = 2$ mm. Phase diagrams showing the trajectories on the $\dot{z}_1 - z_1$ plane in the steady-state motion are drawn in Figure 4.16. Figure 4.16a is

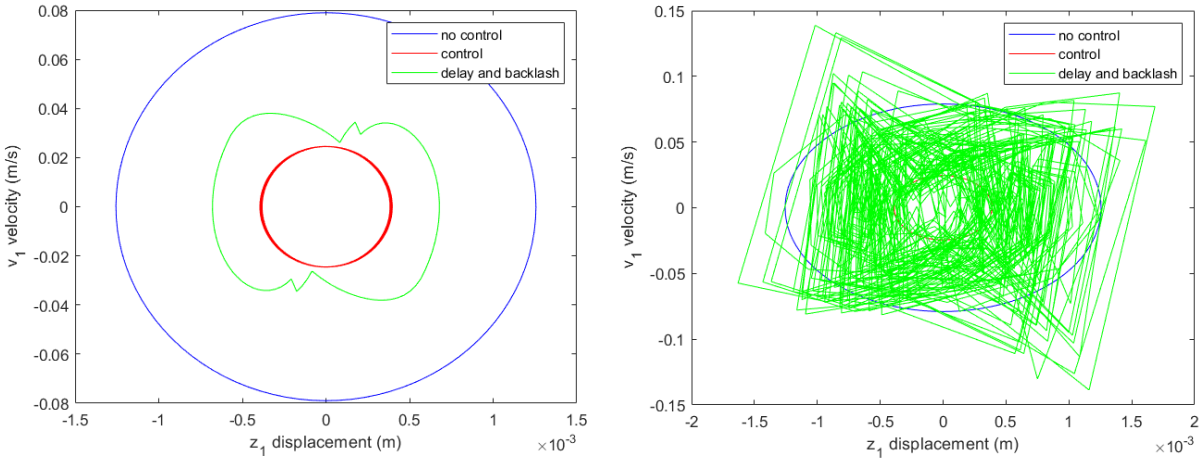

Figure 4.16: Phase diagrams during steady-state motion for excitation $F_0 = 0.5$ N, $f = 10$ Hz, control parameters $P = -557$ N/m and $D = -13$ Ns/m; (a) Case A; (b) Case C

drawn for Case A, and it clearly shows the periodic solutions obtained. The limit cycle is significantly smaller with the application of control (cf. the blue and red curves), and the green curve is obtained in between, which represents the case of control with time delay and backlash considered. If the value of backlash is increased (as in Case B), then the size of limit cycle increases and more frequency components dominate in the motion. Irregularity is observed in the motion when the sampling time increased to 11 ms (Case C). The phase diagram of this motion is shown by the green curve in Figure 4.16b.

The behaviour of the motions described above looks periodic; however, the irregularity observed requires further investigation of the characteristics of the motions. Although chaos has no uniformly accepted definition, chaotic motions are characterized by an attractive set, sensitive dependence on initial conditions, topological transitivity, and at least one positive Lyapunov exponent [4, 28, 91, 128]. The attractive set exists in case of the motions described above, and the other characteristics are examined by applying the fast Fourier transform (FFT), studying the behaviour of trajectories, and calculating the Lyapunov exponents numerically. The prevailing frequency of vibration can clearly be distinguished in the Fourier spectrum when the sampling delay is 1 ms (Cases A and B). This frequency is 10 Hz that corresponds to the excitation frequency. When the sampling delay is 11 ms (Case C), then the highest peak still occurs at 10 Hz; however, many other small peaks appear in the Fourier spectrum. These observations suggest that the motions are periodic or quasiperiodic, but further investigation is recommended in Case C.

The sensitive dependence on initial conditions may be revealed by the deviation between nearby trajectories. If the trajectories initially are close enough to each other, then nearby trajectories approach each other in most of the cases. This property is observed even in Case C when the irregularity was noticed in the phase plane. However, for Case B when the sampling time is 1 ms, then nearby trajectories neither approach nor stretch each other even though the motion was characterized as periodic.

Occurrence of a trajectory in any small domain inside the attractive set during the

Lyapunov exponents	Case B	Case C
λ_1	-0.0010	-0.0140
λ_2	-0.0014	-0.0148
λ_3	-0.0476	-0.1855
λ_4	-0.0497	-0.4789
λ_5	-33.26	-29.23

Table 4.4: Lyapunov exponents obtained for Cases B and C

motion may refer to topological transitivity. Simulation time is varied for Case C and small parts of the phase plane in Figure 4.16b are compared. The trajectory occurs in a significantly greater part of the domain considered when simulation time increases from 10 to 100 s. However, further increasing simulation time from 100 to 1000 s does not mean that trajectories would become denser in this domain. Consequently, these numerical results suggest that the condition of topological transitivity is not satisfied.

The Lyapunov exponents are calculated numerically by applying the following algorithm [4]. First, choose an initial orthogonal basis $\{\mathbf{w}_1^0, \ldots, \mathbf{w}_5^0\}$. Then, compute the vectors $\{\mathbf{v}_1^1, \ldots, \mathbf{v}_5^1\}$ by multiplying the basis by the matrix $\mathbf{S}$ or $\mathbf{S}^*$ defined in (4.36) at the initial condition. Use the Gram-Schmidt orthogonalization to obtain a new orthogonal basis $\{\bar{\mathbf{w}}_1^1, \ldots, \bar{\mathbf{w}}_5^1\}$. Normalize these vectors in order to eliminate the problem of extremely large and small numbers to get the orthogonal basis of the next step $\{\mathbf{w}_1^1, \ldots, \mathbf{w}_5^1\}$. Repeating these steps n times, the Lyapunov exponents may be estimated as follows

$$\lambda_i = \frac{\ln \|\bar{\mathbf{w}}_i^n\| + \ldots + \ln \|\bar{\mathbf{w}}_i^1\|}{n}, \quad i = 1, \ldots, 5 \tag{4.37}$$

Lyapunov exponents are calculated in each time step for Cases B and C, and the values obtained with at least 1% accuracy are listed in Table 4.4. The Lyapunov exponents that are not significantly smaller than zero are shown in Figure 4.17. Results clearly show that all the Lyapunov exponents are less than one. Thus, the Lyapunov exponents confirm the findings of the previous analysis. Although motions that seem irregular may arise in the system studied, but those motions are not chaotic.

The active control of conductor vibration proposed in Section 4.1 was successfully improved. The stability analysis revealed that the stability domain on the plane of control parameters may significantly shrink with increasing time delay that occurs due to sampling in the digital control. When backlash is also present at the driving, then irregularity was observed in the motion depending on the value of backlash. However, the motion was characterized periodic or quasiperiodic according to the numerical study. Although nearby trajectories do not approach each other in some cases, but they do not stretch each other either. Orbits are not dense, and the condition of topological transitivity is not satisfied. Furthermore, all the Lyapunov exponents are less than zero. The irregular motion that was obtained in digitally controlled unstable systems with backlash and that was characterized more complicated that quasiperiodic, but not chaotic [79], was not observed in the present study. It may be concluded that digitally controlled forced

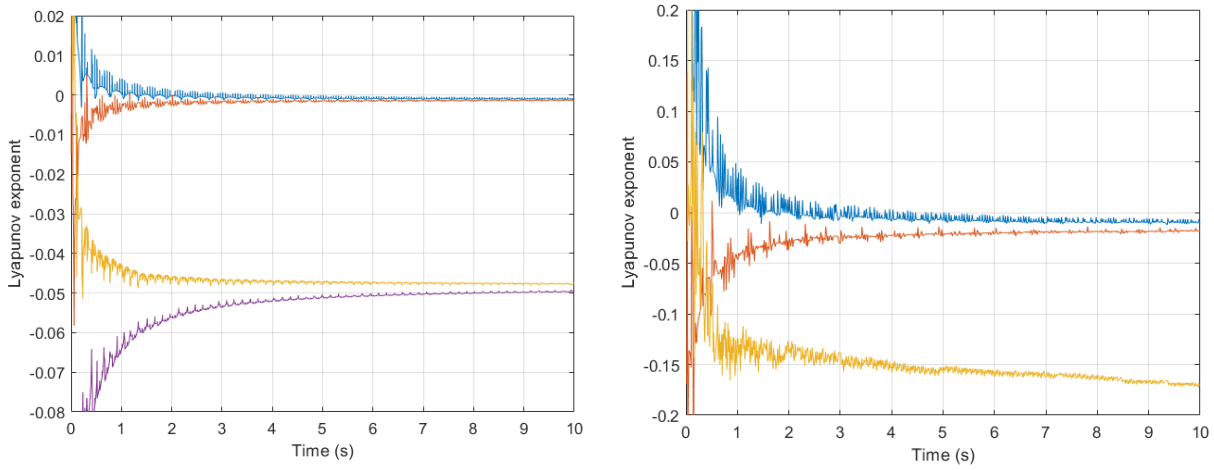

(a) (b)

Figure 4.17: The largest Lyapunov exponents as calculated in the first 10 s for excitation $F_0 = 0.5$ N, $f = 10$ Hz, control parameters $P = -557$ N/m and $D = -13$ Ns/m; (a) Case B; (b) Case C

vibration in piecewise linear systems results in periodic or quasiperiodic motions with the irregularities described in this section. From the practical point of view, unpredictable motion is not expected if control parameters, sampling time and value of backlash are properly chosen. However, sampling delay and backlash result in limitations in the control. Sampling delay should be small enough for successful control, i.e. in the range of 10 ms when the excitation frequency is around 10 Hz, what reduces below 1 ms when the excitation frequency exceeds 50 Hz. The presence of backlash may require quick changes (i.e. in the range of few ms) in the direction of rotation of the driving motor. Backlash does not have great influence on the motion when it is in the range of 0.1 mm or smaller; however, irregularities in the motion occur if the value of backlash is in the range of 1 mm.

4.4 New results

Main contribution 5 *An active control methodology was proposed that successfully attenuates vibration of conductors at the location where the control is applied. The model developed has two degrees of freedom and consists of the conductor simplified at the specified location with a controlled vibration absorber. The theory of statics and dynamics of suspended cables provides the basics to determine model parameters. They are calculated from the geometrical and material properties of the conductor and the span, whereas the characteristics of vibration observed in related finite element modelling and experimental tests were also applied in the calculation of damping coefficient. The approach considers wind effect as a periodic excitation. The model involves time delay that is always present in digital control due to sampling effect. The above described control method successfully reduces the initial peak and the amplitude of high-frequency, low-amplitude vibration that characterizes a type of wind-induced conductor motion, the so-called aeolian vibration.*

The amplitude of such vibration is comparable to the conductor diameter, whereas its frequency is in the range of few Hz to several 10 Hz. Time delay in the digital control results in a limitation, since the sampling time should be reduced below the range of 1 ms when the excitation frequency exceeds 50 Hz.

The approach was further improved by considering the nonlinear elastic material behaviour of the conductor. Thereby, the vibration control may successfully attenuate even high-amplitude conductor vibration. The model was applied for a typical case when vibration followed ice shedding from a transmission line conductor. Such vibration is characterized by a high conductor rebound height (i.e. in the range of several m in case of a transmission line with span length of several hundred m) followed by a decaying oscillation. Simulation results demonstrated that the application of control could contribute to substantially reducing the first peak of vibration. For the full-scale transmission line modelled, the first peak is reduced to about two-third of its value without control, and to about half of its value without damper.

Related publications: Kollár (2021) [61], Kollár (2022) [62]

Main contribution 6 *Irregular motion may arise in digitally controlled piecewise linear systems. The active control of conductor vibration is described by such system if sampling delay is considered together with backlash at the driving. The motion observed exhibited irregularities for some parameter values; however, it was characterized periodic or quasiperiodic based on the following results. Although nearby trajectories do not approach each other in some cases, but they do not stretch each other either. Orbits are not dense, and the condition of topological transitivity is not satisfied. Furthermore, all the Lyapunov exponents are less than zero. From the practical point of view, unpredictable motion is not expected if control parameters, sampling time and the value of backlash are properly chosen. However, sampling delay and backlash result in limitations in the control. Sampling delay should be small enough for successful control as was stated in Thesis 5. The presence of backlash may require quick changes (i.e. in the range of few ms) in the direction of rotation of the driving motor. Backlash does not have great influence on the motion when it is in the range of 0.1 mm or smaller; however, irregularities in the motion occur if the value of backlash is in the range of 1 mm.*

Related publication: Kollár (2023) [63]

Chapter 5

Summary

The research presented in this dissertation aimed to study the three areas related to the vibration of transmission line conductors and to the development of solutions to reduce the harmful effects of such vibrations. These topics include the characteristics of droplet clouds that determine the process of ice accretion, the natural phenomena that lead to conductor vibration, and the methods that are developed in order to attenuate the vibration. The goals and the methodology were formulated in Chapter 1.

Theoretical and experimental models were developed to study droplet clouds that are responsible for atmospheric icing and to simulate their variation in the flow before reaching the icing object. The theoretical model considered the following processes that influence droplet cloud characteristics: (i) binary droplet collision, (ii) droplet evaporation and cooling, (iii) gravitational settling of droplets, and (iv) turbulent dispersion of droplets. Particular attention was paid to droplet collision. Collision outcome maps include the possible outcomes of droplet collisions, and criteria for most of the transitions between the regimes were already proposed in the relevant literature. Two common outcomes in the process that simulates the evolution of the clouds in atmospheric icing is the coalescence after minor deformation and bounce. The boundary between these regimes has been observed previously in experimental studies with no criterion proposed yet. The theoretical background of the criterion for this transition was developed here. The application of the composite collision outcome model involving this criterion contributed to explaining the effects of ambient parameters on the characteristics of droplet clouds. Results revealed the streamwise and vertical variations of droplet size distribution and liquid water content of the cloud, which are among the decisive factors influencing atmospheric icing processes. The related developments and results are summarized in Theses 1 and 2.

Transmission line conductors are exposed to such natural phenomena as wind, ice or impact from external sources. Wind or ice shedding may lead to high-frequency or high-amplitude vibrations that may damage some elements of the transmission line. These phenomena have been examined theoretically, numerically and experimentally in former research. The main contribution of the present research is the development of a modelling approach that simulates vibration of conductor bundles following ice shedding from a subconductor. Spacer model was proposed and the approach revealed their effects on the

vibration. The number of spacers and their location along the span influence the maximum jump height of the ice-shedding conductor, the maximum drop of the loaded conductor, the bundle rotation and the conductor tension. Consequently, properly chosen spacer arrangement contributes to reducing the severity of vibration following ice shedding. The modelling approach was adapted for several ice shedding processes, including (i) propagation of ice shedding along the length of the span, (ii) propagation of ice shedding along the length of the span plus an additional downward pull induced at discrete locations along the span by the detachment of ice chunks, and (iii) sudden and simultaneous ice shedding from the whole span or part of the span. Interphase spacers were also considered in the model, which contribute to preventing the reduction of conductor clearance and the risk of flashover during high-amplitude vibration. These results are formulated in Theses 3 and 4.

Line protection methods that help reduce the harmful effects of vibration have been applied for decades. The present research proposes an active control methodology that can be applied at any specific position along the span. The model considers a simplified conductor with a vibration absorber. The application of control successfully attenuates high-frequency, low-amplitude conductor vibration at the location where the absorber is placed. Time delay that is always present in digital control due to sampling results in a limitation, since control remains successful only for small enough sampling delay for high excitation frequencies. An improved model considers the nonlinear elastic material behaviour of the conductor, which makes the control successfully attenuate even such high-amplitude vibration as that following ice shedding from the conductor. Backlash at the driving means a further limitation in the control, since it may require quick changes in the direction of rotation of the driving motor. The presence of time delay together with backlash in the control of forced vibration may result in an irregular motion. However, this motion was characterized periodic or quasiperiodic based on a detailed dynamic analysis. These achievements are written in Theses 5 and 6.

Bibliography

[1] M. H. Abbasi and H. Moradi. Optimum design of tuned mass damper via pso algorithm for the passive control of forced oscillations in power transmission lines. *SN Appl Sci*, 2:1–15, 2020.

[2] Y. Achkire. *Active Tendon Control of Cable-Stayed Bridges*. PhD dissertation, Active Structures Laboratory, Université libre de Bruxelles, 1997.

[3] ADINA. *Theory and Modeling Guide*. ADINA, Watertown, MA, 2010.

[4] K. T. Alligood, T. D. Sauer, and J. A. Yorke. *Chaos. An introduction to dynamical systems*. Springer-Verlag, New York, NY, 1996.

[5] K. Anderson and P. Hagedorn. On the energy dissipation in spacer dampers in bundled conductors of overhead transmission lines. *Journal of Sound and Vibration*, 180(4):539–556, 1995.

[6] N. Ashgriz and J. Y. Poo. Coalescence and separation in binary collisions of liquid drops. *Journal of Fluid Mechanics*, 221:183–204, 1990.

[7] ASTM. Standard test methods and definitions for mechanical testing of steel products. In *ASTM A-370. Annual Book of ASTM Standards, Section One: Iron and Steel Products*, volume 01.03, pages 102–150, West Conshohocken, PA: Infinity Publishing Co., 2004.

[8] O. Barry, D. C. D. Oguamanam, and D. C. Lin. Aeolian vibration of a single conductor with a stockbridge damper. *Proceedings of the Institution of Mechanical Engineering, Part C: Journal of Mechanical Engineering Science*, 227(5):935–945, 2012.

[9] K. J. Bathe. *Finite Element Procedures*. Prentice Hall, Upper Saddle River, NJ, USA, 1996.

[10] K. V. Beard and H. R. Pruppacher. A wind tunnel investigation of the rate of evaporation of small water drops falling at terminal velocity in air. *Journal of Atmospheric Sciences*, 28:1455–1464, 1971.

[11] P. R. Brazier-Smith, S. G. Jennings, and J. Latham. The interaction of falling water droplets: coalescence. *Proc. Royal. Soc. London A*, 326:393–408, 1972.

[12] B. Chen, W. Guo, P. Li, and W. Xie. Dynamic responses and vibration control of the transmission tower-line system: a state-of-the-art review. *Sci World J*, Article ID 538457:1–20, 2014.

[13] J.-D. Chen, P. S. Hahn, and J. C. Slattery. Coalescence time for a small drop or bubble at a fluid-fluid interface. *AIChE Journal*, 30(4):622–630, 1984.

[14] CIGRE. *SCB2 WG11. State of the Art Survey on Spacers and Spacer Dampers.* Electra No. 277, 2005.

[15] S. G. Cober, G. A. Isaac, and J. W. Strapp. Characterization of aircraft icing environments that include supercooled large drops. *J. Appl. Meteorol.*, 40:1984–2002, 2001.

[16] K. L. Cooke and J. Turi. Stability, instability in delay equations modeling human respiration. *J. Math. Biol.*, 32:535–543, 1994.

[17] P. Creismeas. A Eulerian/Lagrangian model to calculate the evolution of a water droplet spray. *International Journal for Numerical Methods in Fluids*, 20(2):135–155, 1995.

[18] C. T. Crowe, M. P. Sharma, and D. E. Stock. The particle-source-in cell (psi-cell) model for gas-droplet flows. *Journal of Fluids Engineering*, pages 325–332, 1977.

[19] J. P. Den Hartog. Transmission line vibration due to sleet. *AIEE Transactions*, 51:1074–1076, 1932.

[20] J. Druez, S. Louchez, and P. McComber. Ice shedding from cables. *Cold Regions Science and Technology*, 23:377–388, 1995.

[21] N. Du. *Études des méthodes par impact et a l'huile utilisées pour déterminer le diametre des gouttelettes dans les brouillard naturels et artificiels.* MSc thesis, University of Québec at Chicoutimi, Chicoutimi, QC, Canada, 1987.

[22] J. K. Dukowicz. A particle-fluid numerical model for liquid sprays. *Journal of Computational Physics*, 35:229–253, 1980.

[23] J. B. Edson, S. Anquetin, P. G. Mestayer, and J. F. Sini. Spray droplet modeling 2. An interactive Eulerian-Lagrangian model of evaporating spray droplets. *Journal of Geophysical Research*, 101(C1):1279–1293, 1996.

[24] A. T. Edwards and J. M. Boyd. Bundle-conductor-spacer design requirements and development of 'spacer-vibration-damper'. *IEEE Transactions on Power Apparatus and Systems*, PAS-84(10):924–932, 1965.

[25] EPRI. *Transmission Line Reference Book: Wind-Induced Conductor Motion.* Electric Power Research Institute, Palo Alto, CA, 1979.

[26] EPRI. *Transmission Line Reference Book: Wind-Induced Conductor Motion*. Electric Power Research Institute, Palo Alto, CA, 2005.

[27] J.-P. Estrade, H. Carentz, G. Lavergne, and Y. Biscos. Experimental investigation of dynamic binary collision of ethanol droplets - a model for droplet coalescence and bouncing. *International Journal of Heat and Fluid Flow*, 20:486–491, 1999.

[28] M. Farkas. *Periodic motions*. Springer, New York, NY, 1994.

[29] M. Farzaneh. *Atmospheric icing of power networks*. Springer, Berlin, Germany, 2008.

[30] Y. Fujino, K. Kimura, and H. Tanaka. *Wind resistant design of bridges in Japan: developments and practices*. Springer, 2012.

[31] S. Gao, C. Zeng, L. Zhou, X. Liu, and B. Gao. Numerical analysis of the dynamic effects of wine-cup shape power transmission tower-line system under ice-shedding. *Structures*, 24:1–12, 2020.

[32] E. M. Gates, W. Lam, and E. P. Lozowski. Spray evolution in icing wind tunnels. *Cold Regions Science and Technology*, 15:65–74, 1988.

[33] M. Gavaises, A. Theodorakakos, G. Bergeles, and G. Brenn. Evaluation of the effect of droplet collisions on spray mixing. *Proc. Inst. Mech. Eng.*, 210:465–475, 1996.

[34] B. Godard. A vibration-sag-tension-based icing monitoring of overhead lines. In *Proc. 18th Int. Workshop on Atmospheric Icing of Structures*, page Paper 4, Reykjavik, Iceland, 2019.

[35] S. Godard. Mesure de gouttelettes de nuage avec un film de collargol. *Bulletin de l'Observatoire du Puy de Dome*, pages 41–46, 1960.

[36] R. A. Gore and C. T. Crowe. Effect of particle size on modulating turbulent intensity. *Int. J. of Multiphase Flow*, 15:279–285, 1989.

[37] A. D. Gosman and E. Ioannides. Aspects of computer simulation of liquid-fuelled combustors. *AIAA Paper*, 1981-323, 1981.

[38] P. Hagedorn, N. Mitra, and T. Hadulla. Vortex-excited vibrations in bundled conductors: A mathematical model. *Journal of Fluids and Structures*, 16(7):843–854, 2002.

[39] C. Hardy and P. Bourdon. The influence of spacer dynamic properties in the control of bundle conductor motion. *IEEE Transactions on Power Apparatus and Systems*, PAS-99(2):790–799, 1980.

[40] C. Hardy and P. Van Dyke. Field observations on wind-induced conductor motions. *Journal of Fluids and Structures*, 9:43–60, 1995.

[41] D. G. Havard and P. Van Dyke. Effects of ice on the dynamics of overhead lines. Part II: Field data on conductor galloping, ice shedding and bundle rolling. In *Proc. 11th Int. Workshop Atmospheric Icing Structures*, pages 291–296, Montreal, QC, Canada, 2005.

[42] G. Hetsroni. Particles-turbulence interaction. *Int. J. of Multiphase Flow*, 15:735–746, 1989.

[43] G. Huang, B. Yan, N. Wen, C. Wu, and Q. Li. Study on jump height of transmission lines after ice-shedding by reduced scale modeling test. *Cold Reg. Sci. Technol.*, 165:102781, 2019.

[44] R. F. Ide. *Liquid water content and droplet size calibration of the NASA LEWIS Icing Research Tunnel*. NASA TM-102447, 1990.

[45] R. F. Ide and J. R. Oldenburg. *Icing cloud calibration of the NASA Glenn Icing Research Tunnel*. NASA/TM-2001-210689, 2001.

[46] T. Insperger and G. Stépán. *Semi-discretization for time-delay systems: stability and engineeing applications*. Springer, New York, NY, 2011.

[47] H. M. Irvine. *Cable Structures*. MIT Press, Cambridge, MA, 1981.

[48] H. M. Irvine and T. K. Caughey. The linear theory of free vibrations of a suspended cable. *Proceedings of the Royal Society London A*, 341:299–315, 1974.

[49] A. Jamaleddine, G. McClure, J. Rousselet, and R. Beauchemin. Simulation of ice shedding on electrical transmission lines using ADINA. *Comput. Structures*, 47(4/5):523–536, 1993.

[50] R. K. Jeck. *Representative Values of Icing-Related Variables Aloft in Freezing Rain and Freezing Drizzle*. DOT/FAA/AR-TN95/119, 1996.

[51] R. K. Jeck. *Icing-Design Envelopes (14 CFR Parts 25 and 29, Appendix C) Converted to a Distance-Based Format*. DOT/FAA/AR-00/30, 2002.

[52] S. A. K. Jeelani and S. Hartland. Effect of surface mobility on collision of spherical drops. *Journal of Colloid and Interface Science*, 206:83–93, 1998.

[53] K. Ji, X. Rui, L. Li, A. Leblond, and G. McClure. A novel ice-shedding model for overhead power line conductors with the consideration of adhesive/cohesive forces. *Comput. Struct.*, 157:153–164, 2015.

[54] T. Kálmán, M. Farzaneh, and G. McClure. Numerical analysis of the dynamic effects of shock-load-induced ice shedding on overhead ground wires. *Comput. Struct.*, 85:375–384, 2007.

[55] T. Kálmán, G. McClure, M. Farzaneh, and L. E. Kollár. Dynamic behavior of iced overhead cables subjected to mechanical shocks. In *Proc. 6th Int. Symp. Cable Dynamics*, pages 339–346, Charleston, SC, USA, 2005.

[56] S. G. Kelly. *Mechanical vibrations: theory and applications.* Cengage Learning, Stamford, CT, USA, 2011.

[57] L. Kempner Jr. *Longitudinal impact loading on electrical transmission line towers — A scale model study.* PhD dissertation, Portland State Univ., Portland, OR, 1997.

[58] S. Kim, D. J. Lee, and C. S. Lee. Modeling of binary droplet collisions for application to inter-impingement sprays. *Int. J. of Multiphase Flow*, 35:533–549, 2009.

[59] G. H. Ko and H. S. Ryou. Droplet collision processes in an inter-spray impingement system. *Aerosol Science*, 36:1300–1321, 2005.

[60] L. E. Kollár. *Dynamics of Digitally Controlled Unstable Mechanical Systems.* PhD dissertation, Department of Applied Mechanics, Budapest University of Technology and Economics, 2001.

[61] L. E. Kollár. Digital control of cable vibration with time delay. *International Journal of Dynamics and Control*, 9:1223–1235, 2021.

[62] L. E. Kollár. Ice-shedding-induced vibration of conductors with active vibration control. *Cold Regions Science and Technology*, 196:103504, 2022.

[63] L. E. Kollár. Dynamics of digitally controlled forced vibration of suspended cables. *Meccanica*, 58:25–42, 2023.

[64] L. E. Kollár and M. Farzaneh. Dynamic analysis of overhead cable vibrations as a result of ice shedding. In *Proc. 6th Int. Symp. Cable Dynamics*, pages 427–434, Charleston, SC, USA, 2005.

[65] L. E. Kollár and M. Farzaneh. Dynamic behavior of cable systems with spacers following ice shedding. In *Proc. ICNPAA 2006: Mathematical Problems in Engineering and Aerospace Sciences*, Budapest, Hungary, 2006.

[66] L. E. Kollár and M. Farzaneh. Modeling the evolution of droplet size distribution in two-phase flows. *Int. J. of Multiphase Flow*, 33(11):1255–1270, 2007.

[67] L. E. Kollár and M. Farzaneh. Vibration of bundled conductors following ice shedding. *IEEE Transactions on Power Delivery*, 23(2):1097–1104, 2008.

[68] L. E. Kollár and M. Farzaneh. Modeling the dynamic effects of ice shedding on spacer dampers. *Cold Regions Sci. Technol.*, 57:91–98, 2009.

[69] L. E. Kollár and M. Farzaneh. Spray characteristics of artificial aerosol clouds in a low-speed icing wind tunnel. *Atomization and Sprays*, 19(4):389–407, 2009.

[70] L. E. Kollár and M. Farzaneh. *Modeling and Experimental Study of Variation of Droplet Cloud Characteristics in a Low-Speed Horizontal Icing Wind Tunnel*, pages 93–127. Nova Science Publishers, Inc., Hauppauge, NY, 2011.

[71] L. E. Kollár and M. Farzaneh. Modeling sudden ice shedding from conductor bundles. *IEEE Transactions on Power Delivery*, 28(2):604–611, 2013.

[72] L. E. Kollár, M. Farzaneh, and A. R. Karev. Modeling droplet collision and coalescence in an icing wind tunnel and the influence of these processes on droplet size distribution. *Int. J. of Multiphase Flow*, 31(1):69–92, 2005.

[73] L. E. Kollár, M. Farzaneh, and A. R. Karev. The role of droplet collision, evaporation and gravitational settling in the modeling of two-phase flows under icing conditions. In *Proc. 11th International Workshop on Atmospheric Icing of Structures*, page Paper IW38, Montreal, QC, Canada, 2005.

[74] L. E. Kollár, M. Farzaneh, and A. R. Karev. Modeling droplet size distribution near a nozzle outlet in an icing wind tunnel. *Atomization and Sprays*, 16(6):673–686, 2006.

[75] L. E. Kollár, M. Farzaneh, and P. Van Dyke. Modeling of cable vibration following ice shedding propagation. In *Proc. 14th Int. Workshop Atmospheric Icing Structures*, Chongqing, China, 2011.

[76] L. E. Kollár, M. Farzaneh, and P. Van Dyke. Modeling ice shedding propagation on transmission lines with or without interphase spacers. *IEEE Transactions on Power Delivery*, 28(1):261–267, 2013.

[77] L. E. Kollár, G. Stépán, and S. J. Hogan. Sampling delay and backlash in balancing systems. *Periodica Polytechnica Ser. Mech. Eng.*, 44(1):77–84, 2000.

[78] L. E. Kollár, G. Stépán, and J. Turi. Dynamics of delayed piecewise linear systems. *Electronic Journal of Differential Equations*, Conference 10:163–185, 2003.

[79] L. E. Kollár, G. Stépán, and J. Turi. Dynamics of piecewise linear discontinuous maps. *International Journal of Bifurcation and Chaos*, 14(7):2341–2351, 2004.

[80] L. E. Kollár and M. Farzaneh. The effects of droplet collision, evaporation, gravity and turbulent dispersion on the droplet size distribution of an aerosol cloud under icing conditions. In *Proc. 12th International Workshop on Atmospheric Icing of Structures*, pages Paper 2–3, Yokohama, Japan, 2007.

[81] M. Lapointe. *Dynamic analysis of a power line subjected to longitudinal loads*. MSc thesis, Department of Civil Engineering and Applied Mechanics, McGill University, Montreal, QC, Canada, 2003.

[82] J. Li, B. Wang, J. Sun, S. Wang, X. Zhang, and X. Fu. Collapse analysis of a transmission tower-line system induced by ice shedding. *Front. Phys.*, 9:712161, 2021.

[83] G. D. M. MacKay and S. G. Mason. The gravity approach and coalescence of fluid drops at liquid interfaces. *The Canadian Journal of Chemical Engineering*, 41:203–212, 1963.

[84] J. Marek and W. A. Olsen Jr. Turbulent dispersion of the icing cloud from spray nozzles used in icing tunnels. In *Proc. 3rd Int. Workshop on Atmospheric Icing of Structures*, Vancouver, BC, Canada, 1986.

[85] Y. Matsubayashi. Theoretical considerations of the twisting phenomenon of the bundle conductor type transmission line. *Sumimoto Elect. Tech. Rev.*, 1:9–21, 1963.

[86] M. R. Maxey and J. J. Riley. Equation of motion for a small rigid sphere in a nonuniform flow. *Physics of Fluids*, 26:883–889, 1983.

[87] Y. Meng and L. E. Kollár. Proposed active control methodologies for aeolian vibration of suspended cables under icing conditions. In *Proc. 18th Int. Workshop on Atmospheric Icing of Structures*, page Paper 30, Reykjavik, Iceland, 2019.

[88] Y. Meng and L. E. Kollár. Dynamic analysis of electrical vibration absorbers for suspended cables. *Proceedings of the Institution of Mechanical Engineers, Part C: Journal of Mechanical Engineering Science*, 235(24):7445–7455, 2021.

[89] V. T. Morgan and D. A. Swift. Jump height of overhead-line conductors after the sudden release of ice loads. *Proc. Inst. Elect. Eng.*, 111(10):1736–1746, 1964.

[90] A. Munnannur and R. D. Reitz. A new predictive model for fragmanting and non-fragmanting binary droplet collisions. *Int. J. of Multiphase Flow*, 33:873–896, 2007.

[91] A. H. Nayfeh and B. Balachandran. *Applied nonlinear dynamics*. Wiley, New York, NY, 1995.

[92] A. V. Nguyen and H. J. Schulze. *Colloidal Science of Flotation*. Marcel Dekker, Inc., New York, NY, 2004.

[93] O. Nigol, G. J. Clarke, and D. G. Havard. Torsional stability of bundle conductors. *IEEE Trans. Power App. Syst.*, PAS-96(5):1666–1674, 1977.

[94] N. Nikolopoulos, K. S. Nikas, and G. Bergeles. A numerical investigation of central binary collision of droplets. *Computers and Fluids*, 38:1191–1202, 2009.

[95] C. Norberg. Fluctuating lift on a circular cylinder: review and new measurements. *J. Fluids Struct.*, 17:57–96, 2003.

[96] N. Olgac and B. T. Holm-Hansen. A novel active vibration absorption technique: delayed resonator. *Journal of Sound and Vibration*, 176(2):93–104, 1994.

[97] N. Olgac and B. T. Holm-Hansen. Tunable active vibration absorber: the delayed resonator. *J. Dyn. Syst. Meas. Control*, 117:513–519, 1995.

[98] M. Orme. Experiments on droplet collisions, bounce, coalescence and disruption. *Prog. Energy Combust. Sci.*, 23:65–79, 1997.

[99] P. J. O'Rourke and F. V. Bracco. Modelling of drop interactions in thick sprays and a comparison with experiments. *Proc. Inst. Mech. Eng.*, 9:101–116, 1980.

[100] W. J. Palm. *Modeling, analysis, and control of dynamic systems.* Wiley, Danvers, 2000.

[101] A. B. Peabody and G. McClure. Modeling the overhead power line post spring-damper using adina. In *Proc. 3rd MIT Conference on Computational Fluid and Solid Mechanics*, Cambridge, MA, USA, 2005.

[102] S. L. Post and J. Abraham. Modeling the outcome of drop-drop collisions in diesel sprays. *Int. J. of Multiphase Flow*, 28:997–1019, 2002.

[103] H. R. Pruppacher and J. D. Klett. *Microphysics of Clouds and Precipitation.* D. Reidel Publishing Company, Dordrecht, Holland, 1978.

[104] J. Qian and C. K. Law. Regimes of coalescence and separation in droplet collision. *Journal of Fluid Mechanics*, 331:59–80, 1997.

[105] M. Roberge. *A study of wet snow shedding from an overhead cable.* M.Eng. thesis, McGill Univ., Montreal, QC, Canada, 2006.

[106] M. Roshan Fekr and G. McClure. Numerical modelling of the dynamic response of ice shedding on electrical transmission lines. *Atmospher. Res.*, 46:1–11, 1998.

[107] M. Roshan Fekr, G. McClure, and D. Hartmann. Simulated ice shedding on a full-scale test line. In *Proc. the 8th Int. Workshop on Atmospheric Icing of Structures*, pages 11–16, Reykjavik, Iceland, 1998.

[108] E. J. Routh. *A treatise on the stability of a given state of motion.* Macmillan and Co., London, 1877.

[109] N. A. Saadabad, H. Moradi, and G. Vossoughi. Semi-active control of forced oscillations in power transmission lines via optimum tuneable vibration absorbers: with review on linear dynamic aspects. *Int J Mech Sci*, 87:163–178, 2014.

[110] S. Samukham, T. K. Uchida, and C. P. Vyasarayani. Fast generation of stability charts for time-delay systems using continuation of characteristic roots. arXiv:2005.10719 [math.DS]:1–12, 2020.

[111] W. H. Snyder and J. L. Lumley. Some measurements of particle velocity autocorrelation functions in a turbulent flow. *Journal of Fluid Mechanics*, 48:41–71, 1971.

[112] E. D. Sontag. *Mathematical control theory.* Springer, New York, NY, 1998.

[113] J. W. Speight. Conductor vibration-theory of torsional damper. *Trans Am Inst Electr Eng*, 60:907–911, 1941.

[114] J. R. Stallabrass. *An Appraisal of the Single Rotating Cylinder Method of Liquid Water Content Measurement.* LTR-LT-92, National Research Council of Canada, Division of Mechanical Engineering, 1978.

[115] B. Steinhaus, P. T. Spicer, and A. Q. Shen. Droplet size effects on film drainage between droplet and substrate. *Langmuir*, 22:5308–5313, 2006.

[116] G. Stépán. *Retarded Dynamical Systems: Stability and Characteristic Functions.* Longman, Harlow, UK, 1989.

[117] G. Stépán and L. E. Kollár. Balancing with reflex delay. *Math. Comput. Model.*, 31:199–205, 2000.

[118] S. Theodossiades and S. Natsiavas. Non-linear dynamics of gear-pair systems with periodic stiffness and backlash. *J Sound Vib*, 229:287–310, 2000.

[119] J. R. Valentine and R. A. Decker. A Lagrangian–Eulerian scheme for flow around an airfoil in rain. *Int. J. of Multiphase Flow*, 21:639–648, 1995.

[120] P. Van Dyke. *Galop induit sur une ligne expérimentale a l'aide de profilés en D sur conducteur simple avec ou sans entretoises interphases.* PhD dissertation, Dept. Mech. Eng., Univ. Sherbrooke, Sherbrooke, QC, Canada, 2007.

[121] P. Van Dyke and A. Laneville. Galloping of a single conductor covered with a D-section on a high-voltage overhead test line. *Journal of Wind Engineering and Industrial Aerodynamics*, 96:1141–1151, 2008.

[122] P. Van Dyke and A. Laneville. Simulated ice shedding on a full-scale test line. In *Proceedings of the 8th International Symposium on Cable Dynamics*, Paris, France, 2009.

[123] J. Vecchiarelli, I. G. Currie, and D. G. Havard. Computational analysis of aeolian conductor vibration with a stockbridge-type damper. *Journal of Fluids and Structures*, 14:489–509, 2000.

[124] H. Wagner, V. Ramamurti, R. Sastry, and K. Hartmann. Dynamics of stockbridge dampers. *Journal of Sound and Vibration*, 30(2):207–220, 1973.

[125] L. P. Wang, O. Ayala, and S. E. Kasprzak. Theoretical formulation of collision rate and collision efficiency of hydrodynamically interacting cloud droplets in turbulent atmosphere. *Journal of Atmospheric Sciences*, 62:2433–2450, 2005.

[126] X. Wang, B. Yang, S. Guo, and W. Zhao. Nonlinear convergence active vibration absorber for single and multiple frequency vibration control. *J Sound Vib*, 411:289–303, 2017.

[127] S. Whitaker. Forced convection heat transfer correlations for flow in pipes, past flat plates, single cylinders, and for flow in packed beds and tube bundles. *AIChE Journal*, 18:361–371, 1972.

[128] S. Wiggins. *Introduction to applied nonlinear dynamical systems and chaos.* Springer-Verlag, New York, NY, 1990.

[129] C. Wu, B. Yan, L. Zhang, B. Zhang, and Q. Li. A method to calculate jump height of iced transmission lines after ice-shedding. *Cold Regions Science and Technology*, 125:40–47, 2016.

[130] X. Xie, Y. Wu, K. Liang, S. Liu, and J. Peng. Experiment study on dynamic effects of tower-line systems induced by ice shedding. *Adv. Civil Eng.*, page 6241789, 2020.

[131] J. Xu and Y. Sun. Experimental studies on active control of a dynamic system via a time-delayed absorber. *Acta Mech. Sin.*, 31(2):229–247, 2015.

[132] B. Yan, K. Chen, Y. Guo, M. Liang, and Q. Yuan. Numerical simulation study on jump height of iced transmission lines after ice shedding. *IEEE Trans. Power Deliv.*, 28(1):216–225, 2013.

[133] Y. Zhou, S. Niu, Z. Gao, Y. Zhou, and J. Yang. Research to the influence factors on shedding processes of three-types icing. *Cold Regions Science and Technology*, 155:300–307, 2018.